Program Title: Lightning Effects on Dry Cask Storage Systems

Document Title: Analysis of Lightning Strike Effects on a Holtec Hi-Storm 100 Dry
Cask Storage System for Spent Nuclear Fuel

Document Type: Letter Report, rev.1

Author: J.J. Yugo

NRC Manager: C.E. Antonescu
ORNL Manager: R.T. Wood

**Prepared for
U.S. Nuclear Regulatory Commission
under
DOE Interagency Agreement 1886-N662-4Y
NRC JCN No. Y6624**

Prepared by the
Nuclear Science and Technology Division
OAK RIDGE NATIONAL LABORATORY
P.O. Box 2008
Oak Ridge, Tennessee 37831-6285
managed by UT-Battelle, LLC
for the
U.S. DEPARTMENT OF ENERGY
under contract DE-AC05-00OR22725

TABLE OF CONTENTS

LIST OF FIGURES

ABSTRACT

This report discusses simulation results associated with predicting the effects of a lightning strike on a Holtec Hi-Storm 100 dry cask storage system and compares the effects of grounding the cask to leaving it ungrounded.

The Topical Safety Analysis Report (TSAR) for the Hi-Storm 100 system provides a discussion concluding that lightning would cause no damage to the dry cask storage system (i.e., the overpack or multi-purpose canister) nor to the spent fuel within it. Oak Ridge National Laboratory (ORNL) has performed simulation calculations to confirm this assertion. Based on the results of these calculations, the ORNL investigators conclude that, although lightning currents are predicted to penetrate both the overpack and multi-purpose canister (MPC), no release of radioactive material from the container as a result of a lightning strike is likely to occur. Grounding of the cask appears to have little effect on power deposition in the MPC but does result in a 3-fold decrease in the average power deposited in the concrete shielding within the overpack. The concrete just below the simulated lightning strike location, is heated by current penetration through the steel cask lid but insufficient energy is deposited to heat the concrete, or free water contained in the concrete, to a temperature where a pressure increase or damage would occur.

Other potential hazardous event scenarios resulting from a lightning strike are supported by the simulations that have been performed. The lack of a ground connection from the overpack to a grid in the concrete allows very high electric potentials to develop on the overpack near the concrete pad. These electrical potentials may result in arcing to nearby structures or equipment. Grounding of the cask significantly modifies the voltage distribution on the outer shell of the overpack, reducing it to near zero at the concrete pad. Without a ground connection, voltages on the cask near the concrete pad reach several megavolts and could pose a significant electrical hazard.

EXECUTIVE SUMMARY

A set of computer models were constructed to evaluate the effects of lightning strikes to a Holtec Hi-Storm 100 dry storage cask under both grounded and ungrounded conditions. Power deposition and current density profiles were determined and used to generate temperature profiles in the various regions of the cask assembly. Summarizing the results from numerous models and cases that were evaluated, we found that the temperature rise in all regions of the cask, except for the metal at the strike location itself, is well below the level where damage or rupture would occur. From two-dimensional (2-d) simulations and some of the three-dimensional (3-d) simulations, it was predicted that localized heating of the metal lid at the lightning strike location would be sufficient to melt and vaporize material. However, this occurs only in a very localized region at the lightning strike location and is unlikely to result in a breach of the container.

Basic Model Configurations

Several models with varying degrees of complexity were employed in these analyses to obtain the most useful information as expeditiously as possible. Various 2-d and 3-d models were used at different times. Two-dimensional models included the most detail and highest resolution of the actual cask design while the larger 3-d models required significant simplifications to maintain a reasonable overall model size. The principal regions included in the 2-d model are the multi-purpose canister (MPC) contents, MPC shell, air gap surrounding the MPC, steel lid, lid and base concrete shielding and steel enclosures, overpack shell, concrete radial shielding, concrete pad, soil, ground connection, and external air.

The primary 3-d model yielded information about the azimuthal profiles of power deposition which was then used to determine the proper azimuthal scaling for 2-d results. Other special-purpose 3-d models were used to investigate specific issues with greater accuracy. One of these was a simple concrete-filled steel cylinder with a steel lid and base plate. This model was used to look in detail at the local power deposition at the lightning strike location and the penetration of current through the lid and into the concrete. This model was placed directly on a ground plane and does not have an ungrounded version because the only region of interest was in the immediate neighborhood of the lightning strike.

Specific areas of interest in most of these simulations include power deposition in the outer shell of the overpack, the concrete radial shielding, the steel shell of the MPC and the MPC contents. From the calculated power deposition, estimates of the peak and average temperatures are made. Additional areas of interest are the localized power deposition in the steel lid and the concrete pad, at the cask-pad interface. A calculation of voltages generated on the outer shell of the overpack for grounded and ungrounded casks was performed to assess potential hazards to personnel and equipment in the vicinity.

Description of the Model Environment

Both 2-d and 3-d models of the ungrounded storage casks are located on a 12-in. thick concrete pad containing no steel rebar and with no specific connection to ground other than contact with the soil layer beneath the concrete pad. The grounded-cask models include, in addition, an array of steel rebar rods embedded in the concrete pad and a specific connection from the cask to the rebar and to the model boundary below the soil layer. The boundary condition applied beneath the soil layer forces all fields to go to zero at that surface, and the surface functions as a perfect ground plane. The air above and around the cask was included in the model to a distance of 9 m from the cask and is bounded by a spherical (3-d) or circular (2-d) boundary with a radius of 15 m. The air boundary has imposed on it an open boundary condition that simulates infinite free space. Several feet of soil were included below the concrete, and a boundary condition was imposed on the lower boundary of the soil, forcing all fields to go to zero at that surface. In all of the simulations performed, only a single cask was included in the model. No inter-cask, or multiple-cask calculations were performed.

Scaling of 2-d Results

The 2-d simulation results contain no information about the spatial profile of power deposition in the azimuthal direction and therefore need to be scaled to account for this effect. From 3-d simulations, discussed in detail separately, it was found that 80% of the total power was deposited within an azimuthal angle of 30° for a lightning strike on the outer edge of the lid. Azimuthal profiles of power deposition at various vertical locations on the outside shell of the overpack were made at each time point to determine how the azimuthal profile changes with position and during the pulse. From this set of profiles, a reasonable average profile was determined. A comparison of the azimuthal profiles during the course of the pulse shows that the azimuthal extent does not change significantly during most of the lightning strike pulse so a single azimuthal profile should represent the results reasonably well. Power deposition results from 2-d calculations were scaled by this factor before peak and average temperatures were calculated. The 3-d simulations did not require any scaling before temperatures were calculated from the time-dependant power deposition.

MPC Power Deposition

In all models that were evaluated, the MPC contents were homogenized and average properties used for the analyses, both electrical and thermal. Because the complexity of the actual MPC, contents was not represented in the models, and therefore it is likely that power deposition in the MPC that was calculated by all of the models is overestimated. The many small gaps within the MPC will prevent currents from flowing as calculated in the models. In addition, considerably less actual contact exists between the MPC contents and MPC shell than is represented in the models. Analysis of both grounded and ungrounded casks predict that power deposited within the MPC contents is insufficient to cause temperature increases that could cause internal damage or rupture of the MPC. The models do predict power deposition within the MPC, and no differences between the grounded and ungrounded casks exist, but the power deposited is only sufficient to cause a small average temperature increase in the MPC. Tables ES-1 and ES-2 list the average and peak temperature increases calculated in various regions of the model.

Table ES-1. Average temperature increase in grounded and ungrounded cask components (initial temperatures vary with region)

Cask region	Average temperature increase (°C)	
	Grounded	Ungrounded
MPC contents	2	2
Overpack concrete	0.2	0.3

Table ES-2. Peak temperature increase in grounded and ungrounded cask components (initial temperatures vary with region)

Cask region	Peak temperature increase (°C)	
	Grounded	Ungrounded
MPC contents	18	11
Overpack concrete	5.9	25.3

The material properties and initial temperatures in each model region were evaluated to determine the minimum power deposition density required to cause a detectable temperature change and to determine when damage would begin to occur. Table ES-3 summarizes the total power deposition required over a 500-μs pulse length to reach these two thresholds.

Table ES-3. Required power deposition for a detectable temperature change and for onset of damage in each of the cask regions

	Required power density for 500 μs (W/m^3)	
Cask region	Detectable temperature change	Damage threshold
MPC contents	1.0×10^8	2.7×10^{11}
MPC shell	5.0×10^9	1.6×10^{13}
Overpack concrete	1.0×10^9	1.5×10^{11}
Overpack shell	5.0×10^9	1.6×10^{13}

Power Deposition in Concrete Radiological Shielding

When comparing the power deposition results from grounded and ungrounded cask simulations, we find that substantially more power is deposited in the concrete radiological shielding when the cask is ungrounded compared to when grounded. The ratio of power deposition in grounded and ungrounded casks varies during the excitation pulse from about a factor of 2 to a factor of 13 more power deposited in the concrete in an ungrounded cask. As an overall average, about 3 times as much power is deposited in the concrete shielding in an ungrounded cask than in a grounded cask.

In spite of the differences in power deposition between grounded and ungrounded casks, it was found that both 3-d calculations and appropriately scaled 2-d calculations both predict small peak and average temperature rises in the concrete for both grounded and ungrounded casks. In 2-d calculations, with an initial temperature of 66°C, the average temperature rise was found to be 0.2°C in the grounded cask and 0.3°C in the ungrounded cask. The peak temperature rise was found to be 5.9°C in the grounded cask and 25.3°C in the ungrounded cask. Some earlier cases had shown higher power deposition results but these results were found to be related to the model or excitation profile. The 2-d results for an ungrounded cask still indicate the possibility of a local temperature excursion sufficient for damage. To further quantify the damage potential, a 3-d model was constructed to better represent current penetration through the cask walls. One concern with the 2-d model is that an insufficient number of elements is present to represent the steel can wall thickness. The lid of the 2-d model is represented by ten elements, but the side walls are represented by only two elements. To quantify the degree of current penetration through the lid and walls of the overpack, a specific 3-d model was used. For equivalent conditions to those in the 2-d model, this 3-d model predicted less current penetration through the steel canister walls than predicted by the 2-d model, resulting in a lower temperature rise. Except for a small local region just below the lightning strike location, the 3-d cylinder model showed imperceptible temperature changes. This confirms that the 2-d results are conservative and that the actual power deposition will almost certainly be less than that predicted.

The presence of air vents through the overpack will increase current flow on the inner surface of the overpack and will be expected to increase the power deposited in the overpack shell and concrete shielding. The air vents were not represented in any of the models so a reasonable estimate of the importance of the vents is not available. This feature would be the most useful addition to a more complex model if it were developed.

Power Deposition in the Steel Cask Lid

Obviously, the largest power deposition density occurs at the lightning strike location, which is on the lid in these simulations. There was concern that power deposition would be sufficient to cause localized melting that would breach the cask. Both 2-d and 3-d models confirmed that the highest power density is deposited at the strike location. Because of the wide variation of spatial resolution of the various models, the different simulations predicted varying peak temperatures on the lid. Average temperatures were in close agreement because the heat deposition is averaged over such a large volume that little average temperature rise occurs in any model. The 3-d cylinder model is fundamentally a different configuration from the storage cask and thus is not expected to agree with the results from the two other cask models. Its higher spatial resolution, however, may make the results from this model the most accurate. With the larger cell sizes in the 3-d cask model, the peak temperature is actually averaged over a large volume, thus reducing the predicted peak temperature. Without accounting for latent heat, the 3-d cylinder model predicts approximately 129 cm^3 of melted material (5 cm cube). Including the latent heat required to first melt and then vaporize the metal, the volume of vaporized metal drops to 53 cm^3 (3.8 cm cube). Because of the small overall size of this model, and the specific boundary conditions applied to it, this model is expected to predict higher temperatures than will be encountered in an actual lightning strike. Nonetheless, the temperatures predicted by this model are significant enough to raise concern and warrant more careful analysis of the local heating process (see Table ES-4).

Table ES-4. Average and peak predicted temperature increases in the cask lid from various models

Cask region	Peak temperature increase (°C)	
	Average	Peak
2-d cask model	12	1767
3-d cask model	~0	62
3-d cylinder	3	>10,000

Voltage on the Outer Shell of the Overpack

One major difference between grounded and ungrounded casks is the voltage profile on the outer shell of the overpack. With the cask grounded to a rebar grid embedded in the concrete pad, the cask voltage at the interface with the pad will be close to zero. In simulations, the voltage is precisely zero at the boundary condition that is applied below the simulated soil layer under the concrete pad. With a ground connection through the soil and concrete to the cask, only a very small voltage occurs on the cask at the concrete interface. However, with the cask ungrounded, the voltage at the concrete interface is several MV, causing concern for personnel and equipment. In Figure ES-1, normalized voltage profiles along the vertical outside surface of the overpack are shown for grounded and ungrounded casks. In this figure, the voltages are normalized to the peak voltage for each profile. In the various simulations peak voltages ranged from about 3 to 6 MV, depending on the excitation profile. One difference between the simulation results (shown in Figure ES-1) and an actual lightning strike will be the rate at which the voltage goes to zero near the concrete pad. Since the simulation forced the voltage to go to zero only a short distance below the concrete pad, the simulations show a steeper voltage gradient than would be the case in a real lightning strike. In a real lightning strike, voltages will be higher in the concrete pad and soil for both grounded and ungrounded casks because the currents cannot be spread and dissipated as quickly and efficiently as in an idealized case.

Normalized Voltage Along Outside Surface of Overpack
From Top to Bottom
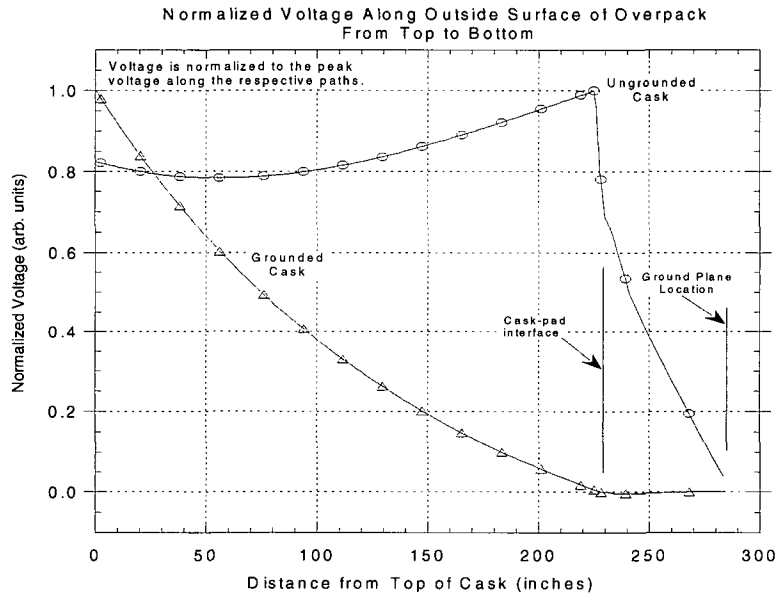
Figure ES-1. Normalized voltage along outside
surface of overpack.

Discussion of Assumptions and Simplifications

Strike Location

Only a single lightning strike location was evaluated for each model, leaving the possibility that other strike locations may result in higher temperatures, particularly locally.

Lightning Current Pulse Shape

Pulse shape is seen to have a significant effect on power deposition, due to the varying frequency content. Only a couple of lightning pulse shapes have been simulated, and the quantitative effects of other pulse shapes are unknown. Beyond that, real lightning pulses can and do have widely varying and complex pulse shapes, the effects of which have not been modeled. Longer duration lightning pulses will penetrate the steel shell more deeply and thus increase the predicted power deposition in the cask interior.

Model Approximations

The largest contributors to uncertainty from the model designs are expected to be from the fact that the air vents allow a clear and direct path through the overpack to the MPC outer shell but are not well represented in any of the models that have been evaluated. In all of the models, improved accuracy would also be obtained if metal wall thicknesses were represented by additional elements.

Material Properties

Representative material properties were chosen for each region of the model but no attempt was made to quantify the effects of the range of property values on the results. In particular, concrete properties vary widely and are dependant on mixing and curing processes as well as the constituent materials. The properties of the actual concrete used in the Holtec casks are unknown.

1. INTRODUCTION

This report compares the effects that grounding a Holtec Hi-Storm 100 dry cask storage system will have on its performance as compared to the performance of the same cask left ungrounded. The issue to be resolved is whether or not the dry cask requires grounding to make it safe for use as a storage system for spent reactor fuel. Oak Ridge National Laboratory (ORNL) researchers have simulated these tests using the electromagnetic analysis system (EMA) code and various two-dimensional (2-d) and three-dimensional (3-d) models. Appendix A contains a theoretical description of the mathematical basis for the EMAS code and also contains numerous references regarding specific aspects of the mathematical techniques used in the code. The energy deposition calculated with the EMAS electromagnetic modeling code is used an input to the heat transfer code Heating[16] which is used to calculate time dependant temperature profiles throughout the cask model.

The Topical Safety Analysis Report (TSAR) for the Hi-Storm 100 system concludes that lightning would cause no damage to the dry cask storage system (i.e., the overpack or multi-purpose canister) nor to the spent fuel within it. Calculations were designed to determine the power deposition in each of the principal regions of the storage cask when the cask is grounded and ungrounded. The most important features of the cask are included in the models, but one of the primary goals of the modeling is to determine whether the models, as constructed, accurately reflect the behavior of the storage cask. Approximations and simplifications constantly require trade-offs to be made between accuracy and model complexity, which translate directly into computer time and resource requirements. In order to perform the calculations that are required to both answer the questions and verify the applicability of the models within the available schedule, the research team made significant simplifications in the models' representation of the storage cask. To add additional detail in critical regions, or to verify the applicability of the model, we made additional 2-d or 3-d models of specific aspects of the cask in order to increase resolution. Results from these ancillary models can either confirm or refine the results from the other storage cask models.

While the steel shell of the Holtec Hi-Storm 100 overpack is a reasonable electrical conductor, the cask is installed on a concrete pad, which in turn sits on soil. Because both the concrete pad and the soil are very poor conductors of electricity, it is expected that quite different electrical behaviors will occur, depending on whether or not the cask is grounded to a buried conducting grid. A rebar grid acts to take the highly localized lightning current and spread it over a large area, so that the current can be distributed at as low an electrical potential as possible. Physically large structures subjected to short electrical pulses behave as transmission lines with distributed properties. In such structures the term "ground" really doesn't have a clear meaning. As expected, we found that the current pulse propagates through the cask model and is reflected from impedance mismatches and is dampened as power is deposited. In particular, the impedance discontinuity at the interface between the cask and concrete pad is significantly modified by the presence or absence of a ground connection.

A detailed 2-d model of the cross section of a storage cask was used to obtain much of the data regarding power deposition. A 3-d model was employed primarily to obtain azimuthal profile information to be used in scaling of 2-d results, but was also used as a check on the specific results for various regions of the two models. In particular, power deposition results for the multi-purpose canister (MPC) contents from the detailed 2-d model and the highly simplified 3-d model were compared to validate the results.

1

2. LIGHTNING CURRENT PULSE MODELS

Lightning strike current profiles have several components as well as a wide variation of peak currents and time durations. An exhaustive literature search to determine parameters and their ranges was not carried out. A number of papers[1-6] related to qualification testing of military and civilian systems for lightning response cite the standards developed by the Society of Automotive Engineering (SAE), which developed a testing standard[1] during the mid to late 1970s. The SAE standard was eventually adopted as a military standard[2] for lightning qualification testing. The waveform in Figure 2-1 is similar to that published by the SAE committee on lightning test techniques. Ranges of time durations and currents are given in the figure, and the waveforms used in these simulations were constructed to be in rough agreement with the general waveform shown.

In the cases described in this report, only two lightning strike current components were used, the short-duration, high-current initial strike and the long-duration, low-current continuing current. Determining whether one or both of these portions of the pulse were important to the total power deposition was one objective in the initial transient pulse analyses that were performed. Because the initial strike and the continuing current operate on such vastly different time scales (500 μs compared to 1 s) it is difficult to analyze both within a single model because of the large number of time steps required. Therefore, a number of otherwise identical cases were analyzed with excitations of 500 kA for 250 μs or alternatively 5 kA for 1 s. The peak currents chosen for the simulations were larger than the maximum quoted in the literature as a safety margin, enabling the simulations to compensate for some of the uncertainty from model and parameter simplifications.

The two primary lightning pulse shapes used as excitations in these analyses are described as

- triangular pulse, 300–500 kA, 250 μs duration and

- constant current pulse, 3–5 kA, 1 s duration, but with slight up and down ramps to reduce the high frequency harmonics.

No attempt to systematically explore the impact of current profile changes on the calculated power deposition was attempted because of the highly compressed schedule and the need to be able to compare results from all models. In a few cases a combined excitation pulse was used, similar to that shown in Figure 2-2, although for most cases of this type, only a short period of continuing current was included to avoid having an excessive number of time points in the analysis. The current pulse shown in Figure 2-2 is the calculated current flowing in the cell where the excitation was applied and was plotted from the analysis output.

One of the concerns in the simulations was the excitation of higher order harmonics from the sudden application of a current pulse. Step function pulses excite higher harmonics, and the solutions do not converge as readily. Two-dimensional cases were generally run with a triangular pulse of 250 μs duration and 300–500 kA amplitude plus a trapezoidal-shaped pulse of approximately 1 s duration, with an amplitude of 3–5 kA. In the trapezoidal pulse, a short ramp-up and ramp-down is included to reduce the harmonics. Both ramps in the continuing current pulse had slopes less than half that in the initial strike current to ensure that effects from the sudden onset were no greater than in the initial strike pulse.

In the final calculations, source amplitudes of 500 kA for 250 μs and 5 kA for 1 s, were used with triangular and trapezoidal pulse shapes, respectively. These values give some margin above the highest expected lightning strike currents. Some calculations were performed using sinusoidal-shaped excitation pulses for both components of the current to see whether improvements in convergence resulted and to see if any features of the resultant power deposition profiles were artifacts of the excitation profile details.

3

In these cases, the initial lightning strike pulse was modeled as a sinusoidal wave with a period of 500 μs and the continuing current as a sinusoid with a period of 1 or 2 s. Figure 2-3 shows an example of the initial lightning strike pulse shape used. For consistency, the peak currents with sinusoidal excitations were scaled to give the same total energy as the triangular pulse shapes used.

Idealized Lightning Strike Current Profile
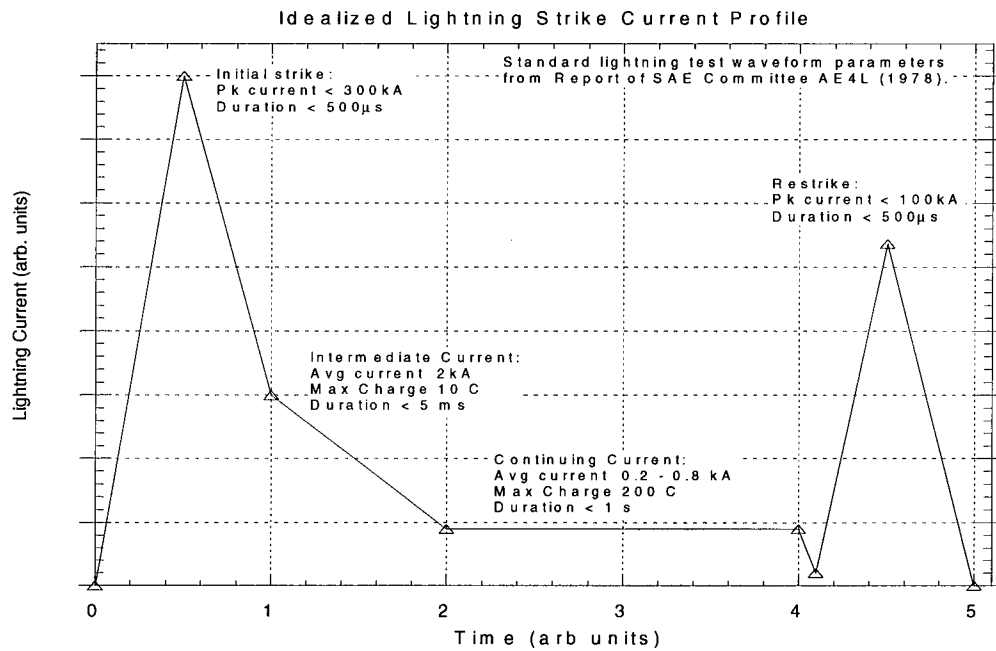
Figure 2-1. Idealized lightning waveform, indicating reasonable ranges of currents and time durations for each portion of the lightning strike (adapted from ref 2).
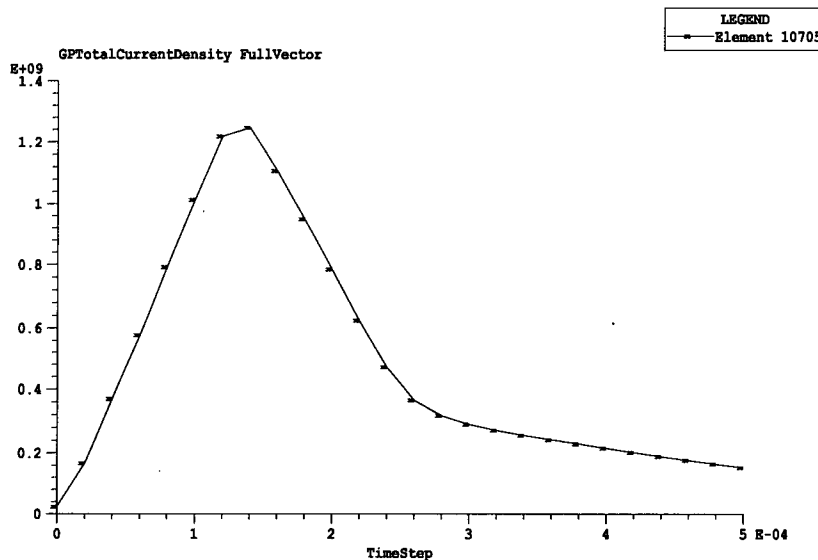
Figure 2-2. Example of the current profile at the excitation location in a simulation with both an initial strike current and a continuing current.

4
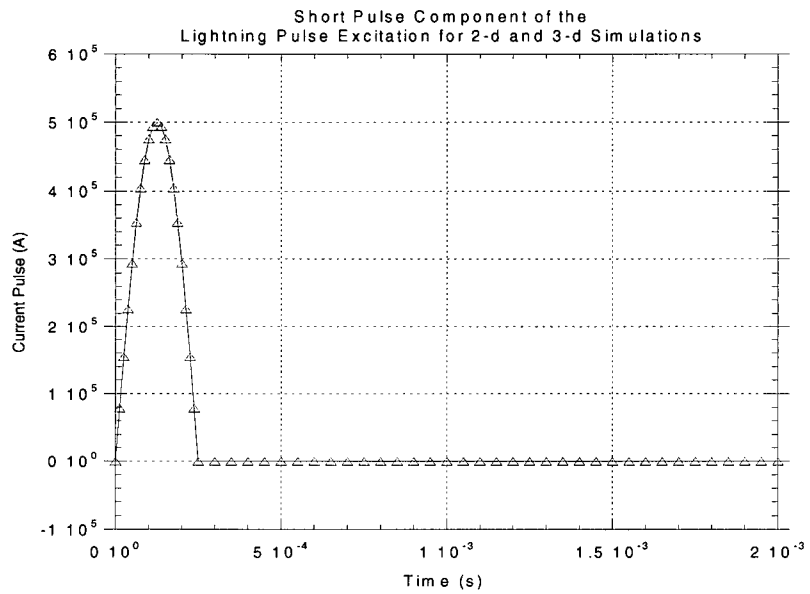
Figure 2-3. Initial, short, high-current, sinusoidal lightning pulse profile used in some of the 2-d and 3-d simulations.

5

3. SKIN DEPTH

The frequencies present in the lightning pulse model used in these calculations can penetrate deeply into metal structures so that, even though the steel shells have thickness on the order of 1 in., the currents will penetrate into the interior of the cask system. Electrical skin depth is defined as the thickness of material through which the current will be reduced to 1/e of its peak value on the surface. At higher frequencies, the current penetrates less deeply. The short (250 µs), high current (300–500 kA) part of the lightning pulse is equivalent to a frequency of 2 kHz and will fall to 1/e of its surface value at a depth of 0.014 inch in carbon steel. With the large currents in a lightning pulse, current will still penetrate the overpack shell. The slower part of the lightning pulse (1 s) has a characteristic frequency of approximately 0.5 Hz. This part of the lightning pulse has the capability to penetrate very deeply into the metal structure, although it contains much less current than the short initial spike. The skin depth in carbon steel for the long, low-current part of the pulse is of the order of 1 in., meaning that it will easily penetrate through the steel shell of the overpack and MPC and into the interior of the canister.

Skin depth (δ) is defined as

$$\delta = [\pi f \mu \sigma]^{-\frac{1}{2}}$$

where:

δ is the skin depth in m and is the depth in a conducting medium where the current has decreased to 1/e of its surface value,

f is the wave frequency in Hz,

μ is the permeability in Henries/m and is equal to $\mu_r \mu_o$,

$\mu_o = 4\pi \times 10^7$ Henries/m,

μ_r is known as the relative permeability,

σ is the conductivity in mhos/m.

Skin depth is inversely proportional to frequency, conductivity, and permeability, meaning that for more highly conductive materials or higher frequencies, the current will penetrate less into the material. A plot of skin depth as a function of pulse width is shown in Figure 3-1. This calculation was performed with the assumption of a continuous sinusoidal current with a half-cycle equal to the pulse width noted on the plot. It is not entirely accurate, but illustrates how the skin affects the current's penetration into the metal.

For a sinusoidal pulse with a half-cycle time
equal to the pulse width, the current will
decay to 1/e (0.367) of its peak (surface)
value at the depth indicated.

A sinusoidal pulse of 250μs duration
will have a skin depth of 0.014 inches.

A pulse of 1 s duration will have a skin
depth of 0.886 inches.

Carbon Steel:
$\mu_r \sim 2000$

$\sigma \sim 5 \times 10^5$ mhos/m
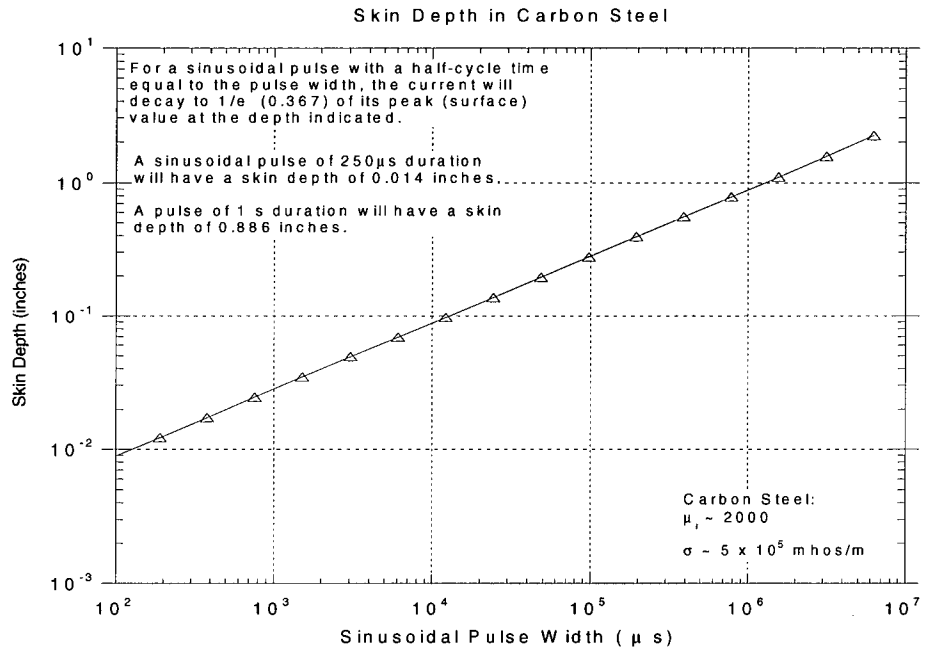
Figure 3-1. Skin depth in carbon steel as a function of the pulse width (frequency).

4. CASK DESIGN

The Hi-Storm cask (multi-purpose canister plus overpack) provides a reasonably good conducting path for the lightning-induced current. Traditional lightning protection systems (lightning rods) would route the lightning current to ground through an alternate path, thereby reducing the current flowing through the protected object. By flowing through the overpack itself, lightning-induced current does have the ability to penetrate into both the overpack and the MPC. The cask system also has the electrical characteristics of a large capacitor and will charge to a high potential with a pulsed input current and then more slowly discharge through the low conductance path of the concrete and soil.

The air vents at the top and bottom of the cask system provide a direct path for currents to flow through the overpack to the shell of the MPC. Although this path is somewhat less desirable (more resistive) than directly down the side of the outer shell, it will still share a significant fraction of the current at that azimuthal location. Even without a direct physical connection between the steel shells of the overpack and MPC, the mutual inductance will couple energy into the MPC from currents flowing in the overpack shell. The cask is constructed much like a coaxial transmission line, guaranteeing a strong electromagnetic coupling between the inner (MPC) and outer (overpack shell) conductors. It would be expected that currents would be induced into the MPC shell by currents flowing in the overpack shell due to the flux linkages between the two, even without direct contact.

Similarly, the overpack shell, with a concrete-filled space between conducting plates, should exhibit behavior similar to a lossy, dielectric-filled transmission line. In a transmission line with an impedance mismatch at one end (cask-concrete pad interface), a pulse of energy, injected at one end, would be expected to reflect back repeatedly from the impedance mismatch until its energy is finally dissipated. In this case, the dissipative media is the storage cask and contents.

A cutaway view of a 3-d model of the Holtec storage cask is shown in Figure 4-1 with the MPC removed. Internal and external void spaces for this model are also not shown in the figure. The raised ring on the top lid is a steel-cased concrete radiological shield, as is the central cylindrical region on the inside surface of the lid.
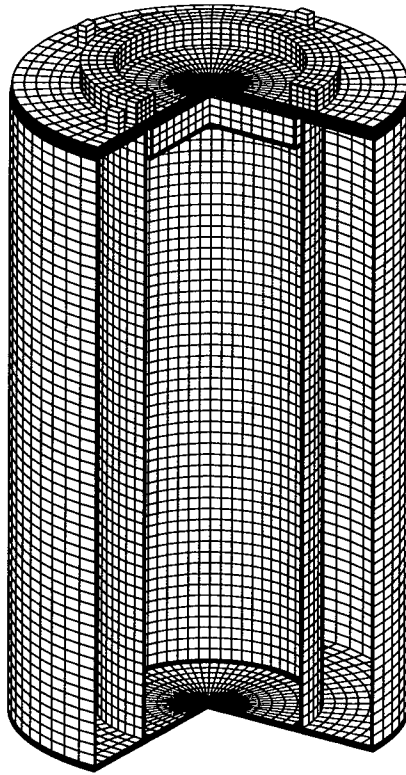
Holtec Hi-Storm 100
Dry Cask Fuel Storage Overpack

Shown with:
Concrete radial shielding removed
Multi-purpose canister removed
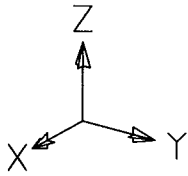
Figure 4-1. Cutaway view of the 3-d model from which the 2-d model was derived. In this view the concrete radiological shielding, MPC, and bottom shield have been removed for clarity. Also removed are the internal and external air space elements.

5. CASK MODELS

Both 2-d and 3-d models were constructed to simulate transient lightning currents flowing through the Holtec dry storage cask. Grounded and ungrounded versions of both 2-d and 3-d models were evaluated. The 2-d models incorporated the most details of the storage cask design and were the primary mechanism for determining the relative power deposition in the various cask regions. Necessarily, the 3-d models included substantially less detail. One primary use of the 3-d cask model was simply to determine the azimuthal extent and profile of lightning currents flowing in the components of the cask so that 2-d simulation results could be scaled appropriately. Another 3-d model was constructed specifically to evaluate current penetration through the steel lid and into the concrete shielding. In this model much better resolution of the steel lid and wall thicknesses were incorporated. While global power deposition and current flow were evaluated, the primary purpose of this model was to evaluate local effects at the location of the lightning strike.

5.1 Two-Dimensional (2-d) Model

The 2-d model consisted of approximately 30,000 elements and did not use mid-side grid points. Material properties for an approximate mixture of materials in spent nuclear fuel rod assemblies were averaged and homogenized throughout the MPC volume. This gives only average results and precludes obtaining an accurate estimate of peak temperatures in the MPC. The average MPC material properties were principally determined by the assumed void fraction and UO_2 properties. The same average MPC properties were also used in 3-d simulations, discussed later. The principal other materials in the storage cask are carbon steel and concrete. The typical material properties used in the 2-d simulations are listed in Table 5-1. Because time and resources were extremely limited, ranges of material property values were not evaluated to determine the sensitivity to particular properties. The 2-d model used for most of the simulation calculations is shown in Figure 5-1. In this figure, the elements representing the exterior and interior air, concrete pad, and soil are not shown. The gap between the MPC and overpack is visible in this figure but other features, such as the interfaces between the MPC shell and contents and between the MPC and bottom shielding, are difficult to discern because the elements are of similar size and shape. In the Holtec cask system design, vertical ribs contact the sides of the MPC for positioning. Since it is unlikely that these connections would provide reliable electrical contacts, they were not included in the model. Thus, the MPC in the simulation model is connected to the overpack only through contact with the base and through the mutual inductance with the overpack. A small air gap is provided on the sides and top of the MPC. The lightning strike current was injected into the model on the right side of the lid, either into the lid itself, into the lid gap shield ring, or into the retaining bolt. In the 2-d model, the thickness of the steel in the lid region is represented by 10 elements and therefore should represent the behavior of the lid very well. With fewer elements representing the overpack wall thickness, the possibility exists that current penetration through the side walls will be overestimated. In this model the steel shell of the MPC is represented by only a single element, also leading to a risk of overestimating current penetration into the MPC interior.
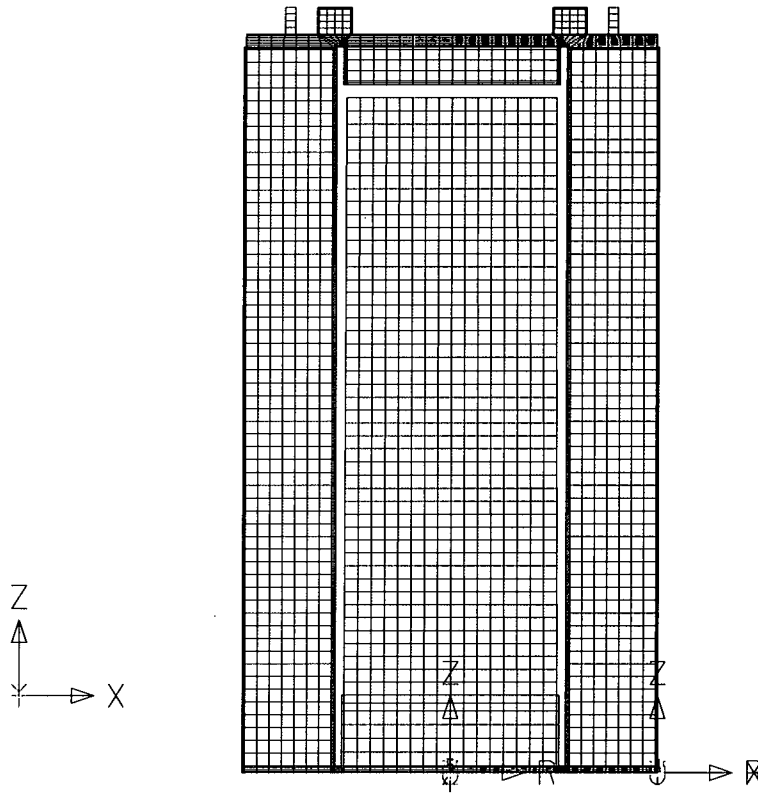
Figure 5-1. Two-dimensional model of Holtec Hi-Storm 100 storage cask. The elements representing the surrounding air, internal voids, the concrete pad, and soil are not shown. The interfaces between the MPC and bottom shielding and between the MPC contents and MPC shell are difficult to discern in this figure because the elements are all of a similar size.

Table 5-1. Electrical and thermal properties of the components in the 2-d computational model

Component	Properties
MPC contents[7,9,10]	Homogenized composition of appropriate fuel rod assembly UO2: 29.97%, Zircaloy: 10.04%, Inconel 718: 0.281%, SS304: 0.062%, Void: 58.86%. Avg MPC: $\mu_r = 1.01, \varepsilon_r = 1.01, \sigma = 5.2 \times 10^3, c_p = 7.013 \times 10^{-5}, k_{avg} = 4.4, \rho_{avg} = 3147$
MPC shell[8,9]	Steel: $\mu_r = 2,000, \varepsilon_r = 10, \sigma = 5 \times 10^6, c_p = 434, k = 60.5, \rho = 7854$
Overpack shell[8,9]	Steel: $\mu_r = 2,000, \varepsilon_r = 10, \sigma = 5 \times 10^6, c_p = 434, k = 60.5, \rho = 7854$
Radial shielding[11-13]	Concrete: $\mu_r = 1.0, \varepsilon_r \sim 10, \sigma = 0.033, c_p \sim 7530, k \sim 1.7, \rho \sim 2850$
Internal voids	Air: $\mu_r = 1, \varepsilon_r = 1, \sigma = 0$
Lid[8,9]	Steel: $\mu_r = 2,000, \varepsilon_r = 10, \sigma = 5 \times 10^6, c_p = 434, k = 60.5, \rho = 7854$
Ext. lid shield shell[8,9]	Steel: $\mu_r = 2,000, \varepsilon_r = 10, \sigma = 5 \times 10^6, c_p = 434, k = 60.5, \rho = 7854$
Ext. lid shielding[11-13]	Concrete: $\mu_r = 1.0, \varepsilon_r \sim 10, \sigma = 0.033, c_p \sim 7530, k \sim 1.7, \rho \sim 2850$
Int. lid shield shell[8,9]	Steel: $\mu_r = 2,000, \varepsilon_r = 10, \sigma = 5 \times 10^6, c_p = 434, k = 60.5, \rho = 7854$
Int. lid shielding[11-13]	Concrete: $\mu_r = 1.0, \varepsilon_r \sim 10, \sigma = 0.033, c_p \sim 7530, k \sim 1.7, \rho \sim 2850$
Base shield shell[8,9]	Steel: $\mu_r = 2,000, \varepsilon_r = 10, \sigma = 5 \times 10^6, c_p = 434, k = 60.5, \rho = 7854$
Base shielding[11-13]	Concrete: $\mu_r = 1.0, \varepsilon_r \sim 10, \sigma = 0.033, c_p \sim 7530, k \sim 1.7, \rho \sim 2850$
External space	Air: $\mu_r = 1, \varepsilon_r = 1, \sigma = 0$
Rebar grid in pad[8,9]	Steel: $\mu_r = 2,000, \varepsilon_r = 10, \sigma = 5 \times 10^6, c_p = 434, k = 60.5, \rho = 7854$
Concrete pad[8]	Concrete: $\mu_r = 1.0, \varepsilon_r \sim 10, \sigma = 0.033, c_p \sim 7530, k \sim 1.7, \rho \sim 2850$
Soil[8]	Average: $\mu_r = 1.0, \varepsilon_r \sim 12, \sigma \sim 0.05$

For all materials:

Permeability (μ_r)	relative permeability (dimensionless)
Permittivity (ε_r)	relative permittivity (dimensionless)
Conductivity (σ)	mhos/m (i.e. copper $\sim 5.8 \times 10^7$ mhos/m)
Specific heat (c_p)	J/kg°K
Thermal conductivity (k)	W/m°K
Density (ρ)	kg/m^3
Anisotropy / nonlinearity	Anisotropic and non-linear material properties were not used.

5.2 Three-Dimensional (3-d) Model

This model was constructed primarily to obtain information about the azimuthal variation of current flow and power deposition because that information could not be obtained from the 2-d models. The model is a multilayered cylinder with overall dimensions consistent with the Holtec Hi-Storm 100 cask. It includes a homogenized representation of the MPC at the center, surrounded by a steel layer, a concrete layer, and an outer steel layer. From this model, we are primarily interested in obtaining information about the power flow from the outside surface inward and are not particularly interested in the power deposition in the MPC contents. The approximations in the design relative to the actual cask design will cause the results in the deep interior of the model to be of poor quality. Nonetheless, some plots of predicted power deposition in the interior were made to verify that they were within a reasonable range. It is expected that heating predictions in the interior of this model will be higher than actual because of the model simplifications and the elimination of one of the steel layers that exists in the actual cask design.

The steel walls on the outside and inside surfaces of the concrete layer are consistent with those in the actual cask design in overall dimensions and thickness. The lid and shielding material on and under the lid have been greatly simplified

The 3-d model was constructed with approximately the same number of elements as the 2-d model to preserve a reasonable computation time and manageable file sizes. The 3-d cask model retained only the most essential features of the 2-d model but required significant simplifications to maintain a model size compatible with the computer memory and schedule constraints. The 3-d model included the inner and outer shells of the overpack and the MPC. The vertical shielding was incorporated into the space between the inner and outer overpack shells. A single layer of carbon steel represented both the inner overpack shell and the MPC shell. In the 3-d model the steel shell wall thicknesses were modeled using either two or three elements to represent the wall thickness. It is essential to have multiple elements through the steel wall thickness to adequately represent skin effects. Because fewer elements were used to represent the steel wall thicknesses in the 3-d model, it would be expected that fields would be predicted to penetrate further into the interior in 3-d simulations.

The mesh sizes in the 3-d model were increased from the order of a few inches on a side to about 1 foot on a side, except in the metal wall thickness. To give reasonably accurate predictions of the azimuthal extent of current flow, the model was made nonuniform in the azimuthal direction. On the side nearest the lightning strike location, 16 azimuthal segments were included, each 5.625° wide. On the remaining 270° of circumference, 12 segments of 22.5° each were used. This gives a somewhat increased resolution in the region of highest interest, but poor resolution over the balance. A cross section of the 3-d cask model is shown in Figure 5-2. In this figure the concrete pad, soil, and air surrounding the cask are not shown. Material properties were not changed from the 2-d simulations, although fewer distinct components were included in the 3-d model. Table 5-2 lists the electrical properties of the principal components of the 3-d cask model. The 3-d model, used to determine the azimuthal profile of power deposition, was also used directly to calculate temperatures in the overpack shell, radial shielding concrete, MPC shell, and MPC contents. However, simplifications made in the 3-d model will reduce the accuracy of the results in some regions. The external overpack shell and shielding concrete should be represented fairly well by this 3-d model, but the MPC and overpack shells were modified to reduce the complexity of the model. Although the results for the MPC contents and shell were evaluated and were compared to the equivalent results from 2-d simulations, larger differences were expected. In the 3-d model, the outer shell of the MPC and inner shell of the overpack were combined and internal voids were eliminated. In the 3-d model current paths through the overpack and into the MPC were enhanced by the elimination of void spaces so that increased heating of the MPC would be expected from this model. The two sources used in the 3-d model are a transient pulse of 500 kA for 250 μs with a triangular waveform, and a trapezoidal pulse of 1 s

14

duration with an amplitude of 5 kA. As with the 2-d simulations, some cases utilized excitations with a sinusoidal profile. The excitation location was typically at or near the center of the steel top lid.
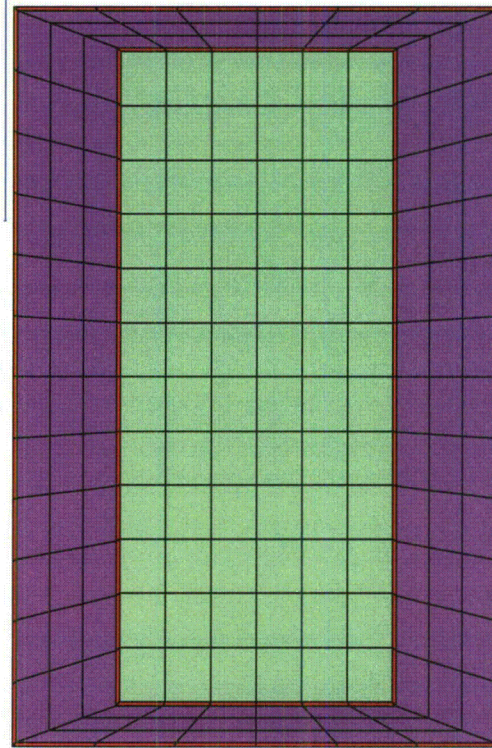
Figure 5-2 Vertical cross section of 3-d model of storage cask. The center region is the MPC, surrounded by a steel shell, a concrete region and an outer steel shell.
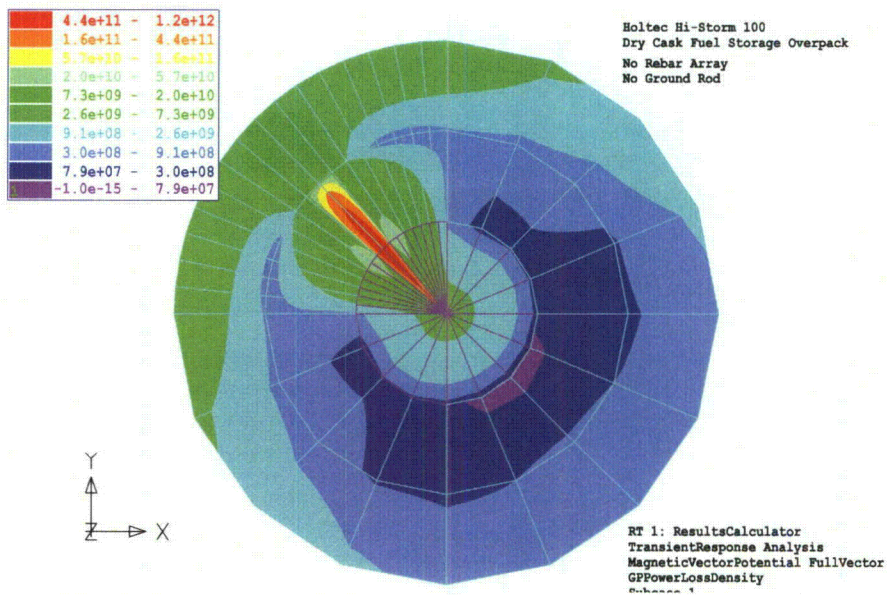
Figure 5-3 Top view of 3-d storage cask model showing non-uniform azimuthal element spacing.

Table 5-2. Electrical properties of components included in the 3-d cask model

Component	Properties
MPC Contents [7,9,10]	Homogenized composition of appropriate fuel rod assembly UO2: 29.97%, Zircaloy: 10.04%, Inconel 718: 0.281%, SS304: 0.062%, Void: 58.86%. Avg MPC: $\mu_r = 1.01, \varepsilon_r = 1.01, \sigma = 5.2 \times 10^3, c_p = 7.013 \times 10^{-5}, k_{avg} = 4.4, \rho_{avg} = 3147$
MPC shell [8,9]	Steel: $\mu_r = 2{,}000, \varepsilon_r = 10, \sigma = 5 \times 10^6, c_p = 434, k = 60.5, \rho = 7854$
Overpack shell and lid [8,9]	Steel: $\mu_r = 2{,}000, \varepsilon_r = 10, \sigma = 5 \times 10^6, c_p = 434, k = 60.5, \rho = 7854$
Radial shielding [11,13]	Concrete: $\mu_r = 1.0, \varepsilon_r \sim 10, \sigma = 0.033, c_p \sim 7530, k \sim 1.7, \rho \sim 2850$
External space	Air: $\mu_r = 1, \varepsilon_r = 1, \sigma = 0$
Rebar grid in pad [8,9]	Steel: $\mu_r = 2{,}000, \varepsilon_r = 10, \sigma = 5 \times 10^6, c_p = 434, k = 60.5, \rho = 7854$
Ground connection [8,9]	Steel: $\mu_r = 2{,}000, \varepsilon_r = 10, \sigma = 5 \times 10^6, c_p = 434, k = 60.5, \rho = 7854$
Concrete pad [8]	Concrete: $\mu_r = 1.0, \varepsilon_r \sim 10, \sigma = 0.033, c_p \sim 7530, k \sim 1.7, \rho \sim 2850$
Soil [8]	Average: $\mu_r = 1.0, \varepsilon_r \sim 12, \sigma \sim 0.05$
Open boundary	Air: $\mu_r = 1, \varepsilon_r = 1, \sigma = 0$

For all materials:	
Permeability (μ_r)	relative permeability (dimensionless)
Permittivity (ε_r)	relative permittivity (dimensionless)
Conductivity (σ)	mhos/m (i.e. copper ~5.8 x 10^7 mhos/m)
Specific heat (c_p)	J/kg°K
Thermal conductivity (k)	W/m°K
Density (ρ)	kg/m^3
Anisotropy / nonlinearity	Anisotropic and non-linear material properties were not used.

5.3 Three-Dimensional Cylinder Model

5.3.1 Purpose

A simple steel cylinder was modeled to more closely investigate current penetration through the steel shell and lid of the overpack. In the physically larger models, it was not possible to represent material wall thicknesses with many elements because the computation time would become prohibitive and memory and storage resources would be exceeded. Because of these limitations, the primary models that were used to accurately represent the physical dimensions of the storage cask could not also accurately predict current penetration through it. In particular, in the regions of very high current density at the lightning strike location, there was concern that the detailed models would over predict current penetration trough the outer shell. This would result in an over prediction of the heating of the contents and over prediction of the associated pressure increase. It is reasonable to expect that peak temperatures will be strictly a function of the local material and lightning properties and will have little or no

relationship to the overall system design or to whether or not a ground connection is present. A detailed model of the local region of a lightning strike should give accurate predictions of peak heat deposition, currents, and temperature changes. A complete model of the storage cask, however, is necessary to evaluate average changes since they will be influenced by the structural details to a greater extent.

5.3.2 Model

The model employed was a cylinder of carbon steel with a wall thickness of 1 in. The cylinder had lids on both top and bottom which were also 1 in. thick and was filled with concrete that had the same material properties as that in the radiological shielding. Figure 5-4 shows the cylindrical model with the concrete interior and external air removed. The portion of the model shown is the carbon steel cylinder walls, top lid and bottom lid. The cylinder was placed directly onto the perfectly conducting ground plane that formed one of the boundary conditions. There was no "ungrounded" case evaluated using this model. The steel cylinder has inside dimensions of 10-cm radius and 30-cm height. Lid and wall thickness were both 2.54 cm (1 in.). The model represented the cylinder wall thickness by 10 elements. An initial model represented the lid and base using three elements and was modified later to also represent the lid using 10 elements. Element thicknesses were then about 0.25 cm (0.1 in.) in the radial direction in the cylinder walls. This number of elements is more than necessary to accurately model the exponential current decay through the metal walls of the cylinder. In this model symmetry is invoked to allow only one quadrant of the cylinder to be actually modeled. With a lightning strike location at the center, the response will also by symmetric.

5.3.3 Excitation

The excitation used to drive this model was the same as used in the larger 2-d and 3-d cask models. The peak excitation current was 500 kA with a triangular pulse shape and duration of 250 μs. The longer time scale, lower current portion of the lightning strike was not simulated since it had been seen earlier not to contribute significantly to the internal heating. Although the lower frequency components penetrate easier into the metal, the lower initial current causes this component of the lightning strike to be inconsequential to the heating scenarios that have been evaluated.
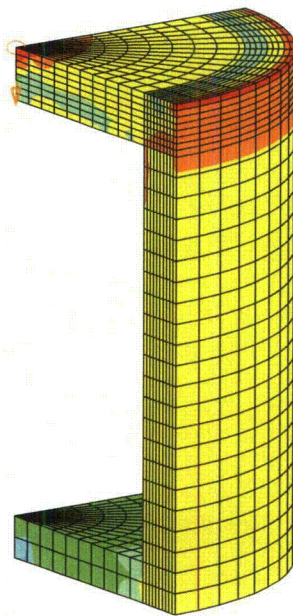
Figure 5-4. Cylindrical model walls and lids. The cement interior is not shown.

17

6. RESULTS FROM TRANSIENT ELECTROMAGNETIC SIMULATIONS

For most of the models which were evaluated, data is presented for power loss density and total current density in various regions of the models. For most of these cases, only plots at or near the time of peak power deposition are shown. For certain cases, voltages along a path through the model are also shown. Most plots shown are for a subset of the model (e.g., only concrete regions, or only steel regions) so that the overall peak value in that region, or type of material, can be easily determined from the index for the plot.

6.1 Transient Results from the Two-Dimensional Model

The lightning strike for this model is a current source at top of low impedance lightning strike channel that originates in the air above cask and injects current into top lid shield enclosure. As with most simulations reported here, the current profile is a triangular pulse with a peak of 500 kA and a duration of 250 μs.

The power loss density in the complete storage cask, concrete pad and subsoil layer is shown in Figure 6-1 at a time close to the peak of the lightning pulse. The grounding connection is seen penetrating through the concrete pad and soil layer. To make the distinctions between model regions clearer, the internal void space between the MPC shell and overpack is not shown. With all model regions shown, it is not possible to determine exactly where the peak power deposition occurs. This figure is shown only to give an overall view of the cask and to show the effect of the ground connection. The power loss density in the non-metallic regions of grounded and ungrounded casks are shown in Figures 6-2 and 6-3. These regions include the concrete radiological shielding throughout the overpack and the contents of the MPC. These regions experience similar power deposition because they are all enclosed within carbon steel structures. The peak power density is similar in the two cases but has very different profiles. The predicted peak power deposition in the grounded cask is about 4×10^9 W/m^3 and in the ungrounded cask 3.3×10^9. The ground connection will modify the current paths through the cask, and local edges and corners will enhance the power loss of one case over the other. The difference in peak power deposition between these two cases is not significant. For both cases, the peak power deposition occurs in the steel lid. Contours of current density for the same regions of the grounded and ungrounded casks are shown in Figures 6-4 and 6-5. As with the peak power deposition, the peak current density for the two cases is nearly identical. Again, the peaks occur on the lid near the location of the lightning strike. The predicted peak current density in the grounded cask is 7.8 MA/m^3 with 7.1 MA/m^3 predicted in the ungrounded cask. While the overall peak values of current density and power density are nearly identical in grounded and ungrounded casks, the peaks in individual regions are not. Close-up views of the current density profiles in carbon steel regions near the top of the grounded and ungrounded casks are shown in Figures 6-6 and 6-7. There is a difference in the peak current density between the grounded and ungrounded cases of 60%, although this is probably due mostly to details of the differences in current flow paths. Peak current density is seen to occur in corners and edges, where the peak current density is enhanced by sharp changes in current direction. Another close-up of the steel lid and overpack case, in the region of the lightning strike is shown in Figure 6-8. In this figure, the degree of current penetration into the metal lid can be easily seen. In this model, the lid is represented by ten elements, so that the penetration is not an artifact of the coarseness of the model. Below the lightning strike location, even with a thick steel lid, current penetration into the material below should be expected, at least locally. A profile of the power loss density along a path from the top of the cask to the concrete pad, through the pad and into the soil is shown in Figure 6-9. In this figure we see a large peak in power deposition at the cask-pad interface. This power will be deposited into the concrete and moisture contained therein at the surface of the concrete pad, potentially resulting in damage to the concrete pad.

The total power deposited in the concrete radiological shielding as a function of time, during the lightning strike pulse is shown in Figure 6-10 for grounded and ungrounded casks. While the profiles for the

19

grounded and ungrounded casks are similar, we see much higher power deposition into the concrete in the ungrounded cask than in the grounded cask. As a time-integrated total, there is on the order of three times as much power deposited in the concrete when the cask is not grounded. The instantaneous difference in power deposition between the two cases ranges from 0 to 12. Profiles of energy deposition into the concrete radial shielding, lid shielding, and lid ring shielding are shown in Figures 6-11, 6-12 and 6-13. The cases for which these three plots were made were all grounded and they are shown only to illustrate the differences in power deposition profiles in various regions of the model. The peak and average temperature profiles in the MPC contents are shown in Figures 6-14 and 6-15 for a grounded case. The predicted average temperature rise for this case is about 60° C with a peak temperature rise of about 800° C. Remembering that the MPC contents is homogenized, the peak temperature is not a reliable prediction, although the average temperature should be much better. In the MPC, the initial temperature is taken to be 394° C. These predicted temperatures are not sufficient to cause damage, although it might be expected that local hot-spots with temperatures beyond those predicted will develop because of the particular geometry and current flow details in the actual cask. Lightning strike location will play a large role in the location of the temperature peak within the MPC. In this case, the lightning strike is on the lid close to one side of the cask, and the peak MPC temperature occurs below this location adjacent to the side of the MPC shell about one-third of the way down from the top. A good relative comparison of power deposition in various regions of the model is shown in Figure 6-16. While the values from this 2-d simulation are not scaled to reflect azimuthal profiles, the plot gives a good indication of how power deposition changes from one region to another. The power deposited in the MPC is biased towards the side on which the current pulse was injected into the model. Power is seen propagating into the interior of the radial shielding and MPC from the outer surfaces. The highest power deposition is in the steel walls.
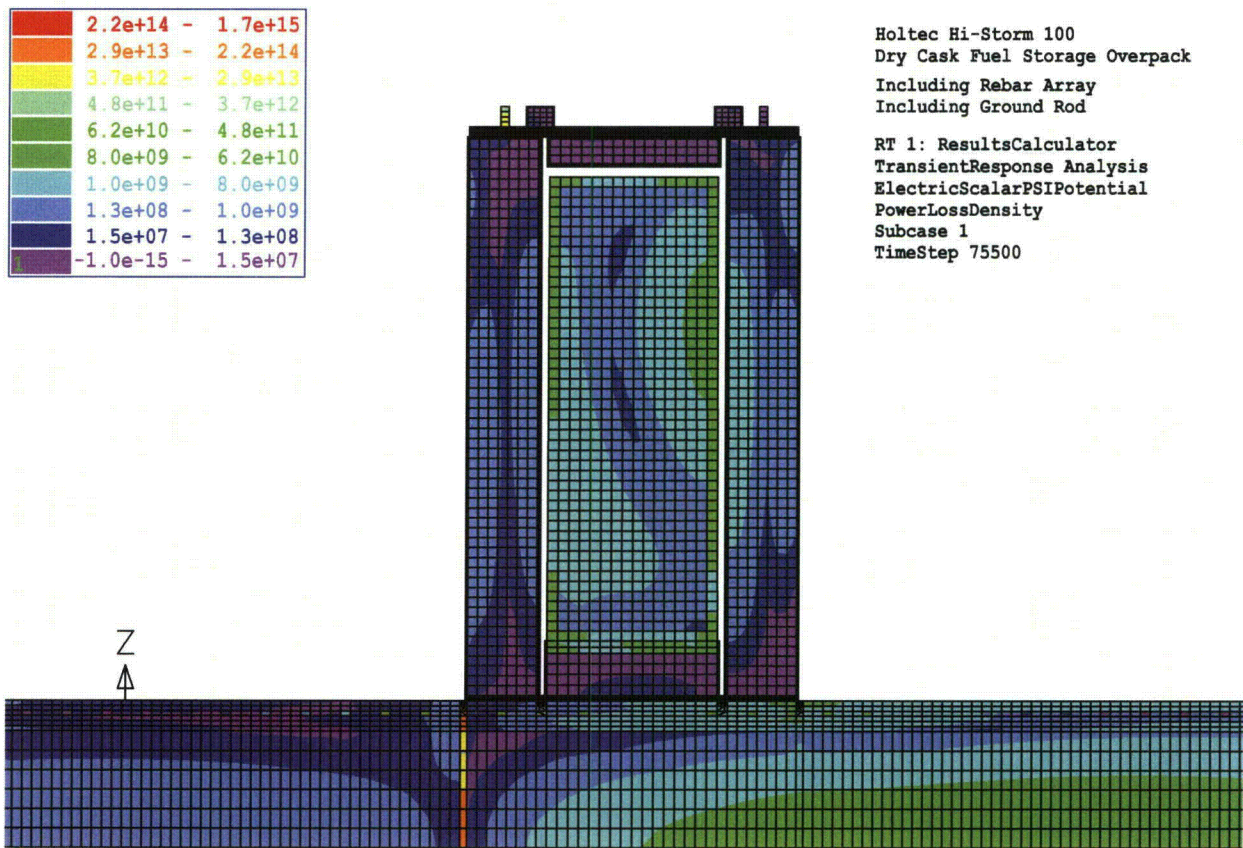
Figure 6-1. Power loss density in cask model, concrete pad and subsoil layer at a time near the peak of the lightning pulse. The ground connection through the concrete pad is visible.

Figure 6-2. Power deposition in non-metallic regions of the cask (MPC contents and concrete shielding). Case TR-02d: Grounded: Power loss density (W/m^3)

Figure 6-3. Power deposition in non-metallic regions of the cask (MPC contents and concrete shielding). Case TR-02c: Ungrounded: Power loss density (W/m^3).
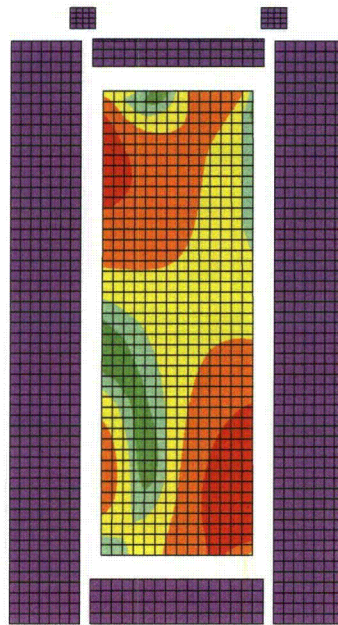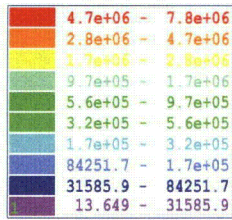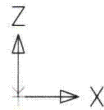
Figure 6-4. Total current density in the non-metallic regions of the cask (MPC contents and concrete shielding). Case TR-02d: Grounded: Current density (A/m^2).
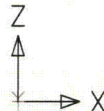
Figure 6-5. Total current density in the non-metallic regions of the cask (MPC contents and concrete shielding). Case TR-02c: Ungrounded: Current density (A/m^2).

4.1e+11 – 6.8e+11	
2.4e+11 – 4.1e+11	
1.4e+11 – 2.4e+11	
8.4e+10 – 1.4e+11	
4.9e+10 – 8.4e+10	
2.8e+10 – 4.9e+10	
1.5e+10 – 2.8e+10	
7.3e+09 – 1.5e+10	
2.7e+09 – 7.3e+09	
0.02105 – 2.7e+09	

Holtec Hi Storm 100
Dry Storage Cask
2-d Model
Transient Electromagnetic Analysis
Case TR-02d

RT 1: ResultsCalculator
TransientResponse Analysis
MagneticVectorPotential FullVector
GPTotalCurrentDensity FullVector
Subcase 1
TimeStep 0.00012
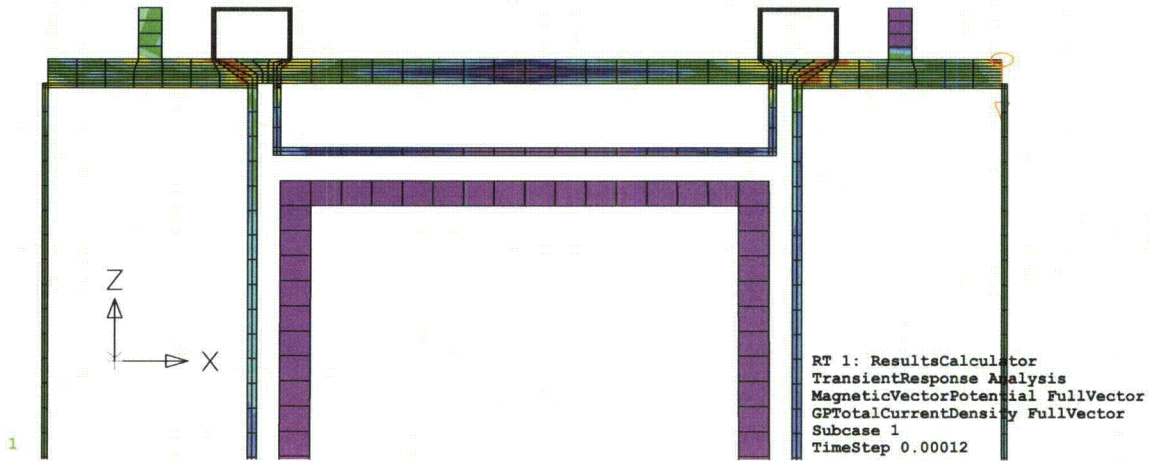
Figure 6-6. Metal shell of overpack, lid, and MPC shell. Case TR-02d: Grounded: Current density (A/m^2)

2.5e+11 – 4.2e+11	
1.5e+11 – 2.5e+11	
8.9e+10 – 1.5e+11	
5.2e+10 – 8.9e+10	
3.0e+10 – 5.2e+10	
1.7e+10 – 3.0e+10	
9.3e+09 – 1.7e+10	
4.6e+09 – 9.3e+09	
1.7e+09 – 4.6e+09	
0.13065 – 1.7e+09	

HOLTEC Hi-Storm 100
Dry Storage Cask
2-d Model
Transient Electromagnetic Analysis
Case Tr-02c

RT 1: ResultsCalculator
TransientResponse Analysis
MagneticVectorPotential FullVector
GPTotalCurrentDensity FullVector
Subcase 1
TimeStep 0.00012
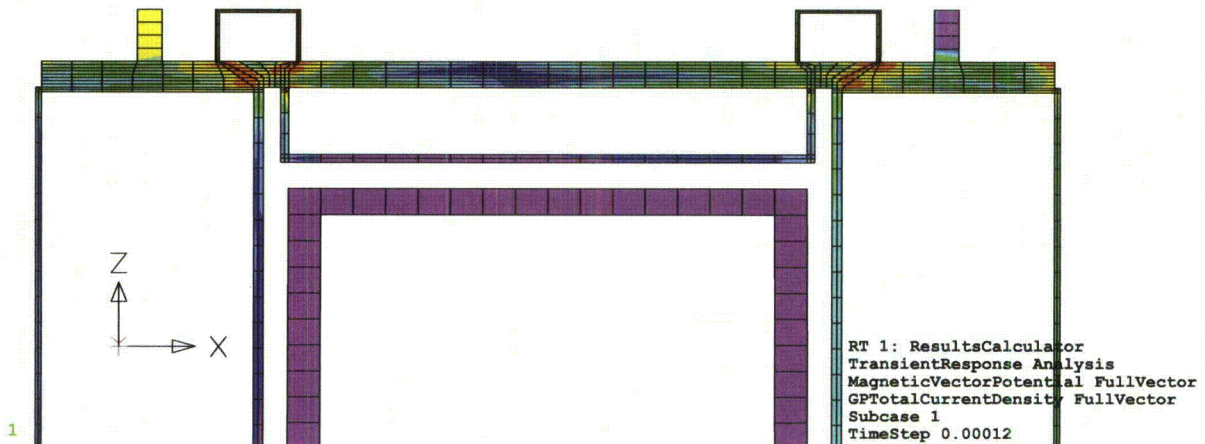
Figure 6-7. Metal shell of overpack, lid, and MPC shell. Case TR-02c: Ungrounded: Current density (A/m^2).

23

Holtec Hi-Storm 100
Dry Cask Fuel Storage Overpack
Including Rebar Array
Including Ground Rod

RT 1: ResultsCalculator
TransientResponse Analysis
MagneticVectorPotential FullVector
ConductionCurrentDensity FullVector
Subcase 1
TimeStep 1.0505e+06
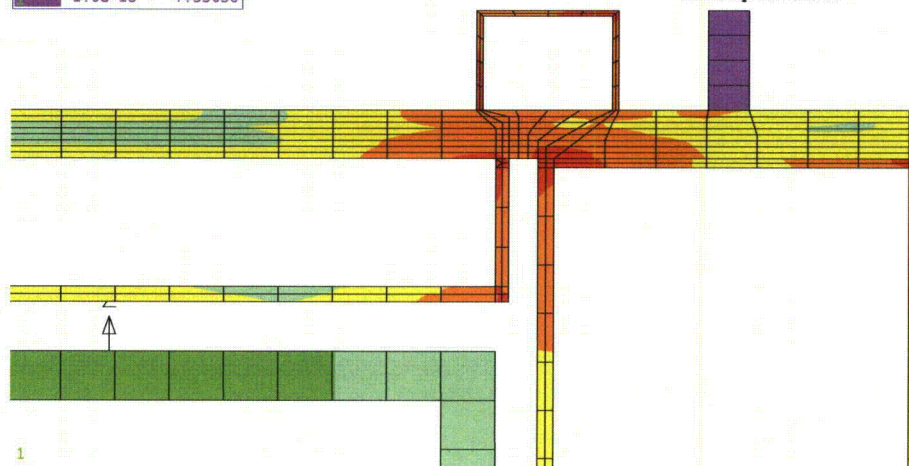
Figure 6-8. Conduction current density (A/m²) in a portion of the metal overpack and MPC walls, showing additional detail of current penetration through the carbon steel structure. Peak currents, for this case and time point occur at the corners on the inside of the lid. The time point for this plot is not the time of peak current for this case.

LEGEND
CutPath 6
PowerLossDensity - Instantaneous Results

Holtec Hi-Storm 100
Dry Cask Fuel Storage Overpack
No Rebar Array
No Ground Rod

CutPath 6 begins at the top of the cask, on the side opposite the lightning strike, and runs down the side of the cask to the pad, through the concrete pad and soil, to the ground plane.
EXCITATION:
Only 2kA, 1s pulse

<-- cask-pad interface

E+02
1.8
1.6
1.4
1.2
1
0.8
0.6
0.4
0.2
0
0   0.5   1   1.5   2   2.5   3 E+02
Path

<-- Top of Cask

Figure 6-9. Power density profile on outside edge of overpack from the top of the cask to the bottom through the concrete pad and into the subsoil.

Total Power Deposited in Concrete Radial Shielding
for Grounded and Ungrounded Casks
(2-d model)
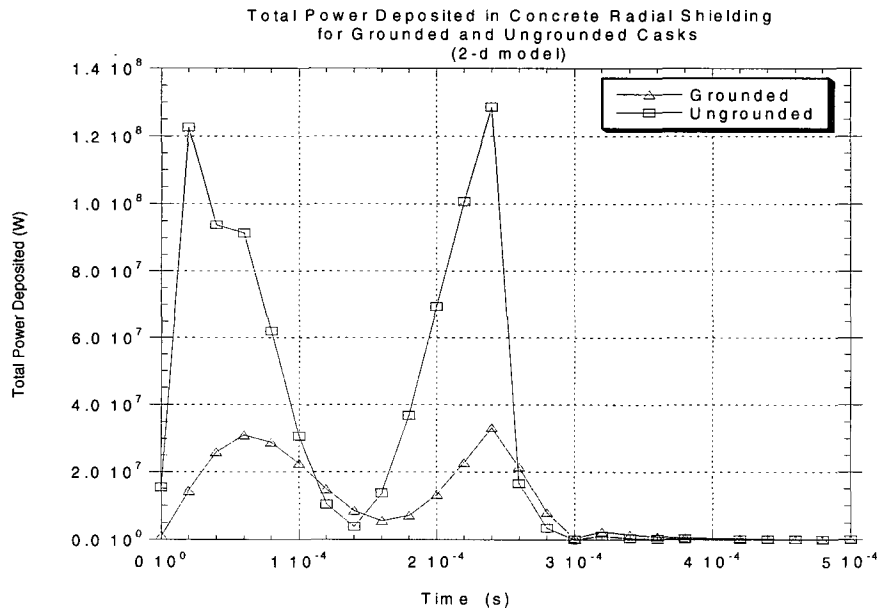
Figure 6-10. Comparison of the time history of power deposition in the concrete radiological shielding in grounded and ungrounded dry storage casks. The integrated power deposition in the ungrounded cask is a factor of 3 higher than in the grounded cask.

Total Energy Deposited in Radial Concrete Shielding
During Simulated Lightning Strike
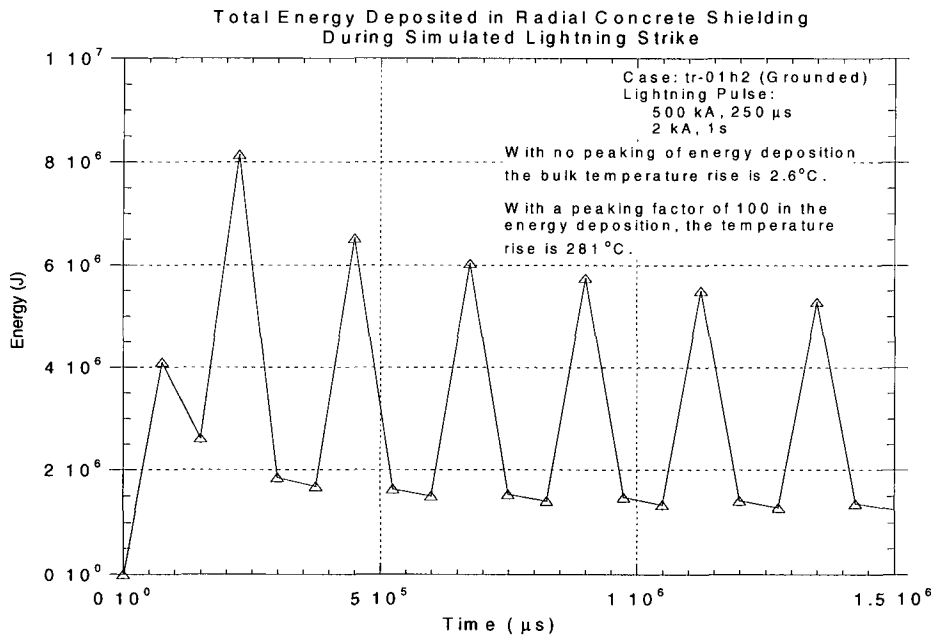
Figure 6-11. Temporal profile of energy deposition in the radial concrete shielding, assuming uniform energy distribution throughout the concrete.

25
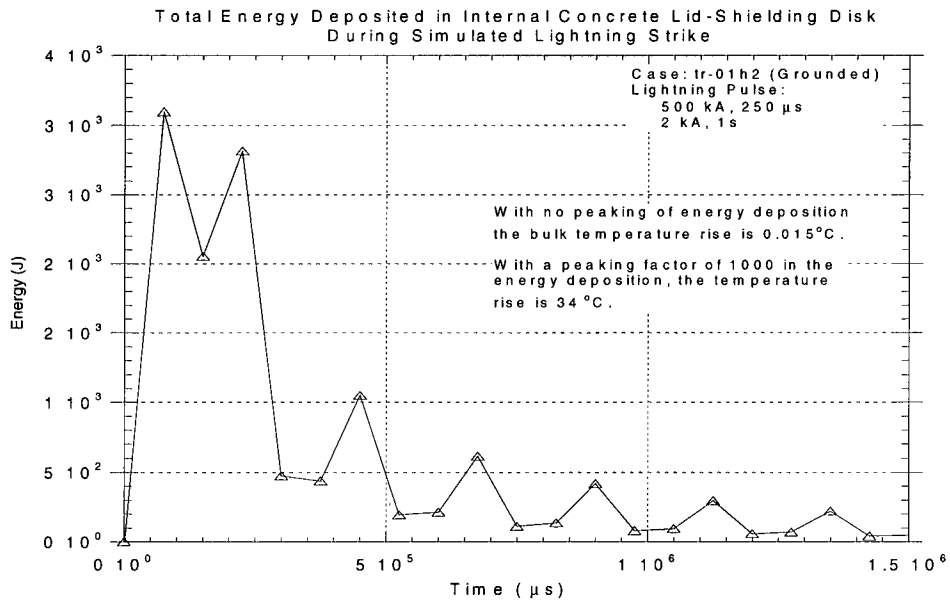
Figure 6-12. Temporal energy deposition in the internal concrete lid-shielding disk, assuming that the energy is uniformly spread throughout the concrete shielding.
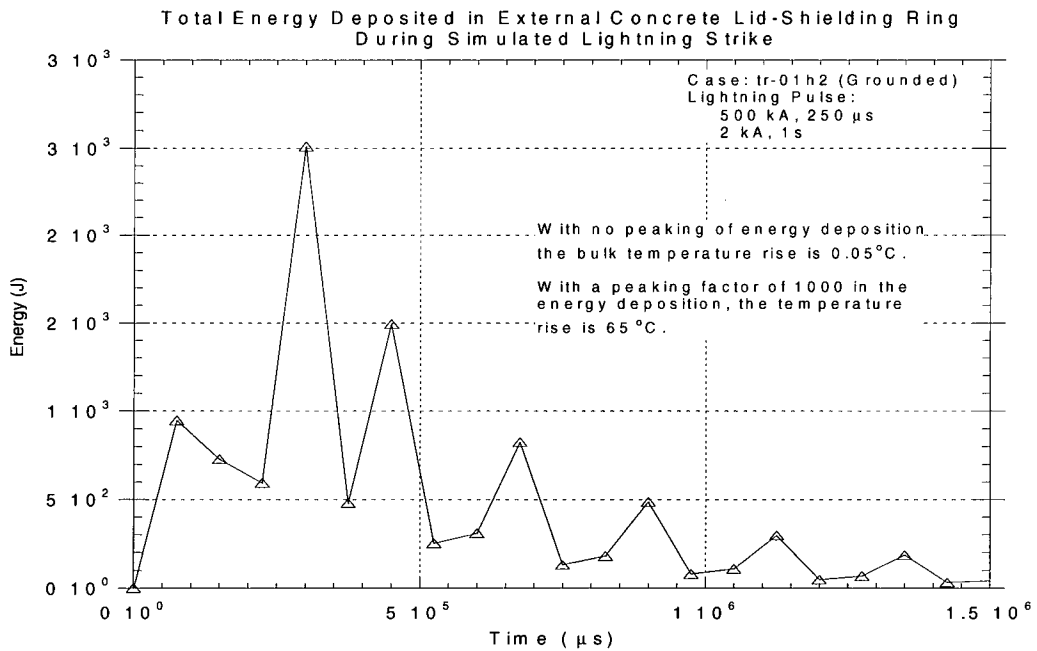
Figure 6-13. Temporal energy deposition in the external concrete lid-shielding ring, assuming that the energy is uniformly spread throughout the concrete.

26
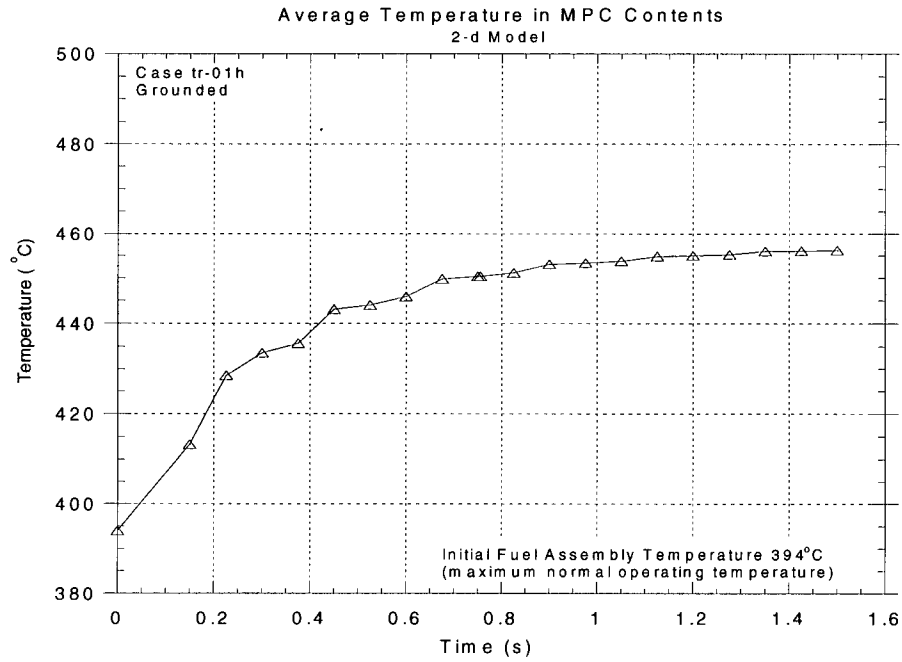
Figure 6-14. Average temperature in the homogenized MPC assuming uniform energy distribution throughout the MPC.
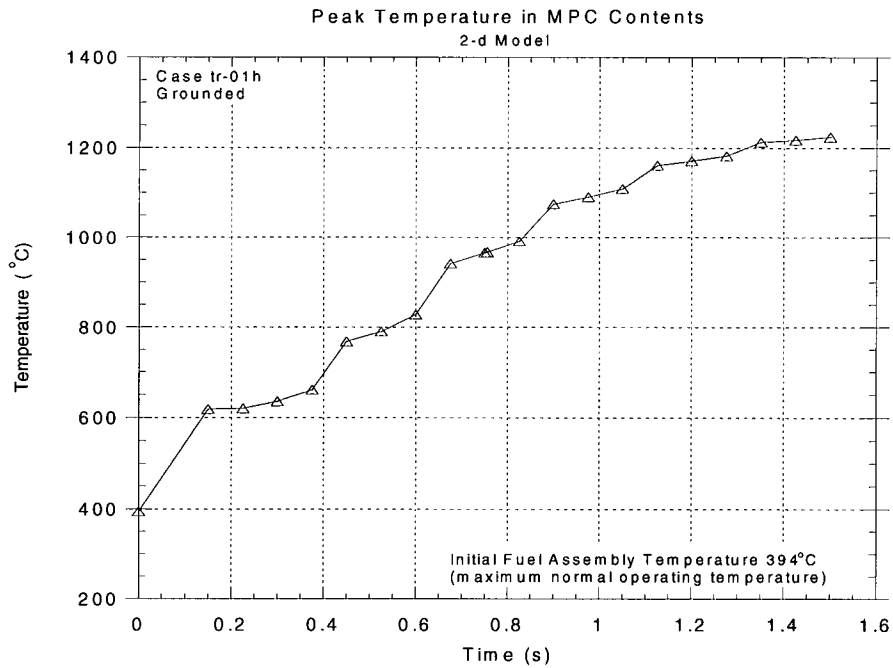
Figure 6-15. Peak Temperature profile in the hottest location of the MPC model. This location is on the side of the MPC contents, adjacent to the steel wall, one-third of the way down from the top.

27
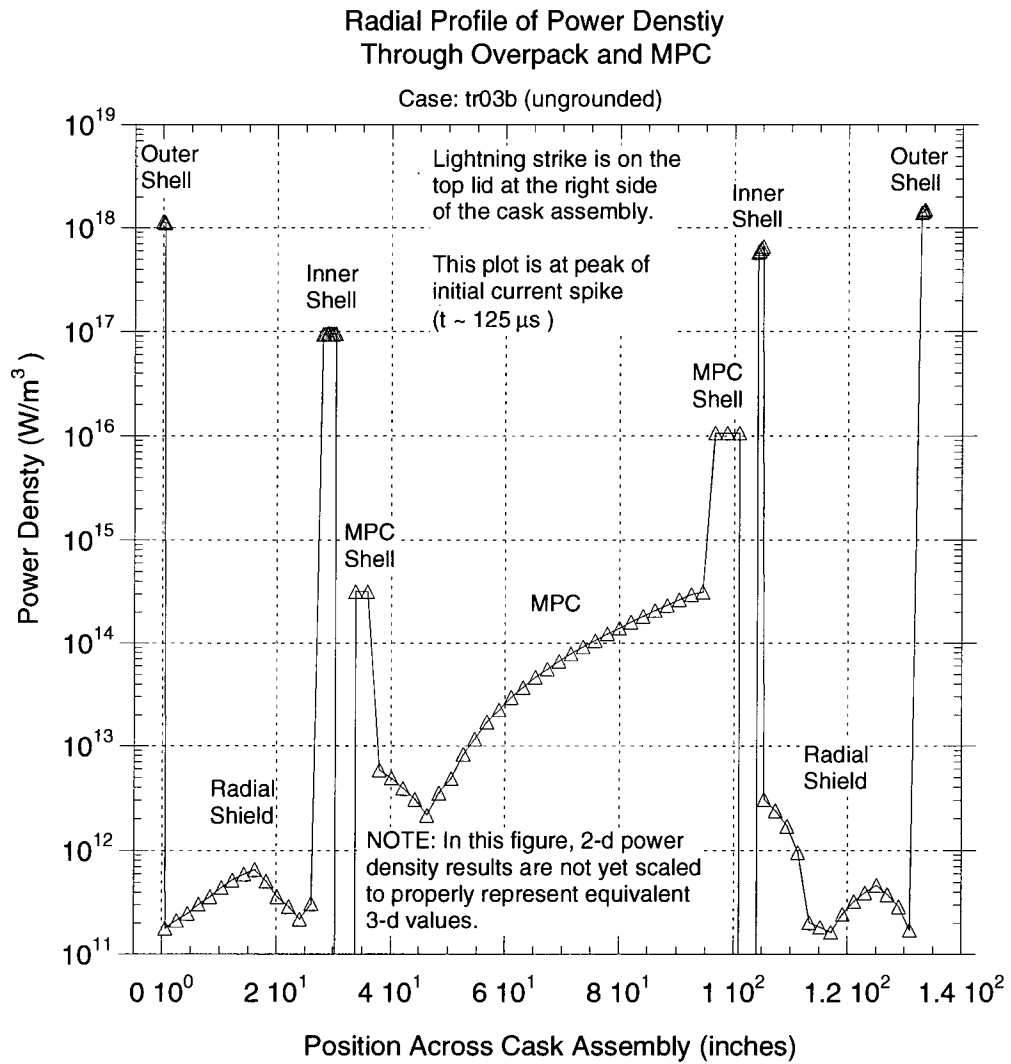
Figure 6-16. Power density along a horizontal path through the 2-d model at a particular time and at a particular vertical location. While this shows the relative values of power deposited, it has not been scaled to represent properly the 3-d values. .

6.2 Transient Results from the 3-d Cask Model

The 3-d model of the cask is greatly simplified, compared to the 2-d model. While this model yielded useful power deposition results for the radial shielding, overpack shell, MPC shell and MPC contents, its primary purpose was to determine the proper azimuthal scaling function for use with 2-d simulation results. Plots of power deposition contours for each of the primary regions of the model are given here at the time of peak power deposition for one of the model configurations (ungrounded). These contour plots give some insight into how the power is distributed between regions and within regions.

6.2.1 Azimuthal Profiles

The 2-d models that were evaluated did not yield information about the variation of power deposition in the azimuthal direction. From the simplified cask model a rough idea of the degree of power deposition localization was obtained. Figure 6-17 shows the azimuthal profile of power deposited in the concrete radiological shielding at one time point. The profile changes with time but generally maintains a shape consistent with that shown. However, the power deposition on the surface of the outer shell is much more localized, as can be seen from some of the 3-d color contour plots. As power penetrates inward, it broadens considerable and becomes generally quite smooth. A single azimuthal profile was chosen for each region and used to scale the corresponding 2-d simulation results.

A cross section cut through the 3-d cask model is shown in Figure 6-18. The principal regions of the model are the MPC contents, a steel shell representing the combined MPC outer shell and overpack inner shell, the concrete radiological shielding, and the outer steel overpack shell. Figure 6-18 also shows power deposition density in the various regions of the model. Although it cannot be seen in this figure, because of the scale, the peak power deposition is in the thin steel layers of the overpack shell and MPC shell. Figures 6-19 to 6-22 are all top views of the power deposition in the principal components of the 3-d cask model at the time of peak power deposition. For each respective region, the surface shown is the closest to the lightning strike location.

Figure 6-19	Power deposition in the top surface of the outer shell of the overpack.
Figure 6-20	Power deposition on the top surface of the concrete shielding within the overpack.
Figure 6-21	Power deposition into the steel layer representing the combined MPC outer shell and overpack inner shell.
Figure 6-22	Power deposition into the top surface of the homogenized MPC contents.

Figures 6-23 to 6-26 are all perspective views of the power deposition in the principal components of the 3-d cask model at the time of peak power deposition. These figures are of the same regions and at the same times as Figures 6-19 to 6-22

Figure 6-23	Power deposition in the top surface of the outer shell of the overpack.
Figure 6-24	Power deposition on the top surface of the concrete shielding within the overpack.
Figure 6-25	Power deposition into the steel layer representing the combined MPC outer shell and overpack inner shell.
Figure 6-26	Power deposition into the top surface of the homogenized MPC contents.
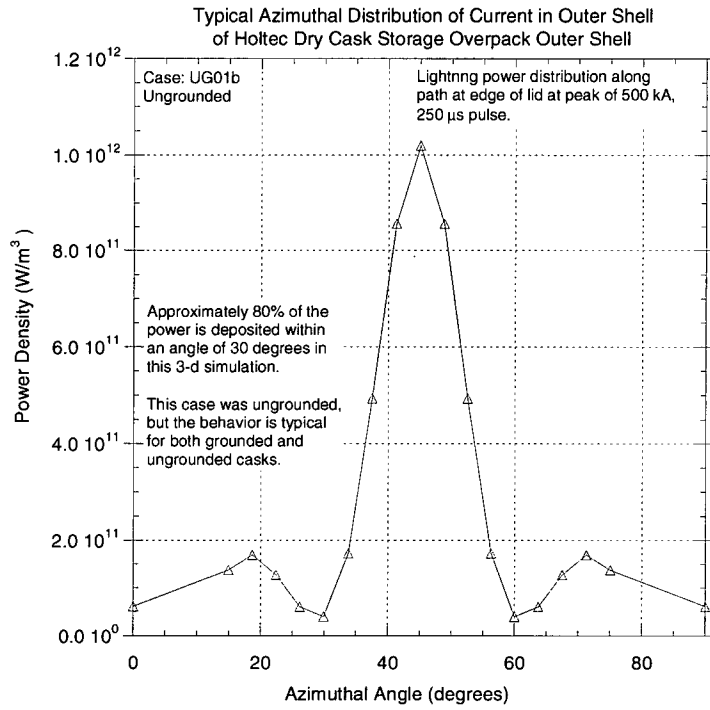
Figure 6-17. Calculated azimuthal profile of power deposition in the outer shell of the storage cask overpack.

	7.0e+10 - 4.2e+11
	1.2e+10 - 7.0e+10
	1.9e+09 - 1.2e+10
	3.2e+08 - 1.9e+09
	5.4e+07 - 3.2e+08
	9.0e+06 - 5.4e+07
	1.5e+06 - 9.0e+06
	2.3e+05 - 1.5e+06
	22306.6 - 2.3e+05
	-12518.1 - 22306.6
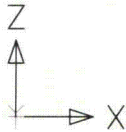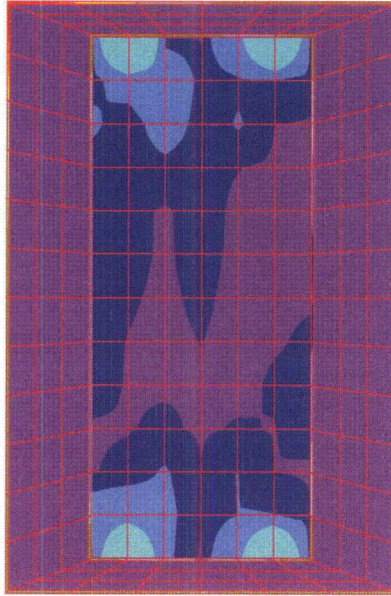
Z
X

RT 1: ResultsCalculator
TransientResponse Analysis
MagneticVectorPotential FullVector
GPPowerLossDensity
Subcase 1
TimeStep 0.00014

Figure 6-18. Current Density on a plane, cut through the simplified cask model. The outer purple region is concrete, central region is the MPC and the metal walls, containing the highest current density, barely visible because of their thinness.
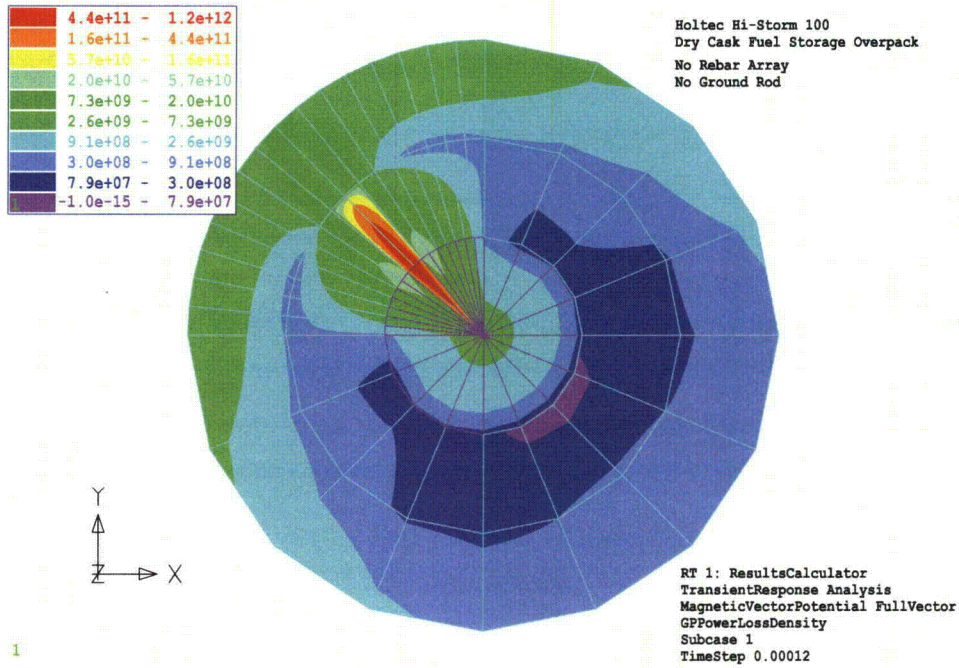
Figure 6-19. Power deposition in outer shell of the overpack in the 3-d cask model.
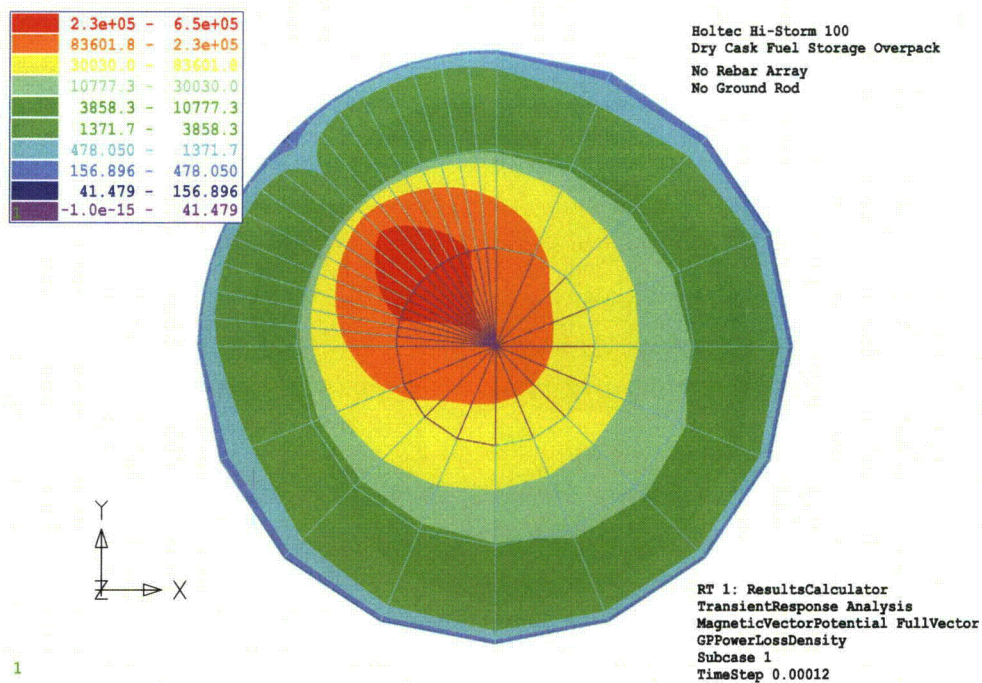
Figure 6-20. Power deposition in the concrete radiological shielding in the 3-d cask model.
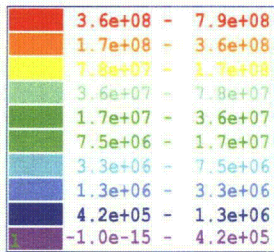
3.6e+08	7.9e+08
1.7e+08	3.6e+08
7.8e+07	1.7e+08
3.6e+07	7.8e+07
1.7e+07	3.6e+07
7.5e+06	1.7e+07
3.3e+06	7.5e+06
1.3e+06	3.3e+06
4.2e+05	1.3e+06
-1.0e-15	4.2e+05

Holtec Hi-Storm 100
Dry Cask Fuel Storage Overpack

No Rebar Array
No Ground Rod
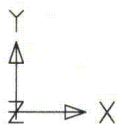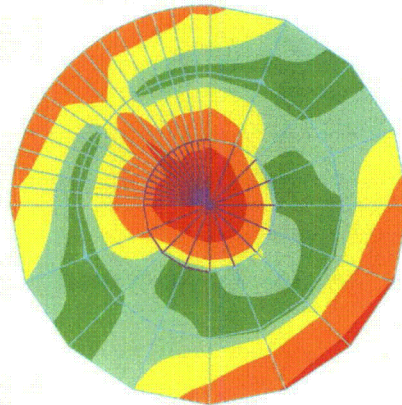
RT 1: ResultsCalculator
TransientResponse Analysis
MagneticVectorPotential FullVector
GPPowerLossDensity
Subcase 1
TimeStep 0.00012

Figure 6-21. Power deposition in outer shell of the MPC in the 3-d cask model
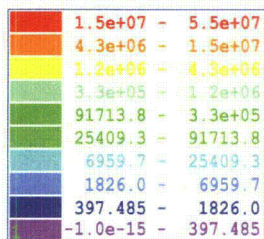
1.5e+07	5.5e+07
4.3e+06	1.5e+07
1.2e+06	4.3e+06
3.3e+05	1.2e+06
91713.8	3.3e+05
25409.3	91713.8
6959.7	25409.3
1826.0	6959.7
397.485	1826.0
-1.0e-15	397.485

Holtec Hi-Storm 100
Dry Cask Fuel Storage Overpack

No Rebar Array
No Ground Rod
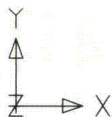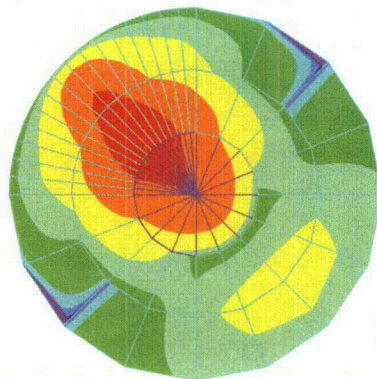
RT 1: ResultsCalculator
TransientResponse Analysis
MagneticVectorPotential FullVector
GPPowerLossDensity
Subcase 1
TimeStep 0.00012

Figure 6-22. Power deposition in the MPC contents in the 3-d cask model.
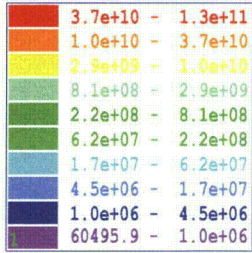
■	3.7e+10 -	1.3e+11
■	1.0e+10 -	3.7e+10
■	2.9e+09 -	1.0e+10
■	8.1e+08 -	2.9e+09
■	2.2e+08 -	8.1e+08
■	6.2e+07 -	2.2e+08
■	1.7e+07 -	6.2e+07
■	4.5e+06 -	1.7e+07
■	1.0e+06 -	4.5e+06
■	60495.9 -	1.0e+06

Holtec Hi-Storm 100
Dry Cask Fuel Storage Overpack

No Rebar Array
No Ground Rod
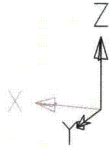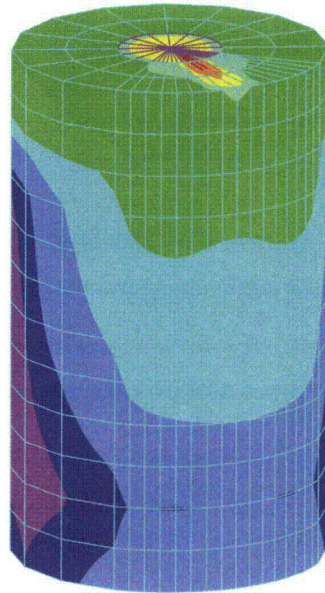
RT 1: ResultsCalculator
TransientResponse Analysis
MagneticVectorPotential FullVector
PowerLossDensity
Subcase 1
TimeStep 0.00013

Figure 6-23. Power deposition in the outer shell of overpack in the 3-d cask model.
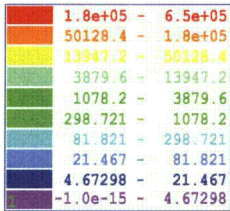
■	1.8e+05 -	6.5e+05
■	50128.4 -	1.8e+05
■	13947.2 -	50128.4
■	3879.6 -	13947.2
■	1078.2 -	3879.6
■	298.721 -	1078.2
■	81.821 -	298.721
■	21.467 -	81.821
■	4.67298 -	21.467
■	-1.0e-15 -	4.67298

Holtec Hi-Storm 100
Dry Cask Fuel Storage Overpack

No Rebar Array
No Ground Rod
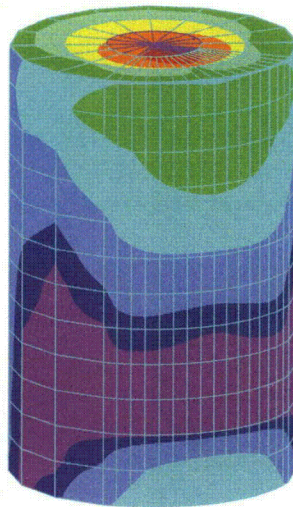
RT 1: ResultsCalculator
TransientResponse Analysis
MagneticVectorPotential FullVector
GPPowerLossDensity
Subcase 1
TimeStep 0.00012

Figure 6-24. Power deposition in concrete radiological shielding in the 3-d cask model.
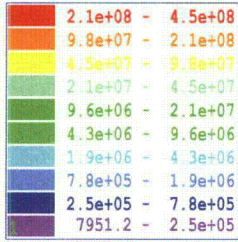
2.1e+08	-	4.5e+08
9.8e+07	-	2.1e+08
4.5e+07	-	9.8e+07
2.1e+07	-	4.5e+07
9.6e+06	-	2.1e+07
4.3e+06	-	9.6e+06
1.9e+06	-	4.3e+06
7.8e+05	-	1.9e+06
2.5e+05	-	7.8e+05
7951.2	-	2.5e+05

Holtec Hi-Storm 100
Dry Cask Fuel Storage Overpack

No Rebar Array
No Ground Rod
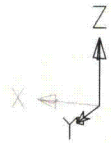
RT 1: ResultsCalculator
TransientResponse Analysis
MagneticVectorPotential FullVector
PowerLossDensity
Subcase 1
TimeStep 0.00013

Figure 6-25. Power deposition in steel MPC shell in the 3-d cask model.
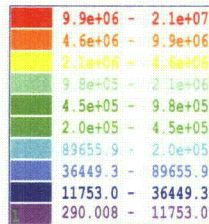
9.9e+06	-	2.1e+07
4.6e+06	-	9.9e+06
2.1e+06	-	4.6e+06
9.8e+05	-	2.1e+06
4.5e+05	-	9.8e+05
2.0e+05	-	4.5e+05
89655.9	-	2.0e+05
36449.3	-	89655.9
11753.0	-	36449.3
290.008	-	11753.0

Holtec Hi-Storm 100
Dry Cask Fuel Storage Overpack

No Rebar Array
No Ground Rod
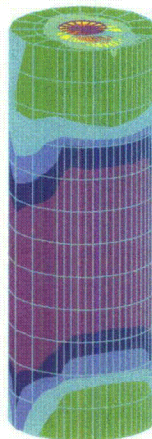
RT 1: ResultsCalculator
TransientResponse Analysis
MagneticVectorPotential FullVector
PowerLossDensity
Subcase 1
TimeStep 0.00013

Figure 6-26. Power deposition in homogenized MPC contents in the 3-d cask model.

6.3 Results from 3-d Cylinder Model

The 3-d cylinder model was excited at the center of the top lid with a current profile of the same type as the storage cask models. The excitation pulse includes both the high-current, short-duration pulse and the low-current, long-duration pulse. A triangular pulse of 250 μs duration and 500 kA peak current plus a 0.5 s, 5 kA pulse is injected into the lid of the cylinder model. The early portion of the excitation pulse is shown in Figure 6-27. Figures 6-28 and 6-29 are contour plots of the current density in the individual regions of the cylinder model at the time of peak power deposition. Figure 6-28 shows the current density in the carbon steel lid and side walls. The peak current regions are at the site of the lightning strike, at the center of the lid, and along the outer top edge of the lid. In the carbon steel regions, the peak current reaches a value of 7.6×10^{11} A/m^3. The predicted current density in the concrete interior of the model is shown in Figure 6-29 As seen, the current density in the concrete is much smaller than in the metal shell. In the concrete, the peak current region is just below the lightning strike location. The peak current density in the concrete is 3139 A/m^3, a factor of 2.4×10^5 lower than in the steel. Tabulated in Table 6-1 are the threshold levels of power deposition (W/m^3) to cause a detectable temperature change in concrete and in carbon steel. Also tabulated are the power densities required for the onset of damage to these materials. In carbon steel, the onset of damage is defined to be onset of melting. In concrete, the onset of damage is defined to be the vaporization of free water contained in the concrete. This criteria may not actually cause damage if the vaporized water is free to expand so that no pressure is built up.

The peak power deposition in the three regions of this model are shown in Figures 6-30 to 6-32. From Figure 6-30, we see that the peak power deposition is 1.0×10^8 W/m3 and occurs at the location just below the lightning strike location. This power density is just sufficient to make a discernable temperature change in the concrete. The peak power density deposited in the carbon steel shell is shown in Figure 6-31. In the steel shell, the peak power density is seen to be about 4.7×10^{16} W/m3. Comparing this with the power density necessary for damage (given in Table 6-1), we see that the peak power density deposited in the model is some 3000 times the threshold temperature for damage. Clearly localized damage is going to occur on the steel lid, although a significant amount of energy will be absorbed by melting, vaporizing, and sputtering of the steel. Power deposition in the complete cylinder model is shown in Figure 6-32. In this figure, the comparison of power deposition in the steel and concrete is easier since the same scale is imposed.

Table 6-1. Power density required for a detectable temperature change and for damage in concrete and carbon steel.

| Cask region | Required power density for 500 μs (W/m^3) | |
	Detectable temperature change	Damage threshold
Carbon Steel	5.0×10^9	1.6×10^{13}
Concrete	1.0×10^9	1.5×10^{11}

Figures 6-33 to 6-37 show power deposition and current density along several paths of interest through the model. Cut Path 1 begins at the lightning strike location at the center of the top lid and proceeds radially outward to the edge of the top lid, and partway down the side of the cylinder. Cut Path 5 begins at the top edge of the lid and proceeds downward along the outside surface of the cylinder to the bottom of the cylinder. Cut Path 6 is a horizontal path just below the steel lid from the center of the model, through the concrete and through the cylinder side wall. In general, we see smooth profiles except at the edge of the lid where the sharp corner enhances the current density and power deposition.

Figure 6-33	Current density along a horizontal path (Cut Path 1) on the top surface of the steel lid.
Figure 6-34	Current density along a vertical path (Cut Path 5) down the side of the cylinder.
Figure 6-35	Current density along a horizontal path (Cut Path 6) through the concrete and steel side wall, just under the lid.

Figures 6-36 to 6-38 show the power deposition along the same set of paths through the model for which current density was previously shown. We see from these profiles and comparison with the threshold values given in Table 6-1, that the concrete will not experience a temperature rise, pressure rise, or any damage due to the lightning strike. The steel lid, however, has greatly exceeded the threshold power density for damage. The volume of material affected is small, but an accurate evaluation of the damaged volume will require analysis, including the details of melting, vaporization, and sputtering because these are highly nonlinear processes.

Figure 6-36	Power deposition along a horizontal path (Cut Path 1) on the top surface of the lid.
Figure 6-37	Power deposition along a vertical path (Cut Path 5) down the side of the cylinder.
Figure 6-38	Power deposition along a horizontal path (Cut Path 6) through the concrete and steel side wall, just under the lid.
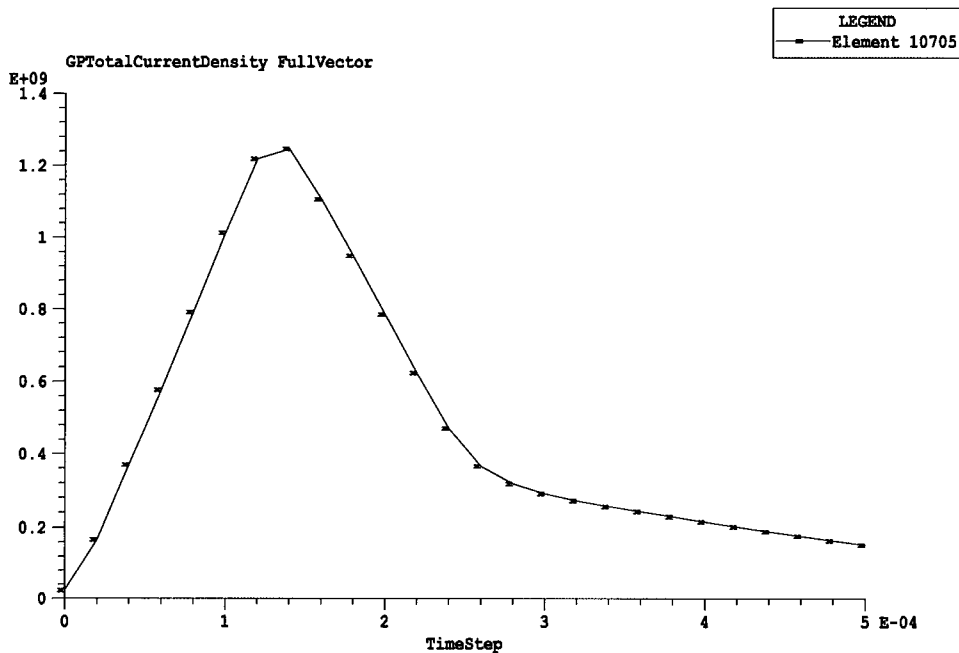
Figure 6-27. Time profile of the current excitation on the top, center of the lid.
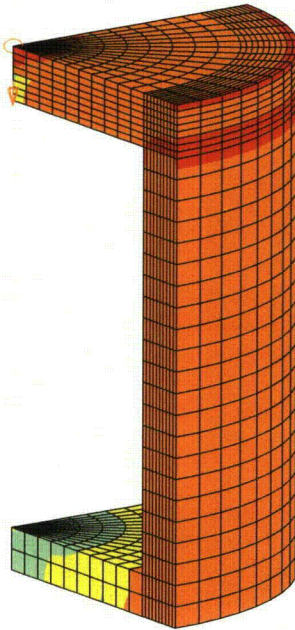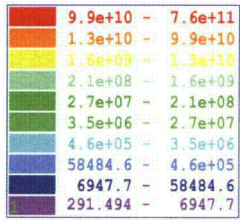
9.9e+10	7.6e+11
1.3e+10	9.9e+10
1.6e+09	1.3e+10
2.1e+08	1.6e+09
2.7e+07	2.1e+08
3.5e+06	2.7e+07
4.6e+05	3.5e+06
58484.6	4.6e+05
6947.7	58484.6
291.494	6947.7

RT 1: ResultsCalculator
TransientResponse Analysis
MagneticVectorPotential FullVector
GPTotalCurrentDensity FullVector
Subcase 1
TimeStep 0.00014

Figure 6-28. Current density in steel shell of cylinder model at the time of peak power deposition.
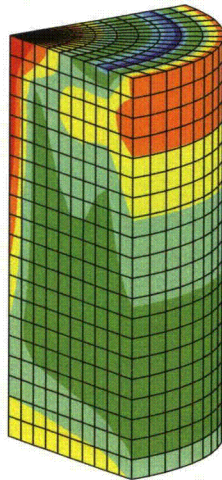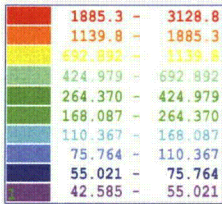
1885.3	3128.8
1139.8	1885.3
692.892	1139.8
424.979	692.892
264.370	424.979
168.087	264.370
110.367	168.087
75.764	110.367
55.021	75.764
42.585	55.021

RT 1: ResultsCalculator
TransientResponse Analysis
MagneticVectorPotential FullVector
GPTotalCurrentDensity FullVector
Subcase 1
TimeStep 0.00014

Figure 6-29. Current density profiles in the concrete interior of cylinder model at the time of peak power deposition.

38

6.0e+07	1.0e+08
3.6e+07	6.0e+07
2.1e+07	3.6e+07
1.3e+07	2.1e+07
7.3e+06	1.3e+07
4.1e+06	7.3e+06
2.2e+06	4.1e+06
1.1e+06	2.2e+06
4.1e+05	1.1e+06
-1.0e-15	4.1e+05
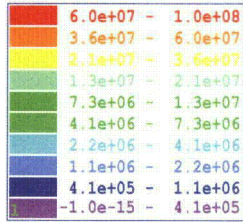
SIMPLE CYLINDRICAL CAN WITH LID

1-in wall,lid thicknesses
Interior: 8-in diam., 10-in height
Can walls: Carbon Steel
Can Fill: Concrete
Perfect ground plane at base
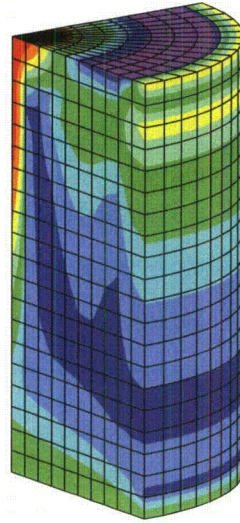
RT 1: ResultsCalculator
TransientResponse Analysis
MagneticVectorPotential FullVector
GPPowerLossDensity
Subcase 1
TimeStep 0.00014

Figure 6-30. Power deposition profiles in the concrete at the time of peak power deposition.
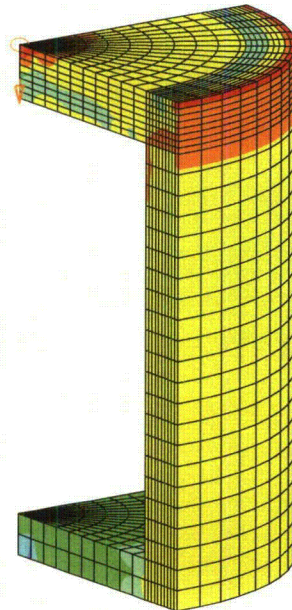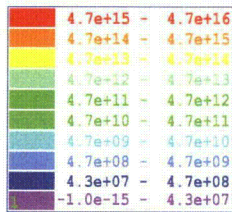
4.7e+15	4.7e+16
4.7e+14	4.7e+15
4.7e+13	4.7e+14
4.7e+12	4.7e+13
4.7e+11	4.7e+12
4.7e+10	4.7e+11
4.7e+09	4.7e+10
4.7e+08	4.7e+09
4.3e+07	4.7e+08
-1.0e-15	4.3e+07

RT 1: ResultsCalculator
TransientResponse Analysis
MagneticVectorPotential FullVector
GPPowerLossDensity
Subcase 1
TimeStep 0.00014

Figure 6-31. Power deposition in the steel shell of the cylinder model at the time of peak power deposition.
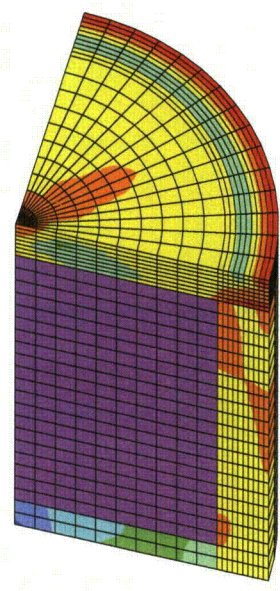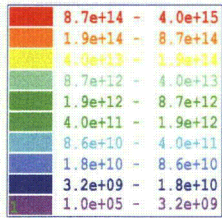
Figure 6-32. Power deposition in the complete cylinder model at the time of peak power deposition.
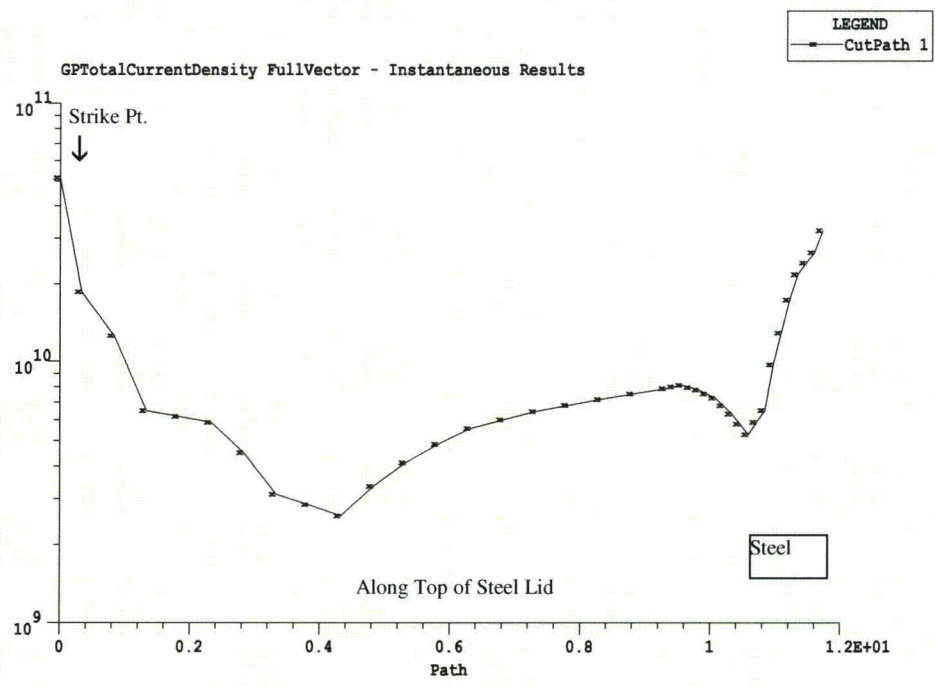
Figure 6-33. Current density along the top of the lid from the center to the outer edge.

GPTotalCurrentDensity FullVector - Instantaneous Results

Top   Along Vertical Edge of Can   Bottom
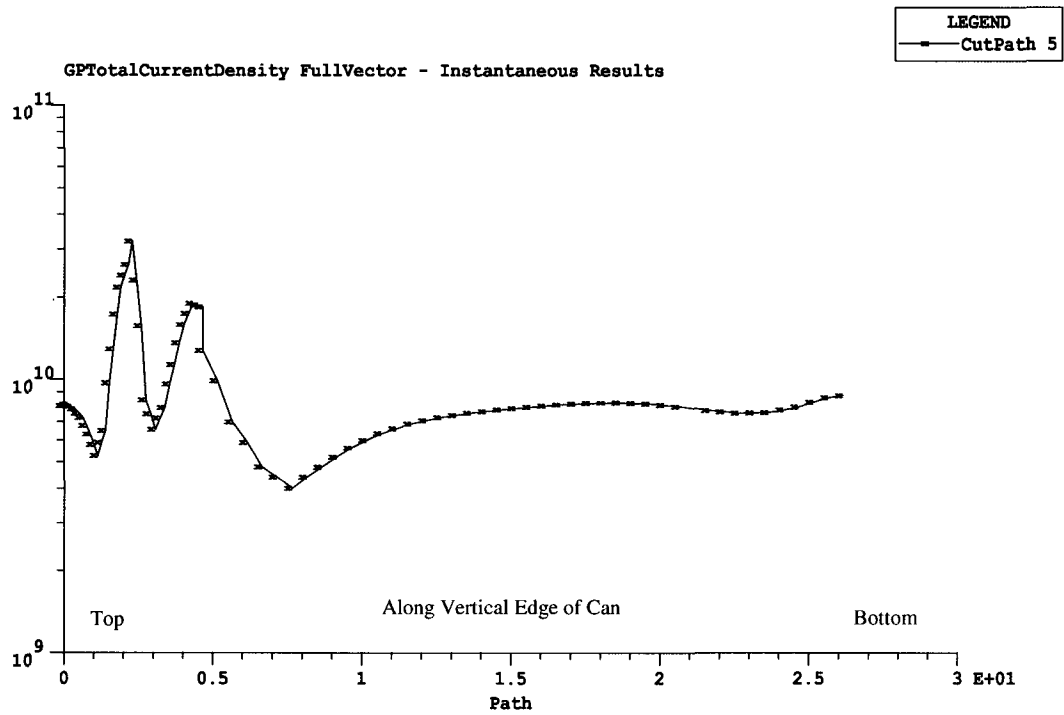
Figure 6-34. Current density along the vertical outer edge of the can from the top to bottom. The top edge of the can is on the left.
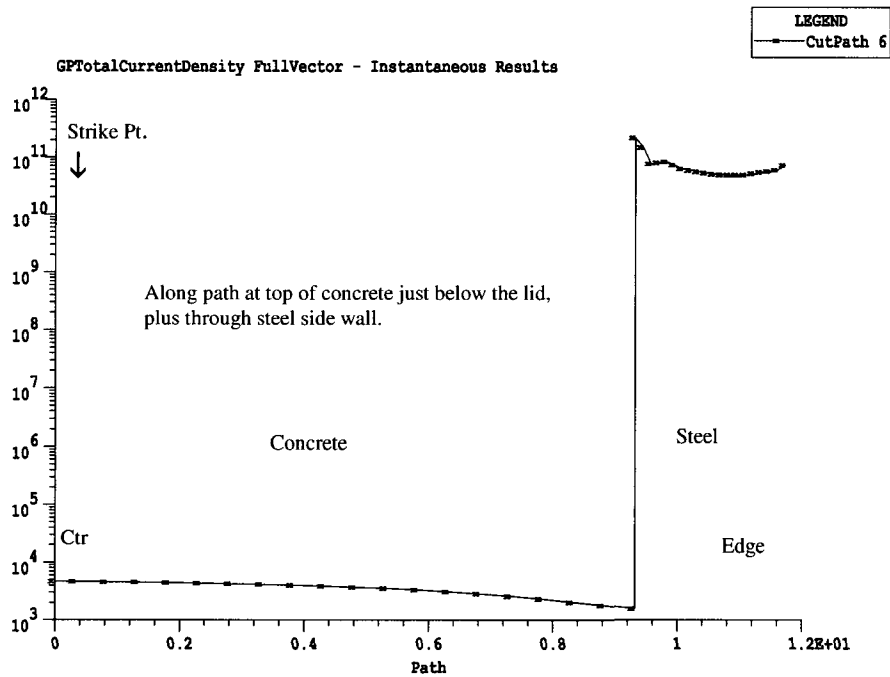
GPTotalCurrentDensity FullVector - Instantaneous Results

Strike Pt.

Along path at top of concrete just below the lid, plus through steel side wall.

Concrete   Steel

Ctr   Edge

Figure 6-35. Current density along a horizontal path through concrete and steel side wall just below the lid.

41

GPPowerLossDensity - Instantaneous Results
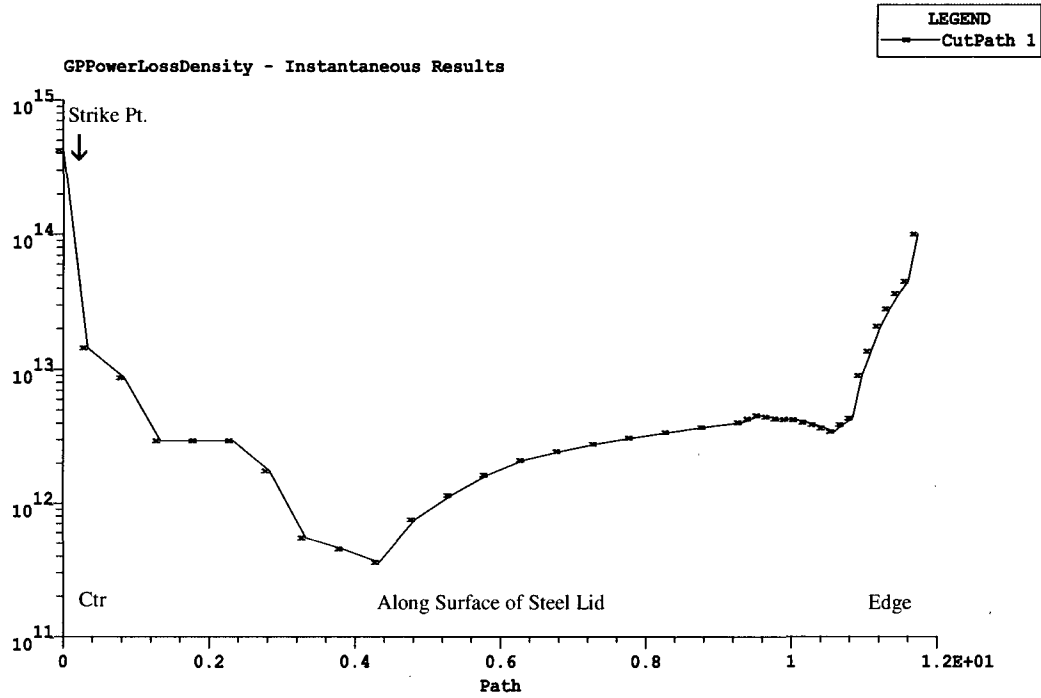
Figure 6-36. Power loss density along the top of the lid from the center to the outer edge.

GPPowerLossDensity - Instantaneous Results
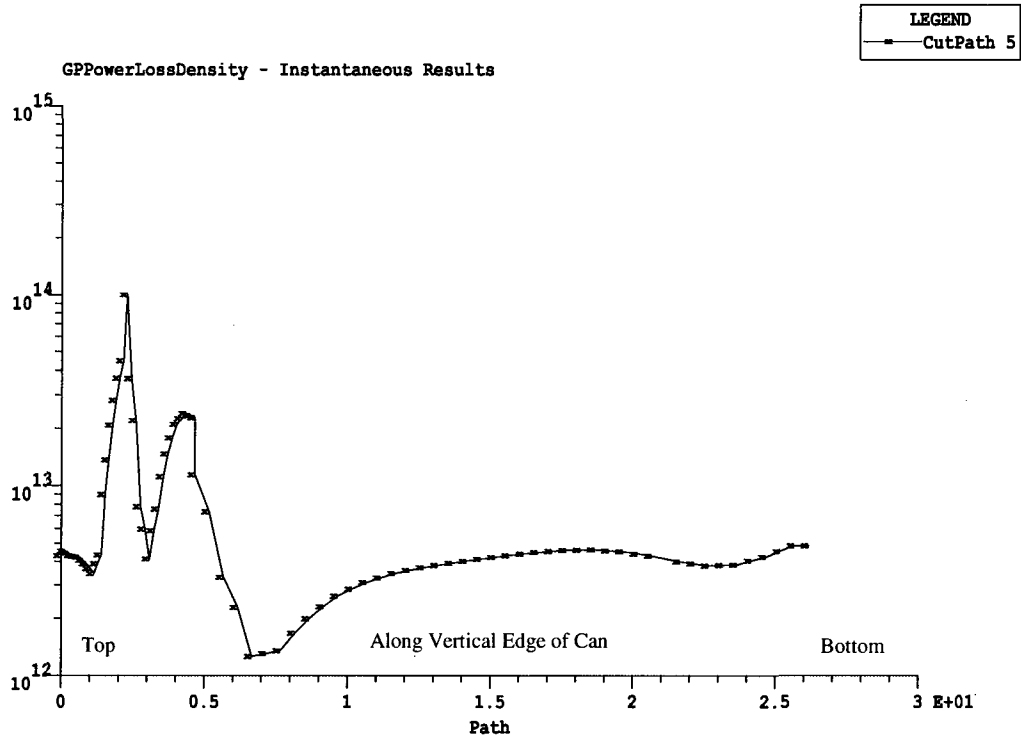
Figure 6-37. Power deposition along the vertical outer edge of the can from the top to bottom.
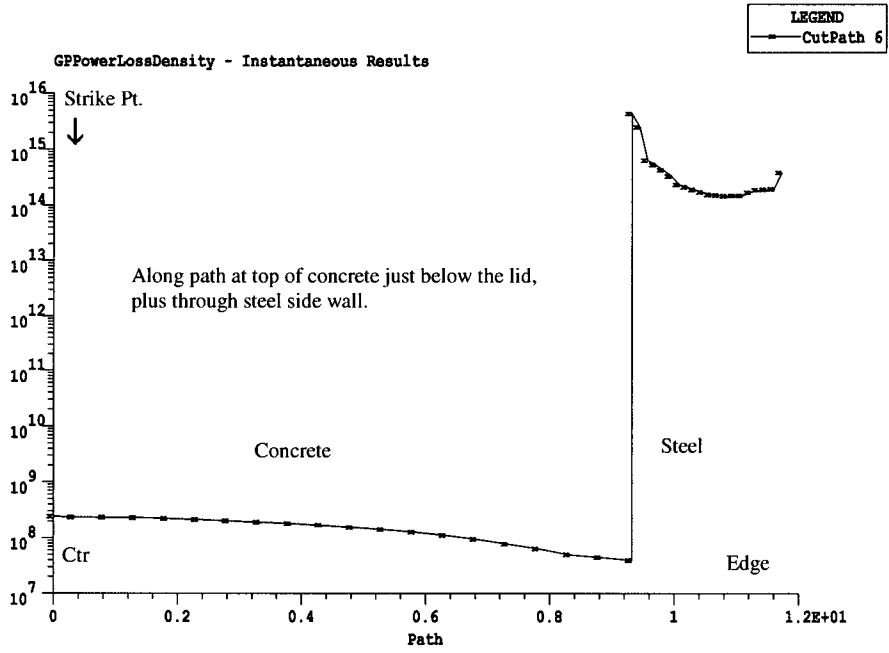
Figure 6-38. Power deposition along path through concrete and steel side wall just below the lid.

7. SUMMARY AND CONCLUSIONS

7.1 Summary

The parameters chosen in the simulations that were performed are thought to be representative of the materials and conditions expected in an actual lightning strike on a Holtec dry storage cask. However, many of the parameters and conditions can vary widely. These conditions include both material properties and lightning strike parameters. Needless to say, with the compressed schedule for these calculations, there was almost no exploration of the effects of the likely range of parameters on the results. Because of this, no error bounds can be placed on the results although it is thought that the parameters chosen represent worst-case scenarios. What we have obtained is an understanding of power deposition in a simplified geometry with one particular set of material properties and under the conditions imposed by a lightning strike with a particular set of parameters. That these simulations indicate the absence of structural damage to the cask is encouraging but not conclusive.

MPC Power Deposition

In all models that were evaluated, the MPC contents were homogenized and average properties were used for the analyses, both electrical and thermal. Because the complexity of the actual MPC contents was not represented in the models, it is likely that power deposition in the MPC that was calculated by all of the models is overestimated. The many small gaps within the MPC will prevent currents from flowing as calculated in the models. In addition, there is considerably less actual contact between the MPC contents and MPC shell than is represented in the models. Analysis of both grounded and ungrounded casks predict that insufficient power is deposited within the MPC contents to cause temperature increases that could cause internal damage or rupture of the MPC. The models do predict power deposition within the MPC, and there are differences between the grounded and ungrounded casks, but the power deposited is sufficient only to cause a small average temperature increase in the MPC. Tables 7-1 and 7-2 list the average and peak temperature increases calculated in various regions of the model. Results from the 2-d cask model predict higher temperatures within the MPC, although still not high enough to cause damage or a breach of the container. The fact that the 2-d model predicted higher temperatures within the MPC may be due to the azimuthal scaling that was applied or possibly caused by model differences. A specific source for this difference has not been identified. Even the highest predicted temperatures from the various models did not exceed the damage threshold, except in the steel lid at the lightning strike location. At that location it is fairly certain that melting and vaporization of a small volume of the metal lid will occur.

Table 7-1. Average temperature increase in grounded and ungrounded cask components (initial temperatures vary with region)

Cask region	Average temperature increase (°C)	
	Grounded	Ungrounded
MPC contents	2	2
Overpack concrete	0.2	0.3

Table 7-2. Peak temperature increase in grounded and ungrounded cask components (initial temperatures vary with region)

Cask region	Peak temperature increase (°C)	
	Grounded	Ungrounded
MPC contents	18	11
Overpack concrete	5.9	25.3

The material properties and initial temperatures in each model region were evaluated to determine the minimum power deposition density required to cause a detectable temperature change and for damage to begin to occur. Table 7-3 summarizes the total power deposition required over a 500 μs pulse length to reach these two thresholds.

Table 7-3. Required power deposition for a detectable temperature change and for onset of damage in each of the cask regions

Cask region	Required power density for 500 μs (W/m^3)	
	Detectable temperature change	Damage threshold
MPC contents	1.0×10^8	2.7×10^{11}
MPC shell	5.0×10^9	1.6×10^{13}
Overpack concrete	1.0×10^9	1.5×10^{11}
Overpack shell	5.0×10^9	1.6×10^{13}

Power Deposition in Concrete Radiological Shielding

When comparing the power deposition results from grounded and ungrounded cask simulations, we find that substantially more power is deposited in the concrete radiological shielding when the cask is ungrounded compared to when grounded. The ratio of power deposition in grounded and ungrounded casks varies during the excitation pulse, from about a factor of 2 to a factor of 13 more power deposited in the concrete in an ungrounded cask. As an overall average, about 3 times as much power is deposited in the concrete shielding in an ungrounded cask as compared to a grounded cask.

In spite of the differences in power deposition between grounded and ungrounded casks, it was found that both 3-d calculations and appropriately scaled 2-d calculations both predict small peak and average temperature rises in the concrete for both grounded and ungrounded casks. In 2-d calculations, with an initial temperature of 66°C, the average temperature rise was found to be 0.2°C in the grounded cask and 0.3°C in the ungrounded cask. The peak temperature rise was found to be 5.9°C in the grounded cask and 25.3°C in the ungrounded cask. Some earlier cases had shown higher power deposition results but were found to be related to the model or excitation profile. The 2-d results for an ungrounded cask still indicate the possibility of local temperature excursion sufficient for damage. To further quantify the damage potential, a 3-d model was constructed to better represent current penetration through the cask walls. One concern with the 2-d model is that an insufficient number of elements are present to represent the steel can wall thickness. The lid of the 2-d model is represented by ten elements, but the side walls are represented by only two elements. To quantify the degree of current penetration through the lid and walls of the overpack, a specific 3-d model was used. For equivalent conditions to those in the 2-d model, this 3-d model predicted less current penetration through the steel canister walls than was predicted by the 2-d

model, resulting in a lower temperature rise. Except for a small local region, just below the lightning strike location, the 3-d cylinder model showed imperceptible temperature changes. This confirms that the 2-d results are conservative and that the actual power deposition will almost certainly be less than that predicted.

The presence of air vents through the overpack will increase current flow on the inner surface of the overpack and will be expected to increase the power deposited in the overpack shell and concrete shielding. The air vents were not represented in any of the models, thus a reasonable estimate of the importance of the vents is not available. This feature would be the most useful addition to a more complex model, if it were developed.

Power Deposition in the Steel Cask Lid

Obviously, the largest power deposition density occurs at the lightning strike location, which is on the lid in these simulations. There was concern that power deposition would be sufficient to cause localized melting that would breach the cask. Both 2-d and 3-d models confirmed that the highest power density is deposited at the strike location. Because of the wide variation of spatial resolution of the various models, the different simulations predicted varying peak temperatures on the lid. Average temperatures were in close agreement because the heat deposition is averaged over such a large volume that there is little average temperature rise in any model. The 3-d cylinder model is fundamentally a different configuration from the storage cask and therefore is not expected to agree with the results from the two other cask models. Its higher spatial resolution, however, may make the results from this model the most accurate. With the larger cell sizes in the 3-d cask model, the peak temperature is actually averaged over a large volume, thus reducing the predicted peak temperature. Without accounting for latent heat, the 3-d cylinder model predicts approximately 129 cm^3 of melted material (~5 cm cube). Including the latent heat required to first melt and then vaporize the metal, the volume of vaporized metal drops to 53 cm^3 (~3.8 cm cube). Because of the small overall size of this model, and the specific boundary conditions applied to it, this model is expected to predict higher temperatures than will be encountered in an actual lightning strike. Nonetheless, the temperatures predicted by this model are significant enough to raise concern and warrant more careful analysis of the local heating process.

Table 4. Average and Peak predicted temperature increases in the cask lid from various models.

	Peak temperature increase (°C)	
Cask region	Average	Peak
2-d cask model	12	1767
3-d cask model	~0	62
3-d cylinder	3	>10,000

Voltage on the Outer Shell of the Overpack

One major difference between grounded and ungrounded casks is the voltage profile on the outer shell of the overpack. With the cask grounded to a rebar grid embedded in the concrete pad, the cask voltage at the interface with the pad will be close to zero. In simulations, the voltage is precisely zero at the boundary condition that is applied below the simulated soil layer under the concrete pad. With a ground connection through the soil and concrete to the cask, only a very small voltage on the cask is present at the concrete interface. However, with the cask ungrounded, the voltage at the concrete interface is several MV, causing concern for personnel and equipment. In Figure 7-1 normalized voltage profiles along the vertical outside surface of the overpack are shown for grounded and ungrounded casks. In this figure, the voltages are normalized to the peak voltage for each profile. In the various simulations peak voltages

were seen to range from about 3 – 6 MV, depending on the excitation profile. One difference between the simulation results, shown in Figure 1, and an actual lightning strike will be the rate at which the voltage goes to zero near the concrete pad. Since the simulation forced the voltage to go to zero only a short distance below the concrete pad, the simulations show a steeper voltage gradient than would be the case in a real lightning strike. In a real lightning strike, voltages will be higher in the concrete pad and soil for both grounded and ungrounded cask because the currents cannot be spread and dissipated as quickly and efficiently as in an idealized case.
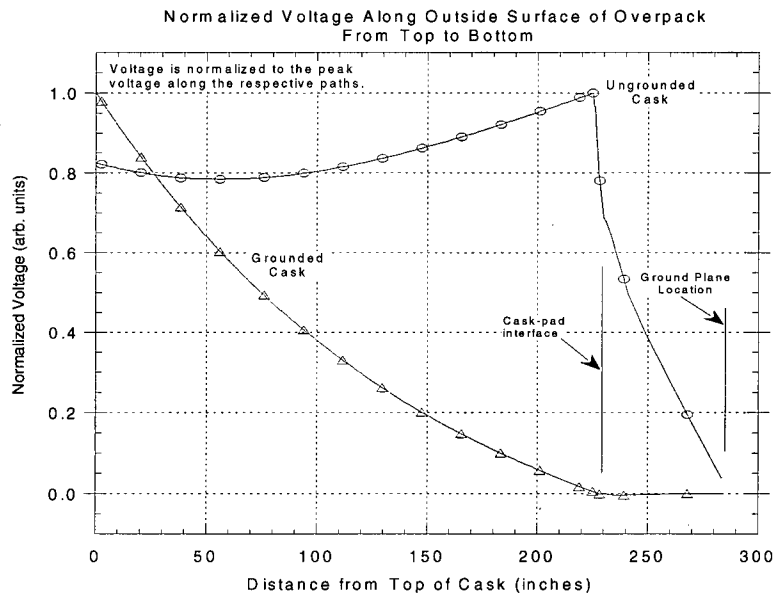
Figure 7-1. Normalized voltage along the outside surface of the overpack.

Results from 3-d Cylinder Model

The power deposition in the metal lid is easily sufficient to vaporize some of the lid material and raise the lid temperature locally to very high temperatures. However, the predicted cement temperature is insufficient to raise its temperature to the point where even local vaporization of free water in the cement would occur. As a result, the temperature and pressure in the radiological shielding will not change appreciably during the lightning strike so long as the parameters are reasonably close to those used in these simulations. Another key feature that is essential to limiting the temperature rise in the concrete is the elimination of any direct current path into the concrete from the outer surface.

Temperature

The peak temperature reached in either the metal container or concrete fill material will be only a function of local conditions since the heat deposition occurs over a time period so short that no heat conduction, water migrations, capillary action, or other process has time to occur. For regions on or near the surface, the peak temperature is likely to occur close to the lightning strike location. For regions far removed from the surface or from the lightning strike location, the location of the peak temperature will be harder to guess, and will depend on the specific current paths in the region. In the simple models considered here, the absolute peak temperature occurs at, or just beneath the location of the lightning strike. Other regions of high temperature occur at the edges of the lid where power loss is accentuated by the sharpness of the corner and the flow of current around and through the edge region. Since, we are interested in simply determining if a melting, rupturing, explosive heating condition can possibly exist, we first looked only locally in the region of the simulated lightning strike.

Discussion of Assumptions and Simplifications

Strike Location
Only a single lightning strike location was evaluated for each model, leaving the possibility that other strike locations may result in higher temperatures, particularly locally.

Lightning Current Pulse Shape
Pulse shape is seen to have a significant effect on power deposition, due to the varying frequency content. Only a couple of lightning pulse shapes have been simulated and the quantitative effects of other pulse shapes are unknown. Beyond that, real lightning pulses can and do have widely varying and complex pulse shapes, the effects of which have not been modeled. Longer duration lightning pulses penetrate the steel shell more deeply and thus increase the predicted power deposition in the cask interior.

Model Approximations
The largest contributors to uncertainty from the model designs are expected to be from the fact that the air vents allow a clear and direct path through the overpack to the MPC outer shell, but these are not well represented in any of the models that have been evaluated. In all of the models, improved accuracy would also be obtained if metal wall thicknesses were represented by additional elements.

Material Properties
Representative material properties were chosen for each region of the model but no attempt to quantify the effects of the range of property values on the results was made. In particular, concrete properties vary widely and are dependant on mixing and curing processes as well as the constituent materials. The properties of the actual concrete used in the Holtec casks are unknown.

7.2 Overall Conclusions

The overall conclusion relative to the potential hazards to the Holtec Hi-Storm 100 Dry Storage Cask is that there is no hazard to the MPC or MPC contents from energy deposition during a lightning strike. Both the peak and average temperature remain below the threshold where physical damage or overpressure could result. It is further found that concrete in the various regions of radiological shielding is not heated sufficiently for damage to occur. Predicted peak temperatures remain below the level where vaporization of water would occur, which could have led to an overpressure. It is concluded that the carbon steel lid will suffer a substantial amount of melting and material vaporization in a very localized region at the site of the lightning strike.

The size of the damaged region on the lid is predicted to be on the order of a cubical volume 4–5 cm on a side (50–100 cm^3), although there are processes that will occur at these temperatures that will reduce temperature and mitigate the damage by absorbing a significant amount of energy. Not all of these processes have been accurately taken into account in these calculations so that the predicted damage is an upper bound.

8. REFERENCES

"Lightning Test Waveforms and Techniques for Aerospace Vehicles and Hardware," Report of Society of Automotive Engineers (SAE) Committee AE4-L on Electromagnetic Compatibility, June 20, 1978.

"Lightning Qualification Test Techniques for Aerospace Vehicles and Hardware," Military Standard MIL-STD-1757, June 17, 1980.

Capt. Randy J. Jost, Capt. Mary P. Hebert, and Capt. James L. Hebert, "An Assessment of Analytical Methods and Lightning Simulation Test Techniques used in Lighting Qualification and Surveillance Testing," International Aerospace and Ground Conference and Lighting and Static Electricity, 105–112 (1988).

J. Anderson Plumer, "A New Standard for Lightning Qualification Testing of Aircraft: Technical Overview, Definitions and Basic Waveforms," Lightning Technologies, Inc, pp. 7-1 through 7-9.

Mike Whitaker, "Activation of the Navy's Indirect Effects Lightning Simulation Laboratory," Electromagnetic Pulse Section, Naval Air Test Center, pp. 32-1 through 32-9.

Andrew S. Podgorski, "Three-Dimensional Time Domain Model of Lightning Including Corona Effects," Electromagnetic Protection Group, Institute for Information Technology, National Research Council of Canada, Ottawa, Canada K1A OR6, pp. 75-1 through 75-7.

Marcos Andre da Fronta Mattos and Christos Christopoulos, "A Nonlinear Transmission Line Model of the Lightning Return Stroke," IEEE Trans. of Electromagnetic Compatibility, **Vol. 30**, No. 3, 401–406 (1988).

Don W. Clifford, Keith E. Crouch, and Edward H. Schulte, "Lightning Simulation and Testing," IEEE Trans. on Electromagnetic Compatibility, **Vol. EMC-24**, No. 2, 209–224 (1982).

Igor Remec, and F. B. K. Kam, "H. B. Robinson-2 Pressure Vessel Benchmark," Oak Ridge National Laboratory, prepared for the U.S. Nuclear Regulatory Commission, ORNL/TM-13204 and NUREG/CR-6453 (1997).

Handbook of Tables for Applied Engineering Science, 2nd ed., edited by Ray E. Bolz, and George L. Tuve, Chemical Rubber, Cleveland, Ohio (1973).

American Institute of Physics Handbook, 3rd ed., Coordinating Editor, Dwight E. Gray, McGraw-Hill Book Company (1972).

Handbook of Chemistry and Physics, 56th ed., edited by Robert C. Weast, CRC Press, Cleveland, Ohio (1975–76).

C. B. Oland and D. J. Naus, *Summary of Materials Contained in the Structural Materials Information Center*, ORNL/NRC/LTR-94/22 (November 1994).

P. Schimmelwitz and J. Hundt, "A Note on the Moisture Condition of Concrete," published in *Concrete for Nuclear Reactors*, Vol. II, pp. 873–882.

Edwin J. Callan, "Concrete for Radiation Shielding," reprinted from the *ACI Journal, Proceedings V,* **50,** 17–44 (1953).

K. W. Childs, *HEATING 7.2 User's Manual,* ORNL/TM-12262 (February 1993).

APPENDIX A

APPENDIX A.

A.1 General EMAS Code Capabilities Description

The EMAS computer code (ElectroMagnetic Analysis System) is a large computer program that analyzes electromagnetic fields using the finite element method. The code is capable of modeling all aspects of field behavior described by Maxwell's equations. Because of its broad generality, EMAS analyses can be used for a wide range of systems and devices, including magnets, generators, antennas, waveguides, lumped circuit elements (R, L, C), microwave devices and others. In addition, a wide range of excitation types can be applied to the models, including point excitations representing total charges or currents, surface excitations representing field or current values, volume excitations representing charge or current density, polarizations, permanent magnets, or coil windings. Time profiles of excitations can be constructed from known functions, tabular input, or by pointwise specifications. A particular model can include one or many dependant or independent sources. Material properties can be scalar or complex, linear or nonlinear, isotropic or anisotropic, symmetric or unsymmetric. Material properties can make use of a set of predefined material properties or can be specially constructed. Independent or dependant boundary conditions can be imposed to represent boundaries, free space or symmetry surfaces. Objects can be modeled in any of several coordinate systems, including rectangular, cylindrical, spherical or user-defined, in one- two- or three-dimensions.

A.2 Theoretical Basis for the EMAS Computer Code

In this section is reproduced (with permission), the mathematical theory portion of one of the EMAS user manuals for reference. Numerous published references for the computer code and solution sequences are included at the end of this section.

APPENDIX A.

A.1 General EMAS Code Capabilities Description

The EMAS computer code (ElectroMagnetic Analysis System) is a large computer program that analyzes electromagnetic fields using the finite element method. The code is capable of modeling all aspects of field behavior described by Maxwell's equations. Because of its broad generality, EMAS analyses can be used for a wide range of systems and devices, including magnets, generators, antennas, waveguides, lumped circuit elements (R, L, C), microwave devices and others. In addition, a wide range of excitation types can be applied to the models, including point excitations representing total charges or currents, surface excitations representing field or current values, volume excitations representing charge or current density, polarizations, permanent magnets, or coil windings. Time profiles of excitations can be constructed from known functions, tabular input, or by pointwise specifications. A particular model can include one or many dependant or independent sources. Material properties can be scalar or complex, linear or nonlinear, isotropic or anisotropic, symmetric or unsymmetric. Material properties can make use of a set of predefined material properties or can be specially constructed. Independent or dependant boundary conditions can be imposed to represent boundaries, free space or symmetry surfaces. Objects can be modeled in any of several coordinate systems, including rectangular, cylindrical, spherical or user-defined, in one- two- or three-dimensions.

A.2 Theoretical Basis for the EMAS Computer Code

In this section is reproduced (with permission), the mathematical theory portion of one of the EMAS user manuals for reference. Numerous published references for the computer code and solution sequences are included at the end of this section.

1   THEORY

1.1   INTRODUCTION

The purpose of this chapter is to relate the user's knowledge of electromagnetic field theory to the task that EMAS performs. This chapter begins by reviewing the principles of electromagnetism in order to state assumptions explicitly and to establish notation. Potentials are discussed in detail since they are unfamiliar to most users. Finally, the theory is cast in a form for computer analysis by introducing finite element approximations. In reading this chapter, the user will make a logical, step-by-step transition from the familiar world of field analysis to the new and less familiar world of finite element field analysis.

Chapters such as this one are usually not included in user's manuals because the theoretical underpinnings of most commercial engineering analysis programs are widely known and accepted. This is certainly not the case in E&M field analysis. While finite element analysis is standard fare in mechanical engineering and can be found in most undergraduate curricula, finite element methods are unknown to most electrical engineers and physicists. Moreover, the particular formulation used in EMAS is in some respects original and unique. It therefore deserves detailed exposition.

The formulation described here takes the traditional, analytical treatment of electromagnetics and casts it in a much simpler, more unified form for finite element analysis. Maxwell's equations are converted into a single matrix equation

$$[M]\{\ddot{u}\} + [B]\{\dot{u}\} + [K]\{u\} = \{P\}. \tag{1.1.1}$$

The equation has the same form as that for either a system of passive circuit elements or damped harmonic oscillators. The four degrees of freedom (DOFs) per grid point $\{u\}$ represent three components of the conventional vector potential $\vec{A}$ plus an unconventional scalar potential ψ. The matrix $[M]$ is related to the material dielectric constant, while the matrices $[B]$ and $[K]$ are related to conductivity and permeability. Material properties may be fully anisotropic, and in the case of magnetic materials, nonlinear. This equation is fully equivalent to Maxwell's equations in their complete and general form. As a result, solutions for a wide range of applications—electrostatics, current flow, magnetostatics, eddy currents, resonant cavities, waveguides, etc.—can be obtained from this single governing equation.

The discussion in Chapter 1 assumes that the reader is familiar with certain technical concepts. Though the formulation proceeds from first principles, a familiarity with the principles of electromagnetics and the use of the vector potential is desirable. Knowledge of vector calculus (divergence, curl, gradient, surface, and line integrals, etc.) and of variational calculus (virtual work) is assumed. Familiarity with linear algebra and matrix notation is also assumed. The reader unfamiliar with these subjects is directed to the bibliography at the end of this Section for suggested readings.

The choice of units in EMAS is left entirely to the user. For convenience, the formulation is carried out in the rationalized MKS system. The notation is somewhat different in other systems. The user is referred to Section 2.2 (of Chapter 2) or the basic texts listed in the bibliography (of this chapter) for a thorough discussion.

The logical flow of the formulation is shown in Figure 1.1.1. First, the electric and magnetic fields are defined in terms of underlying electromagnetic forces. Then their sources and dynamic interactions are reviewed in a Section on the principles of electromagnetics. Once material interactions are taken into account, Maxwell's equations are stated in their general form. Vector and scalar potentials are then introduced to simplify the analysis. A variational principle is derived that reproduces Maxwell's equations in potential form. Then, the integral expression for virtual work is subdivided into small, relatively simple finite element volumes. Generalized forces associated with the unknown degrees of freedom are set to zero, thus imposing dynamic equilibrium. The resulting matrix equation is given in Eq. (1.1.1). Data recovery from solutions is briefly discussed, and modifications for nonlinear analysis are described. Finally, an **exact analogy** between electromagnetics and structural mechanics is described.
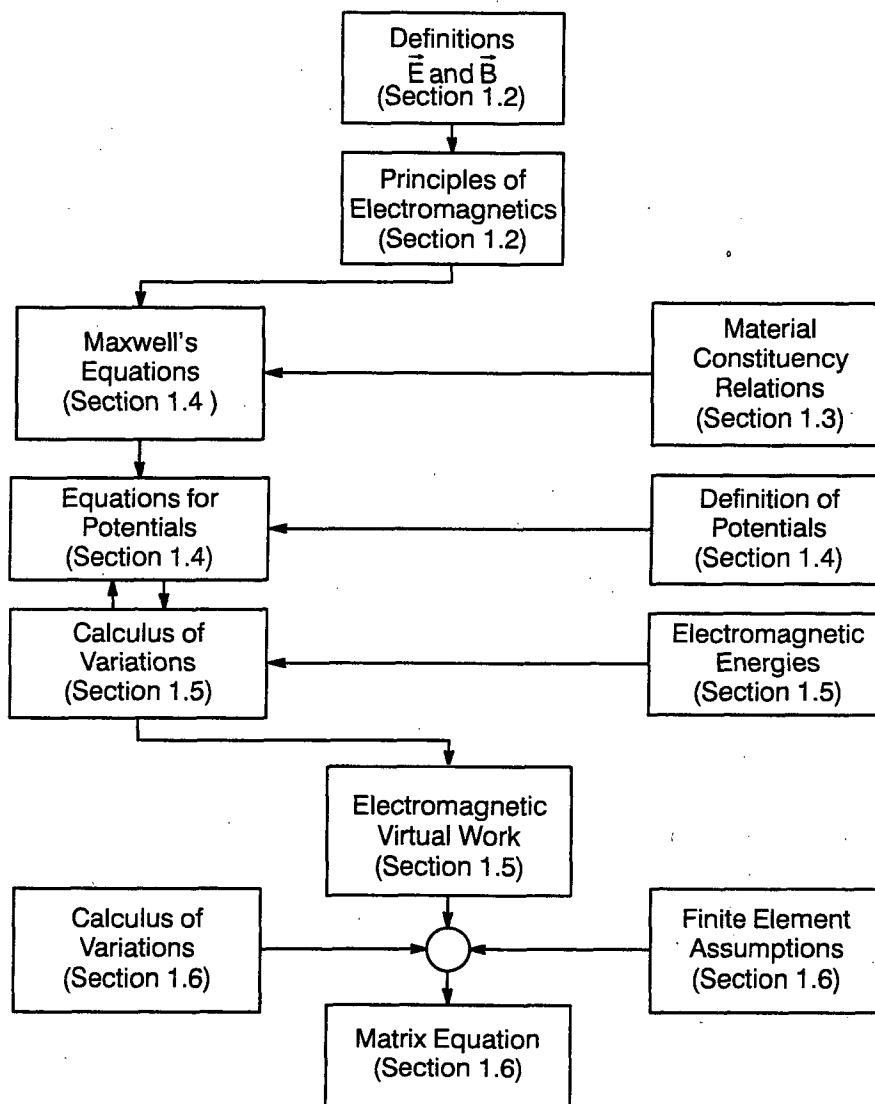
Figure 1.1.1: Formulation of electromagnetics for finite element analysis.

1.2 PRINCIPLES OF ELECTROMAGNETICS

Electromagnetics is the branch of science that deals with the electric and magnetic forces between charged objects (Figure 1.2.1). Electric and magnetic fields are defined by these forces. Rather than deal directly with the motion of charges, the sources and interactions of the fields themselves are emphasized. Thus, the fields take on a certain physical reality. The actual motion of charge, electrical current, is treated as a recovery quantity. This Section discusses the definition of electromagnetic forces and fields, and their dynamic interactions in vacuum.
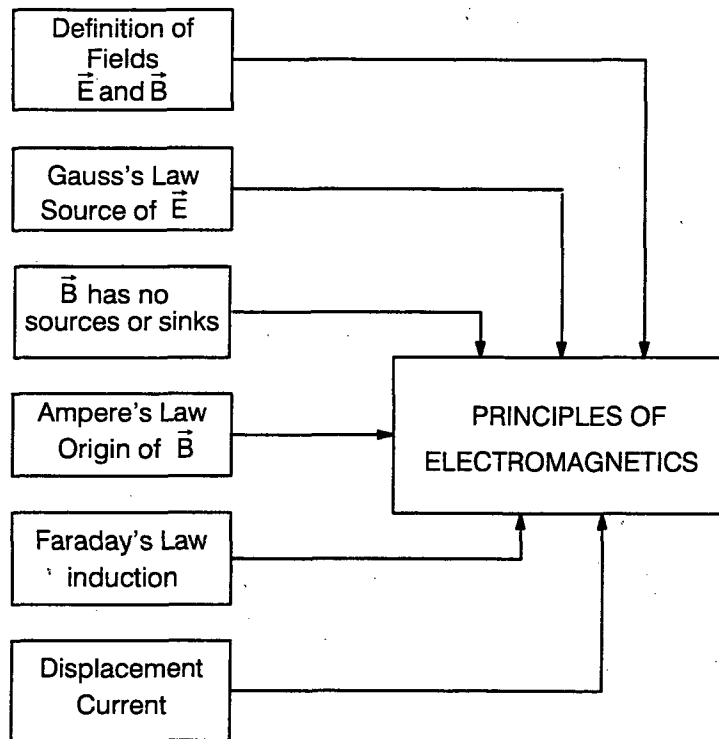
Figure 1.2.1: Principles of electromagnetics.

ELECTRIC FIELDS

Electric fields are defined by fundamental electrical forces between stationary charges. Consider two charges q and q' separated by a distance $r = |\vec{r}|$. The force between these charges is found experimentally to be

$$\vec{F}_e = \frac{qq'\vec{r}}{4\pi\epsilon_o r^3}$$

(1.2.1)

Here, ϵ_o is a dimensioned constant, the dielectric permittivity of vacuum. The force can be either repulsive (charges with the same sign) or attractive (opposite sign). The electric field strength, or simply electric field $\vec{E}$, at location $\vec{r}$ is defined as the electrical force per unit test charge q' in the limit as q' tends to zero

$$\vec{E} = \lim_{q' \to o} \frac{\vec{F}_e}{q'}$$

(1.2.2)

Thus, the electric field from a single point charge is, from Eq. (1.2.1)

$$\vec{E} = \frac{q\vec{r}}{4\pi\epsilon_0 r^3} \tag{1.2.3}$$

The total field from an assembly of charges is simply the vector sum of fields from the individual charges.

MAGNETIC FIELDS

Magnetic fields are defined by magnetic forces acting on moving charges. If a charge is moving with velocity $\vec{v}$, in a magnetic field $\vec{B}$, then it experiences a force F_b,

$$\vec{F}_b = q\vec{v} \times \vec{B} \tag{1.2.4}$$

This relationship is taken as the definition of the magnetic field. Magnetic forces may always be distinguished from electrical forces by their velocity dependence.

LORENTZ FORCE

The total electromagnetic force, the Lorentz force $\vec{L}$ (Figure 1.2.2), on a moving test charge q' is just the sum of F_e and F_b

$$\vec{L} = q(\vec{E} + \vec{v} \times \vec{B}) \tag{1.2.5}$$
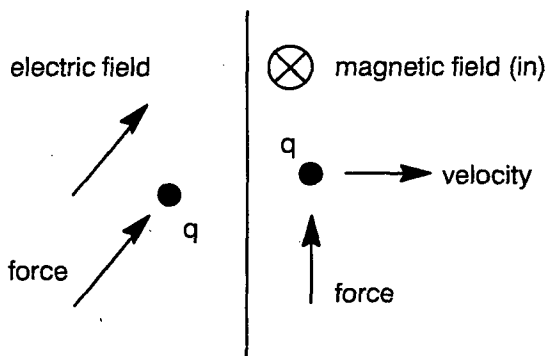
Figure 1.2.2: The Lorentz force.

The force acting on a charge may always be decomposed into forces from electric and magnetic fields. In electromagnetics, the actual motion of individual charges under the influence of such forces is of secondary importance. Instead dynamic behavior is described by the fields.

GAUSS'S LAW

Gauss's law (Figure 1.2.3) states that the sources and sinks of the electric field are electrical charges. The lines of $\vec{E}$ originate on positive charge and terminate on negative charge. To obtain a more quantitative relationship, consider some arbitrary volume V enclosed by a surface S. The flux of $\vec{E}$ flowing out through S is proportional to the net electrical charge inside V

$$\epsilon_o \int_s ds\, \vec{E} \cdot \hat{n} = \int_v dv\, \rho \qquad (1.2.6)$$

where ρ is the charge density (net charge per unit volume). In the limit as V tends to zero volume, Eq. (1.2.6) reduces to the vector calculus expression

$$\epsilon_o \nabla \cdot \vec{E} = \rho \qquad (1.2.7)$$

Thus, Gauss's law describes the origins of $\vec{E}$ in terms of its sources and sinks. Lines of $\vec{E}$ do not close on themselves.
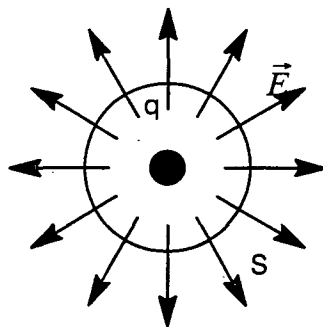
Figure 1.2.3: Gauss's law relates the flux of E to its sources, electric charge.

Unlike $\vec{E}$, the magnetic field $\vec{B}$ has neither sources nor sinks. The flux of $\vec{B}$ out of any closed volume is always zero, or

$$\nabla \cdot \vec{B} = 0 \qquad (1.2.8)$$

As a consequence, the field lines of $\vec{B}$ do not originate or terminate on any object.

AMPERE'S LAW

Ampere's law describes the origins of $\vec{B}$ in terms of electrical currents (Figure 1.2.4). Consider a current $\vec{I}$ flowing out of the page. The magnetic field produced by the current circulates around the wire in the sense dictated by the right-hand rule. A quantitative relationship is obtained by considering an arbitrary surface S bounded by a closed loop L.
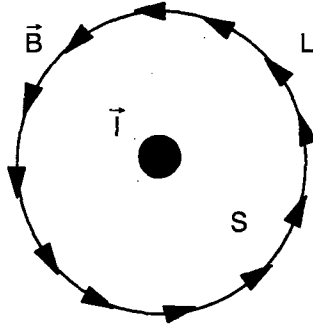
Figure 1.2.4: Ampere's law relates the circulation of $\vec{B}$ to its source, electrical current.

Ampere's law states that the circulation of $\vec{B}$ around L is proportional to the total current passing through the loop

$$v_o \oint_L d\vec{l} \cdot \vec{B} = \int_s \vec{J} \cdot \hat{ds} \qquad (1.2.9)$$

The dimensioned constant v_o is called the magnetic reluctivity (of vacuum). The user may be more familiar with a related quantity, the magnetic permeability, $\mu_o = v_o^{-1}$. The reluctivity is used throughout in order to simplify notation. The user interface described in Chapter 2 uses the permeability because this parameter is more readily available.

In the limit as S shrinks to a single point with zero area

$$v_o \nabla \times \vec{B} = \vec{J} \qquad (1.2.10)$$

Thus currents define the origins of $\vec{B}$ in terms of its circulation (or curl) around a closed loop, rather than its sources and sinks (divergence).

FARADAY'S LAW

Faraday's law of induction (Figure 1.2.5) states that electric fields are induced by time-varying magnetic fields $\vec{B}$. For a quantitative relationship, consider again an arbitrary surface S enclosed by a loop L. Faraday's law states that the circulation of $\vec{E}$ around L is equal to (minus) the rate of change of the total flux of $\vec{B}$ through S

$$\oint_L d\vec{l} \cdot \vec{E} = -\frac{d}{dt} \int_s ds \left(\vec{B} \cdot \hat{n} \right)$$

(1.2.11)
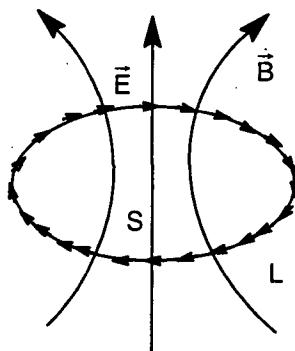
Figure 1.2.5: Faraday's law states that time-varying magnetic fields produce electric fields.

As S shrinks to zero area,

$$\nabla \times \vec{E} = -\dot{\vec{B}}$$

(1.2.12)

This principle may seem at first to be somewhat odd. Here are two fields (which, after all, are simply shorthand notation for the forces between currents and charges) that interact even in vacuum, independent of their origins. Nevertheless, induction is a common phenomenon and governs the operation of many practical devices, including transformers and induction motors.

DISPLACEMENT CURRENT

The introduction of the concept of displacement current by James Clerk Maxwell in 1865 completed the modern formulation of electromagnetics. At that time, he noted that the principles of electromagnetics as stated thus far were not consistent. From taking the divergence of Eq. (1.2.10), it is clear that the currents acting as sources of $\vec{B}$ are divergence free. But there are many real, physical situations in which conduction current is not divergence free. For example, consider the case shown in Figure 1.2.6, a parallel plate capacitor with constant current I flowing into one plate and out the other.
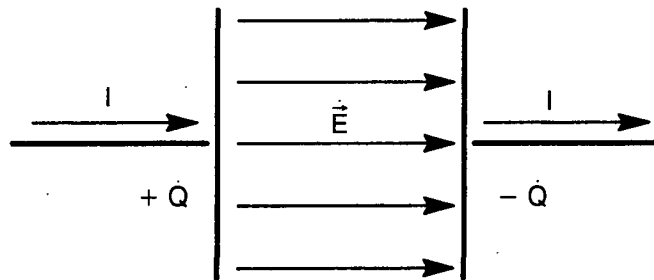
Figure 1.2.6: The displacement current is demonstrated in a parallel plate capacitor.

The field between the plates and the charge on the plates all increase at a constant rate. The flow of current into the plates is not zero, so the divergence of the conduction current cannot be zero. Maxwell postulated that the current density $\vec{J}$ that produces the circulation of $\vec{B}$ in Eq. (1.2.10) has two components: the conduction current due to the actual flow of charge, $\vec{J}_{cond}$ and a displacement current $\vec{J}_{disp}$ due to time-varying electric fields

$$\vec{J} = \vec{J}_{cond} + \vec{J}_{disp} \qquad (1.2.13)$$

where

$$\vec{J}_{disp} = \epsilon_0 \dot{\vec{E}} \qquad (1.2.14)$$

It is the sum of these two components that is divergence free. With this single additional assumption Maxwell was able to show that the principles of electromagnetics are consistent; in fact, he correctly predicted the propagation of light as waves. In honor of this achievement, the governing equations of electromagnetics are known as Maxwell's equations.

1.3   MATERIAL PROPERTIES

1.3.1   Anisotropic and Isotropic Properties

The response of fixed charge in materials to electromagnetic fields can, in general, be quite complicated. If, however, average behavior is viewed on a macroscopic scale, material response can be greatly simplified. A fairly general model (Figure 1.3.1) of material behavior has been incorporated into EMAS. Material properties are specified by three quantities: permittivity, conductivity, and permeability. All three quantities may be anisotropic (dependent on direction) or isotropic (independent of direction). The permeability may also be a nonlinear function of $\vec{B}$. A wide range of material properties may be described with this model. The assumptions that lead to the EMAS material model are described in this Section.

It is convenient to distinguish between various types of charges and currents. Electrical charge is divided into two classes: (1) mobile electrical charge density ρ_{free}, which is free to move through the material, and (2) immobile charge density ρ_{atomic} not free to move in a macroscopic sense (typically bound in orbitals around atomic nuclei). The total charge density is simply the sum of these two classes

$$\rho = \rho_{free} + \rho_{atomic} \qquad (1.3.1)$$

```
 ┌─────────────┐     ┌──────────────┐
 │  Ohm's Law  │─────│    [σ]       │
 │             │     │   linear     │
 └─────────────┘     │ anisotropic  │
                     └──────────────┘
 ┌──────────────────┐              ┌──────────┐
 │ Dielectric       │              │ Material │
 │ Response         │──────────────│  Model   │
 │   [ε]            │              └──────────┘
 │  linear          │
 │  anisotropic     │
 └──────────────────┘
 ┌──────────────────┐
 │ Magnetic         │
 │ Response         │
 │   [ν]            │
 │  nonlinear       │
 │  anisotropic     │
 └──────────────────┘
```
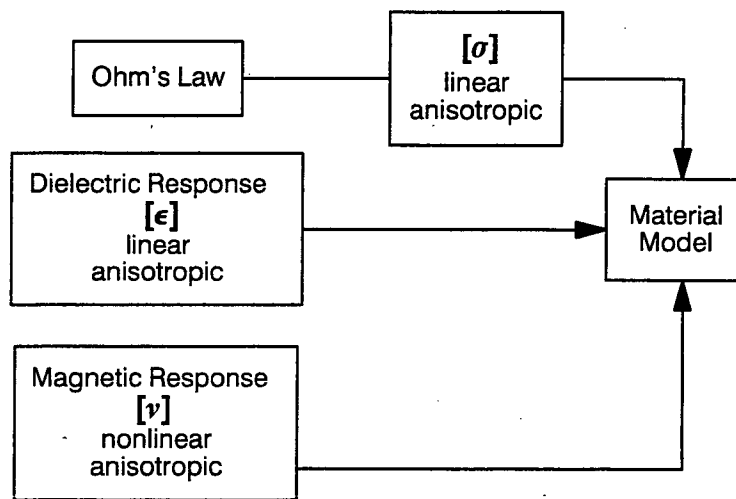
Figure 1.3.1: The material model.

The conduction and displacement currents have already been defined. A third class of currents must be added when materials are taken into account: the localized current $\vec{J}_{atomic}$ due to circulation (but not macroscopic transport) of charge around atomic nuclei. The total current density is a sum of three components

$$\vec{J} = \vec{J}_{cond} + \vec{J}_{atomic} + \vec{J}_{disp} \qquad (1.3.2)$$

Bound charges and currents do produce real effects that are taken into account in the form of atomic dipoles (second-order charge distributions). They do not produce (first-order) macroscopic charge or current. The distinction between bound and mobile charges simplifies the traditional treatment of material properties.

It is assumed that macroscopic charge is conserved. Charge flowing into a volume must be accounted for by an increase in charge density within. This continuity condition can be written as

$$-\nabla \cdot \vec{J}_{cond} = \dot{\rho}_{free} \qquad (1.3.3)$$

Atomic charges play no role in the continuity condition because they produce no macroscopic current. The displacement current also has no role in continuity, since it does not actually represent the flow of charge. The time integral of Eq. (1.3.3) is also useful

$$\rho_{free}(t) = \rho_o - \int_{t_o}^{t} dt' \, \nabla \cdot \vec{J}_{cond}(t') \qquad (1.3.4)$$

The charge density at some time t is the value at some initial time ρ_o plus the total amount that has flowed into the volume since initial time (the integral). Charge continuity, which accounts for the motion of macroscopic charge, plays a fundamental role in the formulation of electromagnetics.

Ohm's law is a familiar macroscopic description of the motion of free charge through materials (Figure 1.3.2). Charges (typically mobile electrons) are accelerated when an electric field is applied. From time to time, charges collide with obstructions (typically dislocations, impurities, lattice vibrations), causing them to lose
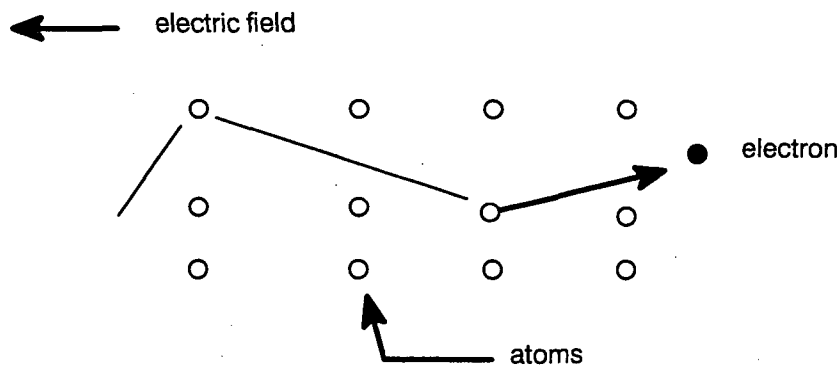
Figure 1.3.2: Ohm's law.

momentum and energy (in the form of heat). As these charges rattle through the material they acquire a net average drift velocity that is proportional to the applied field. As a result, the total conduction current density is proportional to the electric field

$$\vec{J}_{cond} = [\sigma]\vec{E} \qquad (1.3.5)$$

The constant of proportionality, the conductivity $[\sigma]$, is a 3x3 symmetric tensor (matrix) to account for anisotropy. If it has only diagonal terms that are the same in all three directions, then conductivity is isotropic and may be represented by one scalar number. If $\vec{E}$ is induced by $\vec{B}$ (Faraday's law), then the resulting currents are called eddy currents.

The reaction of fixed, microscopic charges (mainly electrons bound within atomic orbitals) to electric fields is called the dielectric response (Figure 1.3.3). Applied fields exert forces on the electrons and nuclei, causing a slight separation of charge.

electric field

dipoles

nuclei

electron orbits
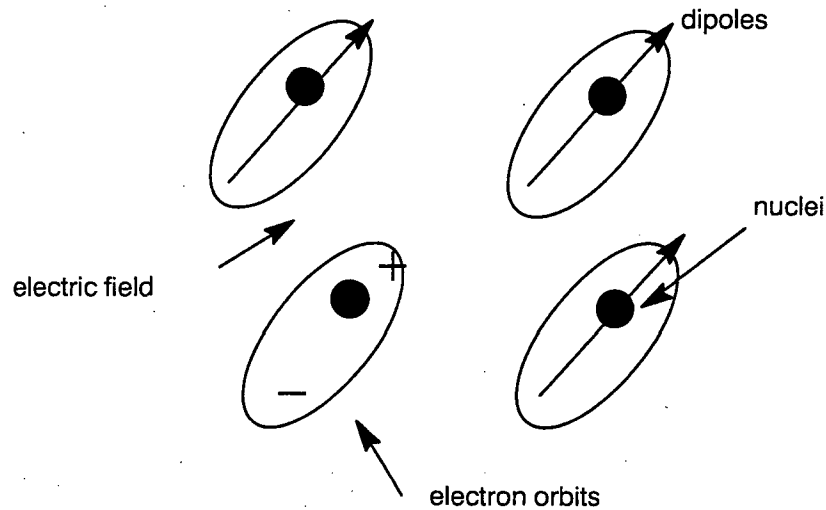
Figure 1.3.3: Dielectric response.

On a macroscopic scale, this separation creates an electric dipole. The direction and strength (charge x separation) of this dipole are given by the atomic dipole moment. The average dipole moment per unit volume $\vec{P}$, the polarization, is proportional to the applied field in most practical cases

$$\vec{P} = [\chi_e]\vec{E} + \vec{P}_o \qquad (1.3.6)$$

where the constant of proportionality, $[\chi_e]$, is the dielectric susceptibility tensor and $\vec{P}_o$ is the remanent polarization. In some cases, for example at the boundary of polarized media, the divergence of the polarization produces macroscopic atomic charge

$$\rho_{atomic} = -\nabla \cdot \vec{P} \qquad (1.3.7)$$

But this charge is considered immobile when accounting for charge continuity. For convenience a second electric vector, the displacement $\vec{D}$, is defined as

$$\vec{D} = \epsilon_o\vec{E} + \vec{P} \qquad (1.3.8)$$

By taking the divergence of Eq. (1.3.8), and combining that result with Eqs. (1.2.7), (1.3.1) and (1.3.7), it is clear that the sources of $\vec{D}$ are restricted to free charges only

$$\nabla \cdot \vec{D} = \rho_{free} \qquad (1.3.9)$$

By combining the time derivative of Eq. (1.3.9) with Eq. (1.3.3), the displacement current and $\vec{D}$ have the same sources; therefore displacement current is given quite generally as

$$\vec{J}_{disp} = \dot{\vec{D}} \qquad (1.3.10)$$

In most situations, Eq. (1.3.6) applies, so by combining the results of Eqs. (1.3.6) and (1.3.8), it can be shown that $\vec{D}$ is simply proportional to $\vec{E}$

$$\vec{D} = [\epsilon]\vec{E} + \vec{P}_o \qquad (1.3.11)$$

where the constant of proportionality, the dielectric permittivity tensor $[\epsilon]$ (or more simply, the dielectric constant), is independent of $\vec{E}$. $[\epsilon]$ is a generalization accounting for possible anisotropy of the scalar quantity ϵ.

In most situations, the macroscopic magnetic response of bound, microscopic currents to applied magnetic fields is much more complicated than the dielectric response. Various responses are described in the literature, including paramagnetism, diamagnetism, ferromagnetism (Figure 1.3.4), antiferromagnetism, ferromagnetism, and so on. Many of these involve not only induced atomic magnetic dipoles, but also atoms with large, permanent atomic dipoles. The behavior of permanent dipoles can also be correlated over large distances, leading to ferromagnetic domains.
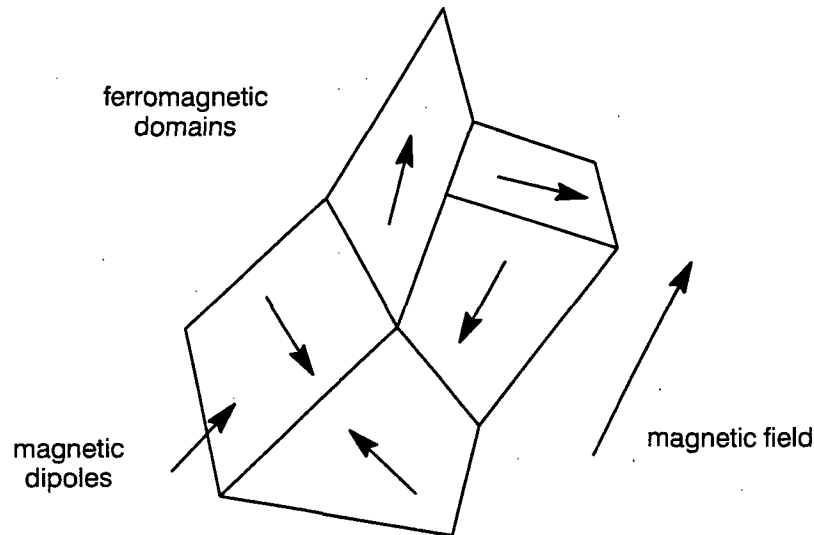
Figure 1.3.4: Magnetic response.

In the macroscopic view (on a scale larger than domains), all of this complex behavior is hidden by focusing on the net magnetic dipole moment per unit volume, or the magnetization $\vec{M}$. On exposed boundaries, the curl of $\vec{M}$ produces localized, macroscopic atomic currents

$$\vec{J}_{atomic} = \nabla \times \vec{M} \qquad (1.3.12)$$

which play no role in charge continuity. A second magnetic vector, the magnetic field strength $\vec{H}$, is usually defined

$$\vec{H} = v_o\vec{B} - \vec{M} \qquad (1.3.13)$$

In simple cases, $\vec{M}$ is proportional to $\vec{B}$,

$$\vec{M} = [\chi_b]\vec{B} + \vec{M}_o \tag{1.3.14}$$

where the constant $[\chi_b]$ is called the magnetic susceptibility and $\vec{M}_o$ is the remanent magnetization. In these cases, $\vec{H}$ is also proportional to $\vec{B}$,

$$\vec{H} = [v]\vec{B} \tag{1.3.15}$$

where $[v]$ is the reluctivity tensor. In other cases (steel, etc.) $[v]$ is a nonlinear function of $\vec{B}$. By taking the curl of Eq. (1.3.13), and combining the result with Eqs. (1.3.12), (1.3.2) and (1.2.10), it is straightforward to show that the sources of $\vec{H}$,

$$\nabla \times \vec{H} = \vec{J}_{cond} + \vec{J}_{disp} \tag{1.3.16}$$

exclude atomic currents. Both fields, $\vec{D}$ and $\vec{H}$, play a similar role in that they both exclude the effects of bound charges and currents. These effects are fully taken into account in the $\vec{E}$ and $\vec{B}$ fields.

1.3.2 Complex Properties

Materials sometimes have loss mechanisms that are not directly associated with ohmic heating. Examples of such behavior include lossy dielectrics and magnetic core losses. If fields vary sinusoidally, as $e^{i\omega t}$, then it may be convenient to represent non-ohmic losses with complex material properties. Under these assumptions the permittivity, conductivity and reluctivity all have real and imaginary parts.

In the case of anisotropic materials, the real and imaginary parts are represented by separate 3x3 matrices (tensors)

$$
\begin{aligned}
[\epsilon] &= [\epsilon'] + i[\epsilon''] \\
[\sigma] &= [\sigma'] + i[\sigma''] \\
[v] &= [v'] + i[v'']
\end{aligned}
\tag{1.3.17}
$$

The net effect of complex material properties can be seen by examining Ampere's law, Eq. (1.3.16). Assuming that all material properties are isotropic and linear, that the imaginary parts of the material constants are small compared to the real parts, and by neglecting remanent magnetization, Ampere's law can be written in terms of $\vec{E}$ and $\vec{B}$ as

$$\nabla \times v\vec{B} = (\sigma + i\omega\epsilon)\vec{E} \tag{1.3.18}$$

By substituting the expression in Eqs (1.3.17) through (1.3.18), the following is obtained:

$$\nabla \times v'(1 + i(v''/v'))\vec{B} = (\sigma' + i\sigma'' + i\omega(\epsilon' + i\epsilon''))\vec{E} \tag{1.3.19}$$

If this equation is multiplied by $(1-i\,(v''/v'))$ and results are kept to first order in the complex material constants, the result is

$$\nabla \times v'\vec{B} = (\sigma' - \omega\epsilon'' + (v''/v')\omega\,\epsilon' + i\omega(\epsilon' + (\sigma''/\omega) - (v''/v')(\sigma'/\omega)))\vec{E} \tag{1.3.20}$$

Lumping the effects of complex material properties into the conductivity and the dielectric constant is somewhat arbitrary.

By comparing Eqs. (1.3.18) and (1.3.20), it can be seen that the net effect of complex material properties is to produce a new effective conductivity and dielectric constant. In particular

$$\sigma = \sigma' - \omega\epsilon'' + \left(\frac{v''}{v'}\right)\omega\epsilon' \qquad (1.3.21)$$

$$\epsilon = \epsilon' - \omega\epsilon'' - \left(\frac{v''}{v'}\right)\left(\frac{\sigma'}{\omega}\right) \qquad (1.3.22)$$

The assumption of small, isotropic imaginary parts is made here only for the sake of illustrating the effects of complex material properties. The EMAS formulation is capable of treating the general case of large, anisotropic, complex material constants in all of its frequency domain solutions. The analytic interpretation of the general case is, however, much more difficult.

1.4 THE VECTOR POTENTIAL FORMULATION OF ELECTROMAGNETICS

For over 100 years, Maxwell's equations have described classical electrodynamic behavior. These four, first-order partial differential equations relate the space and time variation of electric and magnetic fields to macroscopic material properties, and to excitations. Together, they describe a broad range of behavior, including electrostatics, magnetostatics, eddy currents, cavity resonance, waveguides, antennas, radar scattering, and optical phenomena. Thus, Maxwell's equations form the basis for the analysis of virtually every electromagnetic device—everything from computer microcircuitry, to large power generators and transformers. The purpose of this section (Figure. 1.4.1) is to restate Maxwell's equations in the context of the material model described in Section 1.3, and then to introduce electromagnetic potential functions in a novel form, a form that greatly simplifies finite element analysis.
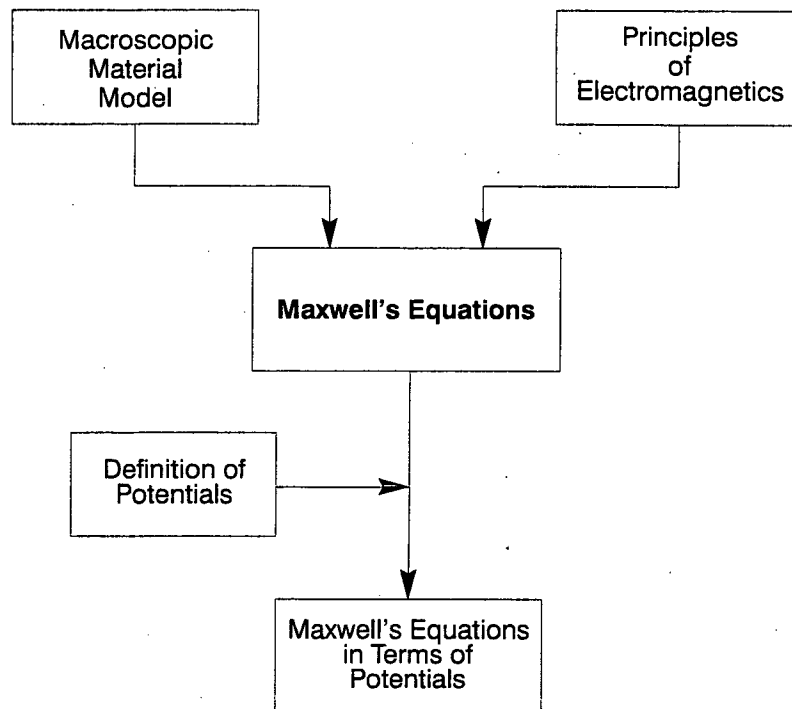
Figure 1.4.1: Vector potential formulation of electromagnetics.

In the notation of vector calculus, Maxwell's equations of electromagnetics are represented by Eqs. (1.2.8), (1.2.12), (1.3.9), (1.3.10), and (1.3.16). They are traditionally written as

$$\nabla \cdot \vec{D} = \rho_{free} \tag{1.4.1}$$

$$\nabla \cdot \vec{B} = 0 \tag{1.4.2}$$

$$\nabla \times \vec{E} = -\dot{\vec{B}} \tag{1.4.3}$$

$$\nabla \times \vec{H} = \vec{J}_{cond} + \dot{\vec{D}} \tag{1.4.4}$$

These four equations state the following:

- Gauss's law: the sources of $\vec{D}$ are free charge.

- $\vec{B}$ has no sources.

- Faraday's law: electric fields are induced by time-varying magnetic fields.

- Ampere's law: the sources of $\vec{H}$ are conduction current plus the displacement current.

EMAS solves these general equations, but only after introducing potential functions to simplify the analysis.

There are three disadvantages to solving Eqs. (1.4.1–4) directly for the unknown vectors $\vec{E}$ and $\vec{B}$. The six unknown components of these two fields cannot be chosen arbitrarily because they are related through Maxwell's equations. Thus, the number of unknowns is larger than is actually needed. The second disadvantage is related to discontinuities in material properties. There are two well-known boundary conditions that must be met at such interfaces: (1) the normal component of $\vec{D}$ must be continuous across the interface (because there is no free charge present); (2) the tangent component of $\vec{H}$ must also be continuous (because there is no conduction or displacement current). Any solution strategy that involves $\vec{E}$ and $\vec{B}$ must enforce these conditions at every interface; potentially at all surfaces of every finite element. This requirement puts an unnecessary burden on numerical computations. The third disadvantage is that $\vec{E}$ and $\vec{B}$ may be infinite at sharp corners of certain materials, and infinite solutions (singularities) cause severe problems on digital computers.

1.4.1   Electromagnetic Potentials

Electromagnetic potential functions are introduced to eliminate the disadvantages of dealing with $\vec{E}$ and $\vec{B}$ directly. Since the divergence of $\vec{B}$ is always zero, Eq. (1.4.2), it must be the curl of some vector $\vec{A}$, the vector potential

$$\vec{B} = \nabla \times \vec{A} \tag{1.4.5}$$

The electric field is also usually expressed in terms of the vector potential, and the scalar potential ϕ

$$\vec{E} = -\nabla\phi - \dot{\vec{A}} \tag{1.4.6}$$

In order to simplify the final finite element equations, a slightly different form is used in EMAS.

$$\vec{E} = -\nabla\psi - \dot{\vec{A}} \tag{1.4.7}$$

The three components of the vector potential and the unconventional scalar potential ψ represent the unknown quantities in EMAS. The conventional potential ϕ is (to within a constant) the time derivative of the new scalar potential. This small change has a profound effect on the symmetry and unity of the finite element formulation of electromagnetics.

Results can now be combined to write Maxwell's equations in terms of the new potential functions. By combining Maxwell's equations, Eqs. (1.4.1-4), the potential relations, Eqs. (1.4.5) and (1.4.7), the general definitions of $\vec{D}$ and $\vec{H}$, Eqs. (1.3.8) and (1.3.13), the charge continuity relation, Eq. (1.3.4), and Ohm's law, Eq. (1.3.5), the following is obtained:

$$\nabla \times ([\nu](\nabla \times \vec{A})) = -[\sigma](\nabla\psi + \dot{\vec{A}}) - [\epsilon](\nabla\dot{\psi} + \ddot{\vec{A}}) + \nabla \times \vec{M}_o \tag{1.4.8}$$

$$\nabla \cdot [\epsilon](\nabla\psi + \dot{\vec{A}}) = -\rho_o + \nabla \cdot \vec{P}_o - \int_{t_o}^{t} dt'(\nabla \cdot [\sigma](\nabla\psi + \dot{\vec{A}})) \tag{1.4.9}$$

Note that $\vec{P}_o$ contributes to the static charge density. These two expressions represent, in potential form, Ampere's law describing the origins of magnetic fields as conduction current and displacement current and Gauss's law describing the sources of electric fields. The other two Maxwell equations Eqs.(1.4.2) ($\vec{B}$ has no sources) and Faraday's law of induction Eq. (1.4.3) are automatically satisfied by the form of the potential substitutions, Eqs. (1.4.5) and (1.4.7). This new form of Maxwell's equations is fully equivalent to the original conventional form.

The physical interpretation of the scalar potential ψ in terms of ϕ is relatively straightforward. In electrostatics, ϕ represents the energy acquired by a test charge in moving to a given point from some reference point. ϕ is commonly called the voltage (of a battery, for example). It is easiest to think of ψ as simply the time integral of ϕ. For example, a constant voltage would be described by a ψ function increasing at a constant rate. ψ can also be thought of as a gauge function, as described below.

A simple, physical interpretation of the vector potential $\vec{A}$ has long eluded scientists. It is possible to argue that $\vec{A}$ is simply a mathematical convenience, without physical significance. For many, this answer is unsatisfactory. One somewhat mathematical interpretation comes from the vector integral equation for $\vec{A}$ in terms of current sources

$$\vec{A} = \frac{\mu_o}{4\pi} \int_v dv \, \frac{\vec{J}_{cond}}{r} \tag{1.4.10}$$

where r is the distance from the source to the evaluation point. This expression should be compared with a similar expression for ϕ in terms of its sources, electric charge

$$\phi = (4\pi\epsilon_o)^{-1} \int_v dv \frac{\rho}{r} \tag{1.4.11}$$

In the sense that ϕ is a potential energy function resulting from a distribution of charges, so $\vec{A}$ is a vector potential function resulting from an assembly of currents.

The significance of $\vec{A}$ may be somewhat deeper. The propagation of light waves through vacuum requires that $\vec{E}$ and $\vec{B}$ interact with each other. But $\vec{E}$ and $\vec{B}$ are just fields, which describe the forces acting between charges and currents. Since these sources are not present in vacuum, the underlying basis for interaction is not clear. On the other hand, a number of advanced theories including quantum mechanics, superconductivity, and special relativity use the vector potential rather than the fields to describe such interactions. The use of $\vec{A}$ results in increased mathematical symmetry. In special relativity, electric and magnetic fields are intermixed by relative motion, since charges in one reference frame represent currents in a moving frame. Thus $\vec{E}$ and $\vec{B}$ are not totally independent entities but are separate aspects of the same unknown quantity. This unknown quantity is related to the vector potential.

1.4.2   Vector Potential Uniqueness

It has long been known that Maxwell's equations do not uniquely specify the vector potential $\vec{A}$ (Figure. 1.4.2). For example, since Maxwell's equations involve $\vec{A}$ through space and time derivatives, the addition of a uniform constant vector $\vec{A}_o$ leaves the physical fields (and forces) unchanged. Other parts of $\vec{A}$ are also undefined. In fact, the only part of $\vec{A}$ defined by Maxwell's equations is its curl. In analysis these undefined portions are seldom a concern since analytic solutions can always be structured to avoid them. In numerical work, undetermined parts lead to singular matrices, resulting in **ill-conditioned** statics problems, and nonphysical resonant modes (called spurious modes). Care must be taken to eliminate these singularities. Relevant modeling practices are described in Section 2. The theoretical basis for these practices is described here.
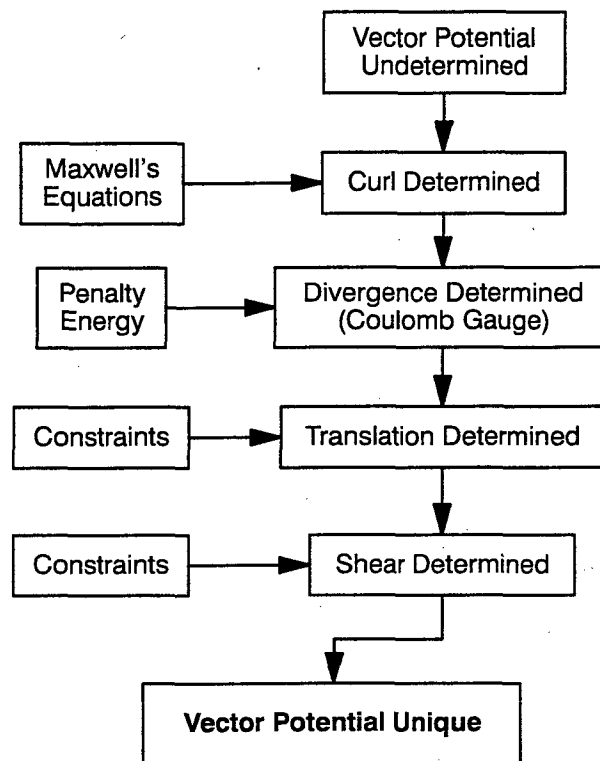
Figure 1.4.2: Vector potential uniqueness.

In order to better visualize the vector field, it is helpful (temporarily) to interpret $\vec{A}$ as actual, physical displacement, much like the displacement field $\vec{u}$ in elasticity. The zero- and first-order functional dependencies of the vector potential can be visualized as distortions of a unit cube. All classes of these zero- and first-order displacements are shown in Figure. 1.4.3. Translation corresponds to adding a uniform, constant vector to $\vec{A}$, as described above. Divergence is represented by a uniform "swelling" of the cube, causing an increase in volume. Shear corresponds to distortion of angles without rotation or volume increase. The only displacement of any physical consequence is curl that corresponds to a uniform rotation.

The curl shown corresponds to a uniform $\vec{B}$ pointing out of the front face of the cube. All other classes of displacement produce no fields or energy, and thus, represent singular displacements of the vector potential. Higher-order singular motions are possible, but these are not supported by first-order finite elements.
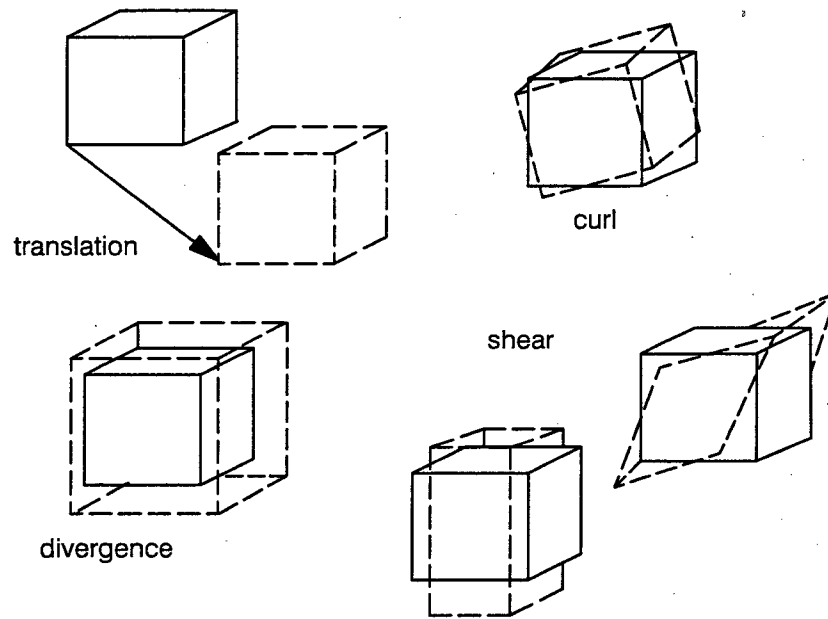
Figure 1.4.3: Elementary displacements of the vector potential.

The methods used to eliminate singular motions depend on their behavior in assemblies of elements. Divergence singularities are often localized; so that a model can possess a large number of independent divergence motions, all of which represent singularities. In contrast, translation and shear can only be present in a global sense; i.e., if uniform shear is present anywhere, it must be present everywhere in equal amounts. Thus, only a small number of singular shear and translation motions are present. EMAS eliminates divergence singularities by imposing the Coulomb gauge condition, using a penalty function method. While this choice has no effect on the resulting fields, it does affect the relationship between the scalar and vector potential functions. The small number of translation and shear singularities are eliminated by constraints.

Gauge Transformations

The form of the potential substitutions, Eq. (1.4.5) and (1.4.7), leave undetermined the divergence of $\vec{A}$, and the relationship between $\vec{A}$ and ψ. Apparently, if $\vec{A}$ is transformed according to

$$\vec{A}' = \vec{A} + \nabla\xi \tag{1.4.12}$$

there will be no change in the resulting magnetic fields, even for arbitrary choices of the gauge function ξ. Similarly, the electric field will be left unchanged if the following transformation is applied:

$$\psi' = \psi - \dot{\xi} \tag{1.4.13}$$

(This result suggests an interpretation of the electrostatic potential ψ; it may be thought of as a gauge function.) The point to note is that the transformations for $\vec{A}$ and ψ are coupled, so that the particular choice for ξ has an effect on the information content of the potentials, even though the physical fields are unchanged.

It is apparent from Eq. (1.4.12) that $\nabla \cdot \vec{A}$ can be made any arbitrary function by the proper selection of ξ. The gauge is set by constraining $\nabla \cdot \vec{A}$ to some particular function. There are two popular choices used in analytical work: the Lorentz gauge, and the Coulomb gauge. These two gauges have different effects on the dynamic equations, and on the information contained in each of the potentials.

LORENTZ GAUGE

The Lorentz gauge is derived from the form of Maxwell's equations, expressed in terms of the potentials. Equations (1.4.8) and (1.4.9) can be written as follows:

$$\nu\nabla^2\vec{A} - \epsilon\ddot{\vec{A}} - \nu\nabla(\nabla \cdot \vec{A} + \frac{\epsilon}{\nu}\dot{\psi}) = -\vec{J}_{cond} - \nabla \times \vec{M}_0 \tag{1.4.14}$$

$$\nabla^2\psi + \nabla \cdot \dot{\vec{A}} = -\frac{\rho_{free}}{\epsilon} \tag{1.4.15}$$

To simplify the discussion, all materials are assumed to be isotropic and linear (ϵ, ν and σ are simply scalar constants). The Lorentz gauge condition is chosen to make the third term in Eq. (1.4.14) zero, i.e.

$$\nabla \cdot \vec{A} = -\frac{\epsilon}{\nu}\dot{\psi} \tag{1.4.16}$$

With this condition Maxwell's equations reduce to two, uncoupled, nonhomogeneous wave equations for $\vec{A}$ and ψ

$$\nabla^2\nu\vec{A} - \epsilon\ddot{\vec{A}} = -\vec{J}_{cond} - \nabla \times \vec{M}_0 \tag{1.4.17}$$

$$\nabla^2(\psi) - \frac{\epsilon}{\nu}\frac{\partial^2(\psi)}{\partial t^2} = -\frac{\rho_{free}}{\epsilon} \tag{1.4.18}$$

Although this separation is highly desirable in analytic work, it is very awkward for numerical analysis; because the gauge condition, which involves material properties as well as space and time derivatives of the potentials, is difficult to implement.

COULOMB GAUGE

The Coulomb gauge is designed to make the second term in Eq. (1.4.15) zero, and thus isolate Coulomb's law from any dynamic effects due to $\vec{A}$. When the Coulomb gauge,

$$\nabla \cdot \vec{A} = 0, \tag{1.4.19}$$

is imposed, Maxwell's equations reduce to

$$\nu\nabla^2\vec{A} - \epsilon\ddot{\vec{A}} = -\vec{J}_t - \nabla \times \vec{M}_0, \tag{1.4.20}$$

$$\nabla^2\psi = -\frac{\rho_{free}}{\epsilon} \tag{1.4.21}$$

$\vec{A}$ still obeys the wave equation; but now the origins of $\vec{A}$ are the divergence free component of the conduction current $\vec{J}_t$ and the (divergence free) curl of $\vec{M}_0$. The curl free component of the conduction current $\vec{J}_l$ no longer has (and never did) any effect on $\vec{A}$ or $\vec{B}$. The historical names for $\vec{J}_t$ and $\vec{J}_l$ are the transverse and longitudinal current densities. For this reason the Coulomb gauge is also called the transverse gauge.

Under the Coulomb gauge the electrostatic potential no longer obeys the wave equation; but instead obeys Gauss's law for electrostatics. Charge conservation and the continuity condition now only involve the scalar potential. Any dynamic or wave propagation effects are completely removed from ψ. For this reason ψ is often called the instantaneous potential. The electric field still has the proper dynamic effects but they are now contained solely in $\vec{A}$.

Translation and Shear Singularities

The small number of translation and shear singularities are removed through the application of constraints.

In the case of translation the form of the constraint is clear: simply constrain all three components of $\vec{A}$ to some particular value at one point. This removes translation singularities by defining explicitly the uniform translation vector $\vec{A}_o$. The technique for constraining shear is similar but slightly more complicated. In first order there are five independent shear motions in three dimensions. The value of shear is obtained from the following operators

$$S_{yz} = \frac{\partial A_z}{\partial y} + \frac{\partial A_y}{\partial z} \tag{1.4.22}$$

$$S_{xz} = \frac{\partial A_x}{\partial z} + \frac{\partial A_z}{\partial x} \tag{1.4.23}$$

$$S_{xy} = \frac{\partial A_y}{\partial x} + \frac{\partial A_x}{\partial y} \tag{1.4.24}$$

$$d_{xy} = \frac{\partial A_x}{\partial x} - \frac{\partial A_y}{\partial y} \tag{1.4.25}$$

$$d_{xz} = \frac{\partial A_x}{\partial x} - \frac{\partial A_z}{\partial z} \tag{1.4.26}$$

A variety of constraint schemes are possible using both SPCs and MPCs. These all, by one means or another, constrain degrees of freedom in such a way that the five independent shear motions are given specific values (usually zero) without affecting the resulting fields. Similar techniques apply in two dimensions, where (in first order) there are three singular translation motions and just two shear motions. More details on these procedures are given in Chapter 2.

1.5   THE PRINCIPLE OF VIRTUAL WORK

In order to adapt the vector potential formulation of electromagnetics to finite element analysis, it is first necessary to cast it in a variational form. The principle of virtual work (Figure 1.5.1) is used because, unlike the Galerkin method, it provides much useful information on boundary and initial conditions. The approach is first to develop an expression for virtual work that reduces to Maxwell's equations when methods from the calculus of variations are used. This process identifies the work associated with Neumann boundary conditions. These additional work terms are then added to the basic expression. Later, in Section 1.6, this integral expression is approximated using finite element techniques. Solutions to Maxwell's equations are then obtained by enforcing dynamic equilibrium through the solution of a matrix equation.
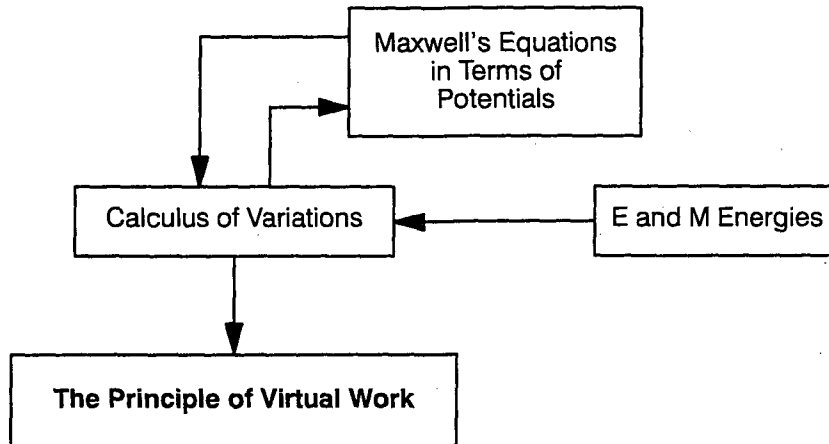
Figure 1.5.1: Principle of virtual work.

Some expressions for electromagnetic work are well known. Others are obtained with guidance from Maxwell's equations, Eqs. (1.4.8) and (1.4.9). The work associated with electric fields is simply

$$\delta W_e = \vec{D} \cdot \delta \vec{E} \tag{1.5.1}$$

for linear media. The work associated with magnetic fields is, in general

$$\delta W_b = -\vec{H} \cdot \delta \vec{B} \tag{1.5.2}$$

The work associated with charges is

$$\delta W_\rho = -\delta \phi (\rho_o - \nabla \cdot \vec{P}_o) \tag{1.5.3}$$

The work associated with remanent magnetization is

$$\delta W_m = -\delta \vec{A} \cdot (\nabla \times \vec{M}_o) \tag{1.5.4}$$

The work associated with dissipation can be written as

$$\delta W_\sigma = -(\delta(\nabla \psi) + \delta \vec{A}) \cdot \vec{J}_{cond} \tag{1.5.5}$$

An additional work term is required to impose the Coulomb gauge. This penalty term associates an artificial energy and work with the presence of $\nabla \cdot \vec{A}$. Since none of the other work terms couple to $\nabla \cdot \vec{A}$, and since

boundary conditions are carefully chosen to avoid exciting $\nabla \cdot \vec{A}$, solutions are always possible in which the divergence is zero. This term is given by

$$\delta W_\alpha = -\alpha[\nu] \, \delta(\nabla \cdot \vec{A}) \cdot (\nabla \cdot \vec{A}) \tag{1.5.6}$$

where the penalty parameter α has the same units as ν.

A variational principle for electromagnetics is obtained by adding work contributions from Eqs. (1.5.1-6), and integrating them over the problem volume, and over time. The resulting expression, written only in terms of $\vec{A}$ and $\dot{\psi}$, is

$$
\begin{aligned}
\delta w = \int_v dv \int_{t_o}^{t_1} dt \Big(& (\delta(\nabla\psi) + \delta\vec{A}) \cdot [\epsilon](\nabla\dot{\psi} + \vec{A}) \\
& - (\delta(\nabla\psi) + \delta\vec{A}) \cdot [\sigma](\nabla\psi + \vec{A}) \\
& - \delta(\nabla \times \vec{A}) \cdot [\nu](\nabla \times \vec{A}) \\
& - \alpha\delta\,[\nu](\nabla \cdot \vec{A})(\nabla \cdot \vec{A}) \\
& - \delta(\psi)(\rho_o - \nabla \cdot \vec{P}_o) \\
& + \delta\vec{A} \cdot (\nabla \times \vec{M}_o) \Big) = 0
\end{aligned}
\tag{1.5.7}
$$

It is this variational principle that serves as the basis for the finite element formulation of electromagnetics used in EMAS.

The principle of virtual work reduces to a statement of dynamic equilibrium between generalized forces. The differential equations equivalent to this principle are recovered by setting to zero the forces associated with the variations $\delta\vec{A}$ and $\delta\psi$. Maxwell's equations are not readily apparent in Eq. (1.5.7) because some of the variations still involve space and time derivatives. These derivatives can be easily removed through integration by parts. As a result of this process, additional surface and time end point terms are generated. These additional terms are then used to determine the virtual work associated with natural Neumann boundary conditions.

When the generalized forces associated with $\delta\vec{A}$ and $\delta\psi$ are set to zero after integration by parts, two differential equations are obtained. The first, associated with $\delta\vec{A}$, is exactly Eq. (1.4.8), the curl-curl equation for the vector potential

$$\nabla \times [\nu](\nabla \times \vec{A}) = -[\sigma](\nabla\dot{\psi} + \vec{A}) - [\epsilon](\nabla\dot{\psi} + \ddot{\vec{A}}) + \nabla \times \vec{M}_o \tag{1.5.8}$$

The penalty term, proportional to $\nabla(\nabla \cdot \vec{A})$, has been omitted since all valid solutions obey the Coulomb gauge. The second equation is not Eq. (1.4.9), but rather its first time derivative

$$-\nabla \cdot [\epsilon](\nabla\dot{\psi} + \ddot{\vec{A}}) = \nabla \cdot [\sigma](\nabla\psi + \vec{A}) \tag{1.5.9}$$

The only reason for obtaining the first time derivative is the mathematical substitution $\dot{\phi} = \psi$ used to define the potentials. The first term is immediately recognized as $\nabla \cdot \vec{D}$, which according to the first Maxwell equation, Eq. (1.4.1), is also ρ. The second term is clearly $-\nabla \cdot \vec{J}_{cond}$. Therefore Eq. (1.5.9) is simply the charge continuity condition, Eq. (1.3.3), written in terms of the vector potential. It is these equations, in finite element form, that are solved by EMAS.

The connection between variational principles and dynamics (initial condition problems) is tenuous. Formally, variational principles involve conditions at two distinct times: an initial time and an end time. The variational principle is then used to solve for the dynamical behavior between these two times. An initial condition problem specifies conditions at one initial time, and solves for subsequent motion. In order to make a transition from end point conditions to a single initial condition, it is assumed that at t_1, all quantities are zero (the universe has run down to its ultimate, zero-free energy state). Thus, the only significant dynamical condition is at the initial time.

The reader may have noticed that something is missing: the static charge distribution, $\rho_0 - \nabla \cdot \vec{P}_0$, from the fifth term in Eq. (1.5.7). In fact, Eqs. (1.5.8-9) contain no information about electrostatics at all. The reason for this is as follows: when the fifth term in Eq. (1.5.7) is integrated by parts with respect to time, the resulting volume integral is zero, because neither ρ_0 nor $\vec{P}_0$ depend on time. These terms appear only in the initial condition obtained from the first and fifth terms

$$\int_v dv\, \delta\psi\left(-\nabla \cdot [\epsilon]\left(\nabla\psi + \vec{A}\right) - \rho_0 + \nabla \cdot \vec{P}_0\right)\bigg|_{t_0} \tag{1.5.10}$$

In order for this term to be zero, either $\delta\psi$ is zero (i.e., ψ is specified as an initial condition) or the term in parentheses must be zero. This term is immediately recognized as Gauss's law for electrostatics. Thus, electrostatics is not formally a part of the equations of motion, but is instead treated as an initial condition.

The first term in Eq. (1.5.7) also generates an initial condition that deserves some discussion. This condition may be written as

$$\int_v dv\, \delta\vec{A} \cdot [\epsilon]\left(\nabla\psi + \vec{A}\right)\bigg|_{t_0} \tag{1.5.11}$$

For this term to be zero, either $\vec{A}$ must be fixed as an initial condition or $\vec{E}$ must be constrained to some specified value. The second choice is not acceptable because the electric fields are obtained as an initial condition by solving the electrostatics problem, Eq. (1.5.10). An arbitrary choice for $\vec{E}$ would not, in general, be consistent with the solution of this problem. Thus, $\vec{A}$ must be specified as an initial condition.

The choice of ψ, $\vec{A}$ and their first time derivatives as initial conditions are dictated by the use of the Coulomb gauge. $\vec{A}$ is chosen to represent the required initial distribution of $\vec{B} = \nabla \times \vec{A}$. ψ is taken as zero everywhere without loss of generality. The first time derivatives $\dot{\psi}$ and $\dot{\vec{A}}$ together must satisfy Coulomb's law for the initial static charge distribution. Since the Coulomb gauge is normally imposed, the divergence of $\dot{\vec{A}}$ is zero so that $\dot{\psi}$ by itself accounts for all the initial charge. $\dot{\vec{A}}$ is then chosen to represent any divergence-free electric fields that may be present, e.g., an external uniform field or an impinging plane wave. When the divergence operator acts on Eq. (1.5.10), the result is always zero, and $\dot{\psi}$ alone accounts for the initial charge distribution. The basic electrodynamic initial conditions are summarized in Figure 1.5.2.

Quantity	Chosen to Represent
$\vec{A}$	$\nabla \times \vec{B}$
$\dot{\vec{A}}$	divergence $-$ free $\vec{E}$
ψ	0
$\dot{\psi}$	electrostatic charge

Figure 1.5.2: Electrodynamic initial conditions.

A number of surface terms are generated when integrating the virtual work, Eq. (1.5.7). These terms identify the work associated with natural boundary conditions. The spatial integration by parts on the first term generates an initial boundary condition to be met when solving Gauss's law, Eq. (1.5.10), for the initial electrostatic potential

$$-\int_s ds\,\delta\psi(\hat{n} \cdot (\vec{D} - \vec{P}_o))\Big|_{t_0} \tag{1.5.12}$$

where $\hat{n}$ is the outward directed unit normal to the surface ds, and the integral is over the problem boundary. This term may be generalized by adding the work done by fixed values of the displacement and remanent polarization, $\vec{D}^*$ and $\vec{P}_o^*$

$$\int_s ds\,\delta\psi\,(\hat{n} \cdot (\vec{D}^* - \vec{P}_o^* - \vec{D} + \vec{P}_o))\Big|_{t_0} \tag{1.5.13}$$

This more general term can be interpreted as follows: either ψ (and $\dot{\psi}$) is fixed on the boundary, or the sum $\vec{D} + \vec{P}_o$ must be equal to the specified value. These are immediately recognized as the natural Dirichlet and Neumann boundary conditions for initial electrostatics problems. The additional work term must, of course, be added to the expression for virtual work, Eq. (1.5.7).

Other terms are associated with boundary conditions. The term associated with $\delta\vec{A}$ is generalized to

$$-\int_s ds \int_{t_0} dt\,\delta\vec{A} \cdot ((\vec{H} + \vec{M}_o - \vec{H}^* - \vec{M}_o^*) \times \hat{n}) \tag{1.5.14}$$

For this term to be zero, either tangent $\vec{A}$ must be fixed on the boundary (the natural Dirichlet condition), or the sum tangent $\vec{H} + \vec{M}_o$ must be equal to its specified value (the natural Neumann condition). Mixed conditions involving $\vec{A}$ and $\vec{H}$ may also be used to implement impedance boundary conditions. A similar term associated with $\delta\psi$ is generalized to

$$\int_s ds \int_{t_0} dt\,\delta\psi\,\hat{n} \cdot (\vec{J}_{cond} + \dot{\vec{D}} - \vec{J}_{cond}^* - \dot{\vec{D}}^*) \tag{1.5.15}$$

This term is zero provided that either ψ is constrained at the boundary (the natural Dirichlet condition) or the normal component of the current $\vec{J}_{cond} + \dot{\vec{D}}$ is equal to its specified value (the natural Neumann condition). In generalizing these expressions, terms corresponding to the work done by constrained field and current values have been added. These terms must also be added to the expression for virtual work, Eq. (1.5.7).

The surface term generated by integrating the penalty function, term four in Eq. (1.5.7), is also of some interest. The term has the following form:

$$-\int_s ds \int_{t_0} dt\,(\delta\vec{A} \cdot \hat{n})(\nabla \cdot \vec{A}) \tag{1.5.16}$$

This term is zero if the normal component of $\vec{A}$ is constrained at the boundary, or if the divergence of $\vec{A}$ is zero. The first choice is undesirable. If $\vec{A}_{normal}$ is constrained, then $\nabla \cdot \vec{A}$ is free to assume any value consistent with the constraint. This value could be nonzero, leading to nonzero divergence in the interior. Remember: $\nabla \cdot \vec{A}$ is not constrained to zero in the interior, it only tends to zero due to the penalty energy. Such a Dirichlet boundary condition on normal $\vec{A}$ would force the divergence, and thus violate the Coulomb gauge. The second choice, $\nabla \cdot \vec{A} = 0$ at the boundary (a homogeneous Neumann condition) is preferred. Note that a generalization involving work done by nonzero $\nabla \cdot \vec{A}$ is not desirable, so that no additional terms need be added to the virtual work.

The basic electromagnetic boundary conditions are summarized in Figure 1.5.3. More elaborate conditions are also possible by combining multiple constraints and excitations. Such conditions include ideal conductors, impedance conditions, and radiation boundary conditions.

$\vec{A}$ DOFs	ψ DOFs
Statics: Constrain Tangent $\vec{A}$ OR Excite Tangent $\vec{A}$ With Tangent $\vec{H}$	Statics: Constrain ψ OR Excite ψ with Normal J or D
Dynamics: same	Dynamics: Constrain ψ (and $\dot{\psi}$) OR Excite ψ with Normal $\vec{J}_{cond} + \dot{\vec{D}}$

Figure 1.5.3: Basic E&M boundary conditions.

The complete expression for electromagnetic virtual work may now be written. By combining Eq. (1.5.7) with the additional surface and end point terms described above, the following expression is obtained:

$$
\begin{aligned}
\delta w = \int_{vol} dv \int_{t_o} dt \Big(& (\delta(\nabla\psi) + \delta\vec{A}) \cdot [\epsilon](\nabla\dot\psi + \dot{\vec{A}}) \\
& - (\delta(\nabla\psi) + \delta\vec{A}) \cdot [\sigma](\nabla\dot\psi + \dot{\vec{A}}) \\
& - \delta(\nabla \times \vec{A}) \cdot [\nu](\nabla \times \vec{A}) \\
& - \alpha\delta\,[\nu](\nabla \cdot \vec{A}) \cdot (\nabla \cdot \vec{A}) \\
& - \delta\psi\,(\rho_o - \nabla \cdot \vec{P}_o) \\
& + \delta\vec{A} \cdot (\nabla \times \vec{M}_o) \Big) \\
+ \int_{surf} ds \int_{t_o} dt\Big(& \delta\vec{A} \cdot \big((\vec{H} + \vec{M}_o)^* \times \hat{n}\big) \\
& - \delta\psi\,(\hat{n} \cdot (\vec{J} + \dot{\vec{D}})^*)\Big) \\
+ \int_{surf} ds\,\delta\psi\,\Big(\hat{n} & \cdot (\vec{D} - \vec{P}_o)^*\Big)\Big|_{t_o}
\end{aligned}
$$

(1.5.17)

This expression is the energy variation used by EMAS.

On the whole, the formulation of electromagnetics used in EMAS is fairly conventional. However, the use of $\psi = \phi$ as the electrostatic potential gives the equations of motion a rather unusual form. Using a conventional material model and Maxwell's equations as a starting point, variational methods were used to obtain equations for the vector and scalar potentials. The standard curl-curl equation for $\vec{A}$ was recovered; however, Gauss's law for static charge now appears as an initial condition. Dynamic charge behavior is specified by the continuity equation. As shown in the next section, the use of ψ gives the finite element formulation a remarkable symmetry and simplicity.

1.6   FINITE ELEMENT ANALYSIS OF ELECTROMAGNETIC FIELDS

Once an appropriate variational principle has been established, the finite element formulation of electromagnetics is obtained in a straightforward manner (Figure 1.6.1). The objective of the analysis is to solve for the unknown potentials $\vec{A}$ and ψ by setting the generalized forces associated with virtual work to zero (enforcing dynamic equilibrium). The approach is to divide the integration volume into finite elements. Within each element, the potentials are given a simple, low-order polynomial dependence. This dependence is specified by unknown coefficients, called degrees of freedom (DOFs), which also happen to be the values of the potentials at predetermined nodes. The virtual work associated with each element is computed in terms of the degrees of freedom; the results are then summed over the elements to represent the work of the entire problem volume. When the generalized forces are set to zero, a single equation is obtained. This equation is entirely equivalent to Maxwell's equations in their complete and general form.
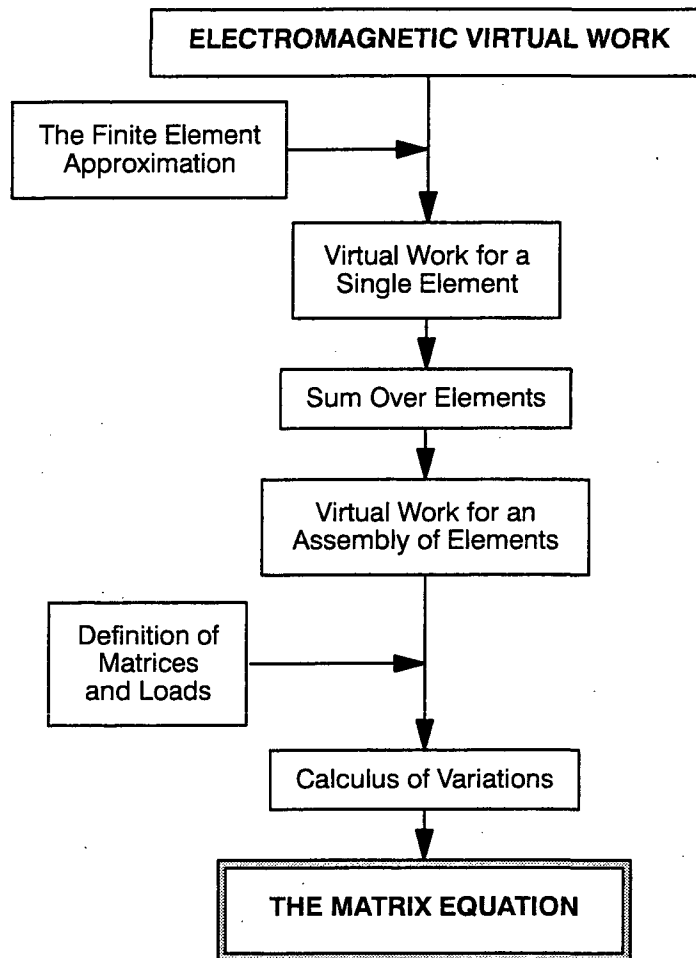
Figure 1.6.1: Finite element formulation of electromagnetics.

1.6.1　The Finite Element Approximation

The problem volume represents a finite region in physical space, in which approximate solutions to Maxwell's equations are obtained. This volume may be either one-, two-, or three-dimensional, or axisymmetric. In principle, fields fill all space out to an infinite distance from their sources. This infinite volume, however, cannot be modeled directly. Instead, infinite volumes are replaced by appropriate boundary conditions, or by infinite elements designed to mimic the effects of the missing volume.

The problem geometry is often quite complex, involving many physical objects with complex geometrical and material properties. To simplify the modeling and solution process, the problem volume is divided into many finite elements, each with much simpler properties. The elements themselves are geometrically close (within the limits of good modeling practice) to standard figures, e.g., a brick. Within each element, material properties are considered uniform. Through the use of simple finite elements it is possible to model a variety of complicated electromagnetic devices.

The functional dependence of the potentials $\vec{A}$ and ψ is simplified within each finite element. Assume that the potentials are given by a general polynomial expansion

$$A_x(\vec{r}, t) = N_1(\vec{r})A_{x1}(t) + N_2(\vec{r})A_{x2}(t) + \dots \tag{1.6.1}$$

$$A_y(\vec{r}, t) = N_1(\vec{r})A_{y1}(t) + N_2(\vec{r})A_{y2}(t) + \dots \tag{1.6.2}$$

$$A_z(\vec{r}, t) = N_1(\vec{r})A_{z1}(t) + N_2(\vec{r})A_{z2}(t) + \dots \tag{1.6.3}$$

$$\psi(\vec{r}, t) = N_1(\vec{r})\psi_1(t) + N_2(\vec{r})\psi_2(t) + \dots \tag{1.6.4}$$

where the shape functions N_i depend only on position $\vec{r}$, and the degrees of freedom A_{xi}, A_{yi}, A_{zi}, and ψ_i depend only on time. The discussion here assumes that $\vec{A}$ is expressed in a Cartesian (x,y,z) coordinate system. A similar discussion applies in other coordinate systems with suitable adjustments in notation and differential operators. The shape functions are chosen so that the degrees of freedom also correspond to the values of the potentials at (mathematical) locations, called nodes, within the elements. These nodes are given physical position by associating them with grid points during the modeling process. The number of nodes varies depending on the element type. There are four degrees of freedom at each node: one DOF for each of the unknown functions A_{xi}, A_{yi}, A_{zi}, and ψ_i.

It is convenient to introduce matrix notation. Eqs. (1.6.1-4) can be written as a single matrix equation

$$\left\{ \begin{matrix} \vec{A} \\ \psi \end{matrix} \right\} = [N] \left\{ \begin{matrix} \vec{A}_i \\ \psi_i \end{matrix} \right\} = [N][u^e] \tag{1.6.5}$$

where $\left\{ \begin{matrix} \vec{A} \\ \psi \end{matrix} \right\}$ is a 4 x 1 column vector representing the time and spatial dependence of the potentials. If there are n nodes in a given element, then the shape function matrix [N] associated with that element is 4 x 4n in size, while the element DOF vector $\{u^e\}$ is a 4n x 1 column vector. [N] has the form

$$[N] = \begin{bmatrix} N_1 & 0 & 0 & 0 & N_2 & 0 & 0 & 0 \\ 0 & N_1 & 0 & 0 & 0 & N_2 & 0 & 0 \\ 0 & 0 & N_1 & 0 & 0 & 0 & N_2 & 0 \\ 0 & 0 & 0 & N_1 & 0 & 0 & 0 & N_2 \end{bmatrix} \cdots \; , \qquad (1.6.6)$$

where the number of partitions is equal to the number of nodes. The vector $\{u^e\}$ has the form

$$\{u^e\} = \left[A_{x1}, \; A_{y1}, \; A_{z1}, \; \psi_1 \; \middle| \; A_{x2}, A_{y2}, A_{z2}, \psi_2 \; \middle| ... \right]^T \qquad (1.6.7)$$

where, again, the number of partitions is equal to the number of nodes.

The time and space derivatives of the potentials can also be represented in matrix notation, using shape functions and DOFs. Since the time dependence of the solutions is contained entirely within $\{u^e\}$, time derivatives are expressed as the basic shape function matrix times the appropriate time derivative of the DOF vector.

For example, the time derivative of $\vec{A}$ and ψ is simply

$$\left\{ \begin{matrix} \dot{\vec{A}} \\ \dot{\psi} \end{matrix} \right\} = [N]\{\dot{u}^e\} \qquad (1.6.8)$$

The shape functions are considered constant with respect to variations, so

$$\delta \left\{ \begin{matrix} \vec{A} \\ \psi \end{matrix} \right\} = [N]\delta\{u^e\} \qquad (1.6.9)$$

Conversely, spatial derivatives operate only on the shape function matrix. For example, the curl operator is expressed as

$$\nabla \times \vec{A} = [\nabla \times N]\{u^e\} \qquad (1.6.10)$$

where $[\nabla \times N]$ is given by

$$[\nabla \times N] = \begin{bmatrix} 0 & -\dfrac{\partial N_1}{\partial z} & \dfrac{\partial N_1}{\partial y} & 0 & 0 & -\dfrac{\partial N_2}{\partial z} & \dfrac{\partial N_2}{\partial y} & 0 \\ +\dfrac{\partial N_1}{\partial z} & 0 & -\dfrac{\partial N_1}{\partial x} & 0 & +\dfrac{\partial N_2}{\partial z} & 0 & -\dfrac{\partial N_2}{\partial x} & 0 \\ -\dfrac{\partial N_1}{\partial y} & \dfrac{\partial N_1}{\partial x} & 0 & 0 & -\dfrac{\partial N_2}{\partial y} & \dfrac{\partial N_2}{\partial x} & 0 & 0 \end{bmatrix} \cdots \qquad (1.6.11)$$

Similarly, the divergence of $\vec{A}$ can be written as

$$\nabla \cdot \vec{A} = [\nabla \cdot N]\{u^e\} \tag{1.6.12}$$

where $[\nabla \cdot N]$ is a 1x4n row vector

$$[\nabla \cdot N] = \left\{ \frac{\partial N_1}{\partial x}, \frac{\partial N_1}{\partial y}, \frac{\partial N_1}{\partial z}, 0 \, \bigg| \, \frac{\partial N_2}{\partial x}, \frac{\partial N_2}{\partial y}, \frac{\partial N_2}{\partial z}, 0 \, \bigg| ... \right\} \tag{1.6.13}$$

The resulting product is a scalar. Finally, the combination, $\nabla \psi + \vec{A}$, appears frequently. This combination can be written as

$$\nabla \psi + \vec{A} = [\nabla N]\{u^e\} \tag{1.6.14}$$

where $[\nabla N]$ is the 3 x 4n matrix

$$[\nabla N] = \begin{bmatrix} N_1 & 0 & 0 & \frac{\partial N_1}{\partial x} & N_2 & 0 & 0 & \frac{\partial N_2}{\partial x} \\ 0 & N_1 & 0 & \frac{\partial N_1}{\partial y} & 0 & N_2 & 0 & \frac{\partial N_2}{\partial y} \\ 0 & 0 & N_1 & \frac{\partial N_1}{\partial z} & 0 & 0 & N_2 & \frac{\partial N_2}{\partial z} \end{bmatrix} \cdots \tag{1.6.15}$$

The use of this matrix notation will greatly simplify the results that follow.

1.6.2   The Matrix Equation

The matrix equation is obtained by substituting the finite element approximations and matrix notation into the expression for the virtual work of the entire system (Figure 1.6.1). The process begins by deriving the virtual work for a single element, and expressing it in terms of the DOFs and shape function matrices. The total work is then obtained by summing contributions from individual elements in a matrix assembly process. Then an equation for all DOFs is obtained by setting generalized forces equal to zero. Solutions to this final equation describe the time evolution of all DOFs in the system. Spatial dependence within elements can then be recovered at any instant in time by interpolating the shape functions.

The virtual work for a single element is obtained by combining the virtual work for continuous variables, Eq. (1.5.17), with the shape function notation just described. The result can be written as

$$\delta w_e = \int_{vol_e} dv \int_{t_0} dt \left(\left([\nabla N]\delta\{u^e\}\right)^T [\epsilon] \left([\nabla N]\{\dot{u}^e\}\right)\right.$$

$$- \left([\nabla N]\delta\{u^e\}\right)^T [\sigma]([\nabla N]\{\ddot{u}_e\})$$

$$- ([\nabla \times N]\delta\{u^e\})^T [\nu]([\nabla \times N]\{u^e\})$$

$$- \alpha[\nu]([\nabla \cdot N]\delta\{u^e\})^T([\nabla \cdot N]\{u^e\})$$

$$- \left([N]\delta\{u^e\}\right)^T \{s\}\left(\rho_o - \nabla \cdot \vec{P}_o\right) \qquad (1.6.16)$$

$$+ \left([N]\delta\{u^e\}\right)^T\left([\nu]\nabla \times \vec{M}_o\right) \Bigg)$$

$$+ \int_{surf_e} ds \int_{t_0} dt\left(([N]\delta\{u^e\})^T[\nu](\vec{H}^* + \vec{M}_o^*) \times \hat{n}\right.$$

$$- ([N]\delta\{u^e\})^T\{s\}(\hat{n} \cdot (\vec{J}_{cond}^* + \vec{D}^*))\Bigg)$$

$$+ \int_{surf_e} ds([N]\delta\{u^e\})^T\{s\}(\hat{n} \cdot (\vec{D}^* - \vec{P}_o^*))\Bigg|_{t_0}$$

where the 4 x 1 column vector {s} given by

$$\{s\} = \begin{Bmatrix} 0 \\ 0 \\ 0 \\ 1 \end{Bmatrix} \qquad (1.6.17)$$

maps scalar quantities into the corresponding ψ DOF locations within {u}, and the 4x3 matrix [v]

$$[v] = \begin{bmatrix} 1 & 0 & 0 \\ 0 & 1 & 0 \\ 0 & 0 & 1 \\ 0 & 0 & 0 \end{bmatrix} \qquad (1.6.18)$$

maps a vector into the corresponding $\vec{A}$ locations. The last three terms of (1.6.16) are used only when element surface excitations are on the problem boundary.

Equation (1.6.16) can be written in a condensed form by the introduction of suitable notation. In particular, since the DOF vectors $\{u^e\}$ only depend on time and not on position, they may be brought out of the volume and surface integrals. The result can be written as

$$
\begin{aligned}
\delta w_e = \int_{t_0} dt \Big(& \delta\{\dot{u}^e\}^T [M_e]\{\dot{u}^e\} - \delta\{u^e\}^T [B_e]\{\dot{u}^e\} \\
& - \delta\{u^e\}^T [K_e^{crl}]\{u^e\} - \delta\{u^e\}^T [K_e^{div}]\{u^e\} \\
& - \delta\{\dot{u}^e\}^T \{\rho_0^e\} + \delta\{u^e\}^T \{M_0^e\} + \delta\{u^e\}^T \{H^e\} \\
& + \delta\{u^e\}^T \{J^e\} \Big) \\
& - \delta\{u^e\}^T \{D^e\}\Big|_{t_0}
\end{aligned}
\tag{1.6.19}
$$

The integration over the element volume has been absorbed into the expressions for the element dielectric, conduction, and reluctivity matrices

$$
[M_e] = \int_{vol_e} dv [\nabla N]^T [\epsilon][\nabla N]
\tag{1.6.20}
$$

$$
[B_e] = \int_{vol_e} dv [\nabla N]^T [\sigma][\nabla N]
\tag{1.6.21}
$$

$$
[K_e^{crl}] = \int_{vol_e} dv [\nabla \times N]^T [v][\nabla \times N]
\tag{1.6.22}
$$

$$
[K_e^{div}] = \alpha[v] \int_{vol_e} dv [\nabla \cdot N]^T [\nabla \cdot N]
\tag{1.6.23}
$$

The element matrices represent element geometry combined with material properties. Note that the permeability matrix has been separated into a part due to the curl operator and a part due to the penalty function (associated with divergence). The key feature of the finite element method is the fact that these matrices represent integrals over nearly regular geometries, even in very complicated models. Thus, highly efficient numerical algorithms (Gaussian integration) can be used to evaluate them. This procedure is discussed in Chapter 5.

The expression for the volume excitation (load) vectors $\{M_0^e\}$, and $\{\rho_0^e\}$ are written as

$$
\{M_0^e\} = \int_{vol_e} dv [N]^T [v](\nabla \times \vec{M}_0)
\tag{1.6.24}
$$

$$
\{\rho_0^e\} = + \int_{vol_e} dv [N]^T \{s\}(\rho_0 - \nabla \cdot \vec{P}_0)
\tag{1.6.25}
$$

These excitations, as developed to this point, would be somewhat awkward to use since they only allow volume excitations through charge densities and remanent magnetization. In a rigorous sense these are the only excitations allowed on the system. Thus to model a wire it would be necessary to first construct a conducting path through the model and then apply appropriate voltage or current boundary conditions to cause current to flow. This approach is, however, unnecessarily restrictive.

The volume excitations associated with $\vec{M}_o$ can be generalized to include direct current excitations. The excitations computed in Eq. (1.6.24) show that the effects of $\vec{M}_o$ are resolved into effective current segments, which are then applied directly to the $\vec{A}$ DOFs at the nodes. The units of these excitations are (current x length) or (current density x volume). In EMAS, this concept is generalized so that current segment excitations can be applied in other ways. Fixed current densities $\vec{J}_o$ may be applied throughout the volume of any element, while current segments (total current x length) $\vec{j}_o$ may be applied directly at the nodes. The more useful form for $\{M_o^e\}$ is

$$\{M_o^e\} = \int_{vol_e} dv [N]^T [v](\nabla \times \vec{M}_o + \vec{J}_o) + \{\vec{j}_o\} \qquad (1.6.26)$$

where the grid point current segment vector $\{j_o^e\}$ is just a list of the current segments applied directly to components of $\vec{A}$ at the nodes

$$\{j_o^e\} = \left[j_{1x}, j_{1y}, j_{1z}, 0 \,\middle|\, ... \right]^T \qquad (1.6.27)$$

The imposed currents can be thought of as resulting from some unspecified but equivalent underlying distribution of $\vec{M}_o$.

Note that the atomic currents that make up the original excitations due to $\vec{M}_o$ are always divergence free. Any current distribution the user imposes must also be divergence free. If the imposed currents have divergence, then the implied accumulation of charge will not be correctly modeled. This may or may not be important to the user, depending on the circumstances.

Volume charge density excitations can be generalized to charge excitations on individual DOFs in a similar manner. Eq. (1.6.25) takes the effects of volume charge density and allocates them to individual ψ DOFs in units of total charge. EMAS allows the user to do this directly through grid point charge excitations. The more general form for the charge excitation vector is

$$\{\rho_o^e\} = + \int_{vol_e} dv \left([N]^T \{s\}(\rho_o - \nabla \cdot \vec{P}_o)\right) + \{q^e\} \qquad (1.6.28)$$

where the grid point charge vector $\{q^e\}$ is simply a list of the total charge assigned to each DOF

$$\{q^e\} = \left[0, 0, 0, q_{1,} \,\middle|\, ... \right]^T \qquad (1.6.29)$$

This charge vector may be thought of as resulting from some equivalent but unspecified charge density distribution.

The surface excitation vectors representing the effects of Neumann boundary conditions are given by

$$\{H^e\} = \int_{surf_e} dv[N]^T[v]((\vec{H}^* + \vec{M}_o) \times \hat{n}) \tag{1.6.30}$$

$$\{J^e\} = -\int_{surf_e} ds[N]^T\{s\}(\hat{n} \cdot (\vec{J}_{cond}^* + \dot{\vec{D}}^*)) \tag{1.6.31}$$

$$\{D^e\} = -\int_{surf_e} ds[N]^T\{s\}(\hat{n} \cdot (\vec{D}^* - \vec{P}_o^*)) \tag{1.6.32}$$

Here, the starred quantities (*) represent values imposed by the user. The surface integrals apply only to those element surfaces that are part of the problem boundary.

The next step is to sum work contributions from individual elements into a single expression for the work of the entire system. This is done through the matrix assembly process. As a result of matrix assembly, all of the element DOF vectors $\{u^e\}$ are assembled into one vector $\{u\}$. Likewise, the individual element matrices and excitation vectors are assembled into global quantities, which take into account contributions from all DOFs.

The result of this assembly process is an expression for the work associated with the entire system. This expression has the same form as for individual elements; but the matrices and vectors now represent assembled quantities

It is convenient to introduce matrix notation. Eqs. (1.6.1-4) can be written as a single matrix equation

$$\delta w = \int_{t_0} dt \left(\delta\{\dot{u}\}^T[M]\{\dot{u}\} - \delta\{u\}^T[B]\{\dot{u}\} \right.$$
$$- \delta\{u\}^T[K]\{u\} - \delta\{\dot{u}\}^T\{\rho_o\}$$
$$\left. + \delta\{u\}^T\{M_o\} + \delta\{u\}^T\{H\} + \delta\{u\}^T\{J\}) \right)$$
$$-\delta\{u\}^T\{D\}\Big|_{t_0} \tag{1.6.33}$$

The final step is to integrate by parts variations with respect to $\{\dot{u}\}$ in order to obtain generalized forces. These generalized forces are then equated to zero. This integrated expression can be written as follows:

$$[M]\{\ddot{u}\} + [B]\{\dot{u}\} + [K]\{u\} = \{P\} \tag{1.6.34}$$

where the assembled excitation vector $\{P\}$ is the sum of contributions from all volume and surface excitations

$$\{P\} = \{M_o\} + \{H\}_{surf} + \{J\}_{surf} \tag{1.6.35}$$

Integration by parts also generates an initial condition

$$[M]\{\ddot{u}_i\} = \{P_i\} \tag{1.6.36}$$

where the initial excitation vector is given by

$$\{P_i\} = \{\rho_o\} + \{D\}_{surf} \tag{1.6.37}$$

These matrix equations, which are equivalent to Maxwell's equations in their complete and general form, are solved by EMAS for the dynamic behavior of the $\vec{A}$ and ψ degrees of freedom.

To clarify these results, the equations of motion, Eqs. (1.6.34) and (1.6.36) are rewritten in $\vec{A} - \psi$ partitioned form

$$\begin{bmatrix} M^{AA} & M^{A\psi} \\ M^{\psi A} & M^{\psi\psi} \end{bmatrix}\begin{Bmatrix} \ddot{\vec{A}} \\ \ddot{\psi} \end{Bmatrix} + \begin{bmatrix} B^{AA} & B^{A\psi} \\ B^{\psi A} & B^{\psi\psi} \end{bmatrix}\begin{Bmatrix} \dot{\vec{A}} \\ \dot{\psi} \end{Bmatrix} + \begin{bmatrix} K^{AA} & 0 \\ 0 & 0 \end{bmatrix}\begin{Bmatrix} \vec{A} \\ \psi \end{Bmatrix} = \begin{Bmatrix} \vec{M}_o \\ 0 \end{Bmatrix}_{vol} + \begin{Bmatrix} \vec{H}_{tan} \\ \vec{J}_{nor} \end{Bmatrix}_{surf} + \begin{Bmatrix} \vec{j} \\ 0 \end{Bmatrix}_{grid} \tag{1.6.38}$$

$$\begin{bmatrix} 0 & 0 \\ M^{\psi A} & M^{\psi\psi} \end{bmatrix}\begin{Bmatrix} \dot{\vec{A}} \\ \dot{\psi} \end{Bmatrix} = \begin{Bmatrix} 0 \\ \rho_o \end{Bmatrix}_{vol} + \begin{Bmatrix} 0 \\ \vec{D}_{nor} \end{Bmatrix}_{surf} + \begin{Bmatrix} 0 \\ q \end{Bmatrix}_{grid} \tag{1.6.39}$$

The upper (AA) partition of Eq. (1.6.38) represents the curl-curl equation for the vector potential, Eq. (1.4.8). The lower partition ($\psi\psi$) represents the charge continuity condition, Eq. (1.4.9). Eq. (1.6.39) represents Gauss's law as an initial condition. The dielectric, conduction, and reluctivity matrices are symmetric, positive semidefinite, banded matrices. The right-hand side of Eq. (1.6.38) represents the excitations on the system. Volume excitations from remanent magnetization apply to $\vec{A}$ DOFs only. Direct grid point excitations on $\vec{A}$ DOFs are also allowed in the form of grid point current segments and constrained current densities. Surface excitations on $\vec{A}$ DOFs come from constrained values of $\vec{H}$. The only excitations on ψ come from surface excitations due to constrained values of $\vec{J}$. Note that the reluctivity matrix is null in the rows and columns associated with ψ DOFs.

1.6.3   Specialization for Specific Solution Types

Frequently the user is interested in a restricted class of behavior. Much time and effort can be saved by specializing the matrix equations. Specialization (Figure 1.6.2) is accomplished by partitioning the dynamic matrices, and by removing certain DOFs from the problem. There are many features that EMAS that make specialization both simple and efficient. Chief among these are user-specified constraints and user control of the solution process through DMAP programming. A few important examples are provided on the following pages to illustrate the process.
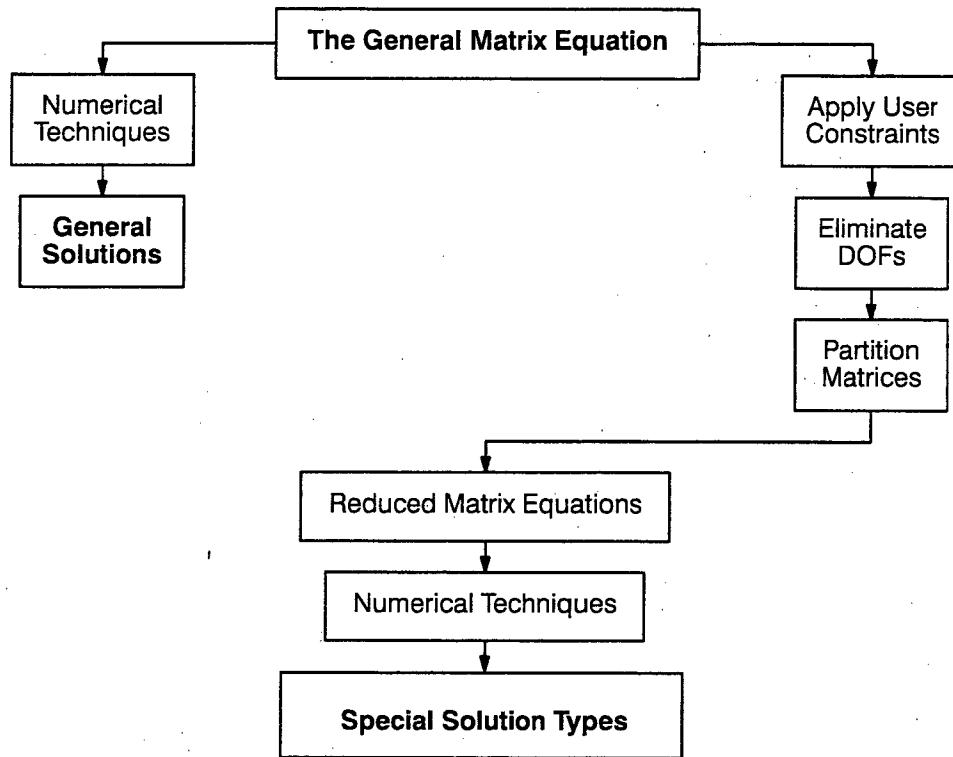
Figure 1.6.2: Specializing the matrix equation.

ELECTROSTATICS

Electrostatics problems are an example of specializing the general matrix equation of motion to save time and solution costs. In electrostatics it is assumed that

- There are no conducting media present, and thus, no ohmic currents.

- There are no magnetic fields.

- There are no dynamic electric fields.

- Static electric fields may be described by a scalar potential alone.

Under these assumptions, the equation of motion can be written as

$$
\begin{bmatrix} M^{AA} & M^{A\psi} \\ M^{\psi A} & M^{\psi\psi} \end{bmatrix} \begin{Bmatrix} \ddot{\vec{A}} \\ \ddot{\psi} \end{Bmatrix} + \begin{bmatrix} B^{AA} & B^{A\psi} \\ B^{\psi A} & B^{\psi\psi} \end{bmatrix} \begin{Bmatrix} \dot{\vec{A}} \\ \dot{\psi} \end{Bmatrix} + \begin{bmatrix} K^{AA} & 0 \\ 0 & 0 \end{bmatrix} \begin{Bmatrix} \vec{A} \\ \psi \end{Bmatrix} = \begin{Bmatrix} \vec{M}_o \\ 0 \end{Bmatrix}_{vol} + \begin{Bmatrix} \vec{H}_{tan} \\ \vec{J}_{nor} \end{Bmatrix}_{surf} + \begin{Bmatrix} \vec{I} \\ 0 \end{Bmatrix}_{grid}
\tag{1.6.40}
$$

$$
\begin{bmatrix} 0 & 0 \\ M^{\psi A} & M^{\psi\psi} \end{bmatrix} \begin{Bmatrix} \ddot{\vec{A}} \\ \ddot{\psi} \end{Bmatrix} = \begin{Bmatrix} 0 \\ \rho_o \end{Bmatrix}_{vol} + \begin{Bmatrix} 0 \\ \vec{D}_{nor} \end{Bmatrix}_{surf} + \begin{Bmatrix} 0 \\ q \end{Bmatrix}_{grid}
\tag{1.6.41}
$$

where the shaded terms are considered zero. The equation to be solved for electrostatics is simply

$$
[M^{\psi\psi}]\{\psi\} = \{\rho_o\}_{vol} + \{\vec{D}\}_{surf} + \{q\}_{grid}
\tag{1.6.42}
$$

The solution is specialized for electrostatics by a section in the static solution sequence that forms only the dielectric matrix, and uses the $\psi - \psi$ partition for static solution. The user need only set a parameter flag to effect this special treatment. The user must also constrain all $\vec{A}$ DOFs to zero (this is accomplished with a single data record).

STEADY CONDUCTION/MAGNETOSTATICS

Steady conduction/magnetostatic analysis calculates the time-independent flow of current through conducting bodies and the magnetic fields they produce. In this analysis, the following is assumed:

- There are no dynamic electric fields.

- All static electric fields may be described by a scalar potential.

- Direct current and magnetization excitations may be present.

- Surface excitations due to boundary conditions on both $\vec{H}$ and $\vec{J}$ may be present.

- Initial charges and initial surface boundary conditions are not present.

As a result, the equation of motion and initial condition may be written as

$$\begin{bmatrix} M^{AA} & M^{A\psi} \\ M^{\psi A} & M^{\psi\psi} \end{bmatrix}\begin{Bmatrix} \ddot{\vec{A}} \\ \ddot{\psi} \end{Bmatrix} + \begin{bmatrix} B^{AA} & B^{A\psi} \\ B^{\psi A} & B^{\psi\psi} \end{bmatrix}\begin{Bmatrix} \dot{\vec{A}} \\ \dot{\psi} \end{Bmatrix} + \begin{bmatrix} K^{AA} & 0 \\ 0 & 0 \end{bmatrix}\begin{Bmatrix} \vec{A} \\ \psi \end{Bmatrix} = \begin{Bmatrix} \vec{M}_o \\ 0 \end{Bmatrix}_{vol} + \begin{Bmatrix} \vec{H}_{tan} \\ \vec{J}_{nor} \end{Bmatrix}_{surf} + \begin{Bmatrix} \vec{J} \\ 0 \end{Bmatrix}_{grid} \tag{1.6.43}$$

$$\begin{bmatrix} 0 & 0 \\ M^{\psi A} & M^{\psi\psi} \end{bmatrix}\begin{Bmatrix} \dot{\vec{A}} \\ \dot{\psi} \end{Bmatrix} = \begin{Bmatrix} 0 \\ \rho_o \end{Bmatrix}_{vol} + \begin{Bmatrix} 0 \\ \vec{D}_{nor} \end{Bmatrix}_{surf} + \begin{Bmatrix} 0 \\ q \end{Bmatrix}_{grid} \tag{1.6.44}$$

where the shaded terms are considered zero. The equations to be solved may be rewritten as

$$[B^{\psi\psi}]\{\psi\} = \{J\}_{surf} \tag{1.6.45}$$

$$[K^{AA}]\{\vec{A}\} = \{M_o\}_{vol} + \{H\}_{surf} - [B^{A\psi}]\{\psi\} \tag{1.6.46}$$

The first equation is used to solve for the distribution of current within the conducting body. Excitations include constrained potentials or specified normal current at the boundary. This solution is then used as an excitation in the second equation, which computes the static magnetic fields due to the current flow, imposed currents, permanent magnets, and applied boundary conditions. Options to calculate the current distribution only, or the magnetic field only, are also available. Depending on which fields are to be calculated, the user should constrain the unused potentials.

CAVITY RESONANCE

Cavity resonance calculations analyze the normal modes of closed cavities. This is done through real eigenvalue analysis in which excitations and conducting media are not allowed. The dynamic equation can be written as

$$\begin{bmatrix} M^{AA} & M^{A\psi} \\ M^{\psi A} & M^{\psi\psi} \end{bmatrix}\begin{Bmatrix} \ddot{\vec{A}} \\ \ddot{\psi} \end{Bmatrix} + \begin{bmatrix} B^{AA} & B^{A\psi} \\ B^{\psi A} & B^{\psi\psi} \end{bmatrix}\begin{Bmatrix} \dot{\vec{A}} \\ \dot{\psi} \end{Bmatrix} + \begin{bmatrix} K^{AA} & 0 \\ 0 & 0 \end{bmatrix}\begin{Bmatrix} \vec{A} \\ \psi \end{Bmatrix} = \begin{Bmatrix} \vec{M}_o \\ 0 \end{Bmatrix}_{vol} + \begin{Bmatrix} \vec{H}_{tan} \\ J_{nor} \end{Bmatrix}_{surf} + \begin{Bmatrix} \vec{j} \\ 0 \end{Bmatrix}_{grid} \qquad (1.6.47)$$

where the shaded terms are considered zero. This equation reduces to a real eigenvalue problem,

$$(-\omega_i^2 [M^{AA}] + [K^{AA}])\{\vec{u}_i\} = 0 \qquad (1.6.48)$$

in which the solution eigenvectors $\{u_i\}$ are paired with corresponding eigenvalues, ω_i^2. EMAS has several efficient algorithms for extracting real eigenvalues of large matrices.

Waveguide analysis is a special case of cavity resonance in two dimensions. Analysis is usually conducted at cutoff, where there is no dependence in the propagation direction. Full dispersion relations can be constructed from cutoff results.

1.7   DATA RECOVERY

The electromagnetic potentials, by themselves, give little insight into the solutions. It is necessary to recover additional data from the potentials (Figure 1.7.1). Such data includes field values, energies, currents, and energy dissipation rates. A limited amount of basic data recovery is available, in tabular form, from EMAS. These data are associated either with grid points or with elements. Additional recovery data representing more elaborate combinations of the basic recovery data is available via postprocessing.
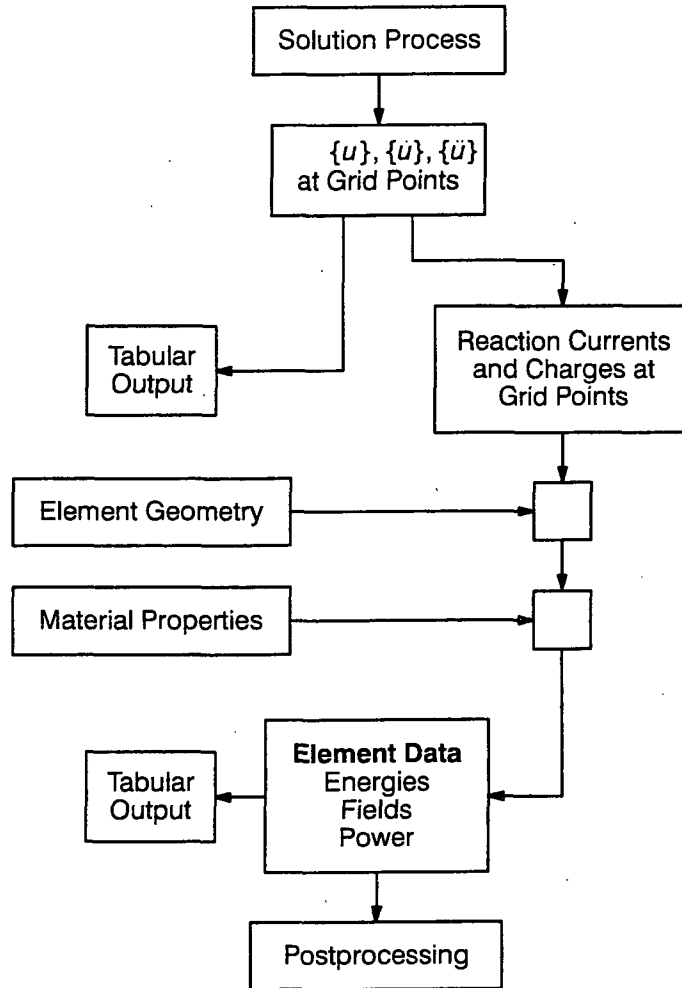
Figure 1.7.1: Data recovery.

The potentials are normally recovered as part of the solution process. The solution vector $\{u\}$ contains values of the DOFs that satisfy the matrix equation. The elements in EMAS are designed so that these values also represent, directly, the values of the potentials at the grid points. Time derivatives of the potentials are recovered in different ways depending on solution methods. In direct transient analysis, time derivatives are recovered from values of $\{u\}$ at different time steps. In frequency response and eigenvalue analysis, time derivatives are recovered through simple multiplication by $i\omega$.

Once the potentials are recovered at the grid points, the fields $\vec{E}$ and $\vec{B}$ can be recovered within each element. $\vec{B}$ is recovered using the expression

$$\vec{B} = [\nabla \times N]\{u\} \tag{1.7.1}$$

where the curl matrix, $[\nabla \times N]$, defined in Eq. (1.6.11), is evaluated at various locations (typically the numerical integration points). The value reported is just the computed average. The electric field is recovered in a similar manner, by evaluating the matrix expression

$$\vec{E} = [\nabla N]\{u\} \tag{1.7.2}$$

Here, the gradient matrix $[\nabla N]$ is defined in Eq. (1.6.15).

Electromagnetic energies are often of interest, particularly to judge energy balance, and accuracy of solutions. Various energy quantities are calculated from fields, and the applied excitations. The most general expression for the energy stored in electric fields is

$$W_E = \int_v dv \int_0^{\vec{D}} d\vec{D} \cdot \vec{E} \tag{1.7.3}$$

where the expression, $d\vec{D} \cdot \vec{E}$, is the work associated with a change in electric fields. An equivalent expression, $\vec{D} \cdot d\vec{E}$, in linear media was used in deriving the expression for virtual work. In the case of linear media, this expression reduces to a simpler form

$$W_E = \frac{1}{2} \int_v dv \, \vec{E} \cdot \vec{D} \tag{1.7.4}$$

Thus, $\vec{E} \cdot \vec{D}$, represents the energy density (energy per unit volume) associated with electric fields at any given point. An exactly equivalent expression, calculated using charges and the electrostatic potential, is given by

$$W_E = \frac{1}{2} \int_v dv \, \rho \psi \tag{1.7.5}$$

This form, called the input electric energy, does not include the energy input through constrained voltages, because the charges needed to maintain the constraints are outside the problem volume. Electric energies are available on an element-by-element basis, or as total quantities for the entire model.

The energy stored in magnetic fields is also of interest. The general expression is

$$W_B = \int_v dv \int_0^{\vec{B}} d\vec{B} \cdot \vec{H} \tag{1.7.6}$$

Note that the expression for work, $d\vec{B} \cdot \vec{H}$, is also used in the variational formulation of electromagnetics. An equivalent expression involving currents and the vector potential can be written as

$$W_B = \int_v dv \int_0^{\vec{A}} d\vec{A} \cdot \vec{J}_{cond} \tag{1.7.7}$$

This expression is, however, seldom calculated directly. The magnetic co-energy

$$W_{BC} = \int_v dv \int_o^{\vec{H}} d\vec{H} \cdot \vec{B} \qquad (1.7.8)$$

is also often of interest. The average of the magnetic energy and co-energy is exactly equal to the energy stored in an equivalent linear system with the same final $\vec{B}$ and $\vec{H}$ values. The energy in this linear system is given either by

$$W_B = \frac{1}{2} \int_v dv \, \vec{B} \cdot \vec{H} \qquad (1.7.9)$$

or by

$$W_B = \frac{1}{2} \int_v dv \, \vec{A} \cdot \vec{J}_{cond} \qquad (1.7.10)$$

The recovery of reaction currents due to constraints is relatively straightforward and efficient. Reaction currents are those currents that would be required to maintain the constraint on $\vec{A}$ at a given point. These currents are calculated using

$$\{J_{react}\} = [K]\{u\} \qquad (1.7.11)$$

evaluated for the constrained DOFs.

Conduction currents result from the combination of induced and imposed currents. The resulting Joule heating can be calculated during data recovery. The conduction current is given by Ohm's law

$$\vec{J}_{cond} = [\sigma]\vec{E} \qquad (1.7.12)$$

while the resulting energy dissipation is given by

$$P_\sigma = \vec{J}_{cond} \cdot \vec{E} \qquad (1.7.13)$$

The above expressions are all for materials with real, not complex, permittivity, permeability, and conductivity. Section 4.5 (the FIELDS command) describes changes to the above energy and power expressions for complex materials.

A final aspect of data recovery by EMAS is its printout of total energies and powers, both stored and input. These printouts are described in detail in Section 4.5 (the FIELDS command in Case Control). By comparing total *stored* energies and powers with total *input* energies and powers, the user can verify that the calculations of the program do indeed conform with the Law of Conservation of Energy.

1.8 NONLINEAR ANALYSIS

The linear material model used thus far is adequate for many applications. There are, however, many cases in which material response is nonlinear. For example, the nonlinear response of magnetic materials, including saturation and hysteresis effects, is critical to the performance of many practical devices. In this section the formulation of electromagnetics will be extended to include nonlinear magnetic effects. Analyses of nonlinear dielectric and conduction properties, though possible, are deferred. Nonlinear magnetic behavior results from complicated changes in the magnetization $\vec{M}$ with changing $\vec{B}$. Even in the most complicated situations, the magnetic field strength is given by the general definition

$$\vec{H} = v_o\vec{B} - \vec{M}. \tag{1.8.1}$$

In linear analysis it is assumed that $\vec{M}$ is proportional to $\vec{B}$, leading to the simple relationship

$$\vec{H} = [v]\vec{B}, \tag{1.8.2}$$

where $[v]$ is the constant reluctivity matrix. In nonlinear analysis, $\vec{M}$ and $\vec{H}$ have a more complicated dependence on $\vec{B}$. Accurate analyses can be performed for isotropic nonlinear materials including, e.g., soft iron and steel. In these materials $\vec{M}$ is always parallel to $\vec{B}$, but is not necessarily a linear function.

Materials are usually characterized by B-H curves. Figure 1.8.1 shows an example of simplified B-H data. The magnetic field strength $\vec{H}$ is usually considered to be the independent variable because it can be measured (or calculated) in the absence of magnetic materials. $\vec{B}$ is then measured as a function of the applied magnetic field strength. Results such as those shown are typical in soft materials, which do not exhibit hysteresis. The initial permeability may be quite high, as much as several thousand ($\times \mu_o$). Eventually the material saturates because all magnetic moments are aligned with the applied field. Any subsequent increase dH only increases B by an amount v_odH, as if the magnetic material were not present.
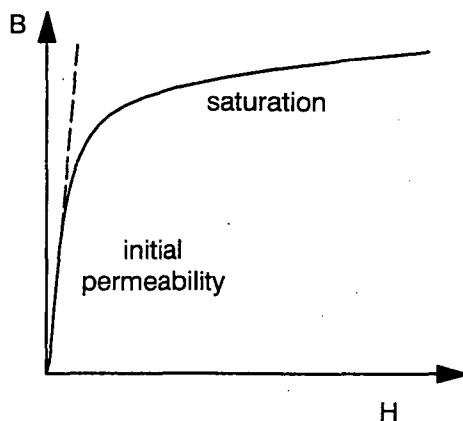
Figure 1.8.1: Simplified B-H curve.

A typical H(B) function generated from B(H) data is shown in Figure 1.8.2. This function is used in nonlinear analysis because the independent variable B is more closely related to the vector potential. Here the initial reluctivity is quite low, but increases sharply as the material saturates. The distinction between the secant reluctivity, $\frac{H}{B}$, and the tangent reluctivity, $\frac{dH}{dB}$, should be noted.
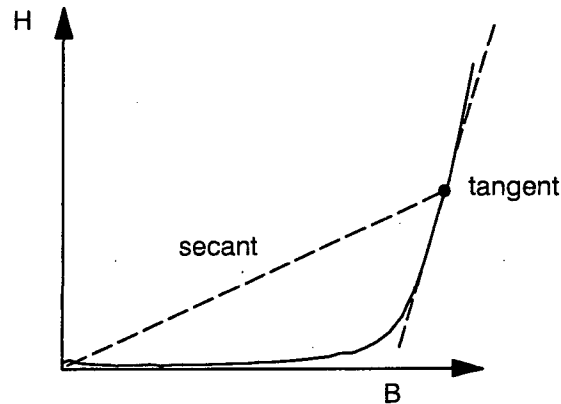
Figure 1.8.2: Simplified H-B function.

The approach to nonlinear analysis will be to first generalize the expression for magnetic virtual work to allow $\vec{H}$ to be an arbitrary nonlinear function of $\vec{B}$. This new expression gives rise to nonlinear loads in the matrix equations. Equilibrium between generalized forces is then imposed through an iteration technique.

1.8.1   Matrix Equations

The basic expression for magnetic virtual work, from Eq. (1.5.2), is as follows:

$$\delta W_B = - \int_{vol_e} dv \; \delta \vec{B} \cdot \vec{H} \tag{1.8.3}$$

This expression is valid even in cases where $\vec{H}$ is a nonlinear function of $\vec{B}$. In linear analysis an expression for the reluctivity matrix [K] is obtained by using $\vec{H} = [v]\vec{B}$. This same expression still applies to linear elements within a nonlinear model. In elements where $\vec{H}$ is a nonlinear function of $\vec{B}$, the magnetic virtual work is written as

$$\delta W_B = - \delta \left\{ \vec{A} \right\}^T \{F\} \tag{1.8.4}$$

where the nonlinear excitation (load) {F} is given by

$$\{F\} = \int_{vol_e} dv \; [\nabla \times N]^T \vec{H}\!\left(\vec{B}\right) \tag{1.8.5}$$

and the curl operator shape function matrix $[\nabla \times N]^T$ is defined in Eq. (1.6.11).

The matrix equations now express a force balance between static, dynamic, and nonlinear forces (equivalent to Kirchhoff's current law). In final form they may be written as

$$\{R\} = [M]\{\ddot{u}\} + [B]\{\dot{u}\} + \left[K^{lin}\right]\{u\} - \{P\} + \{F\} = 0 \tag{1.8.6}$$

where {R} is the residual force. Here, [M] and [B] represent the usual dielectric and conduction matrices; {u} represents the normal DOF column vector; and {P} represents loads from currents and charges. Contributions from the magnetic virtual work are split between two terms. The matrix $\left[K^{lin}\right]$ represents

magnetic energy for linear elements (and the divergence penalty energy for all elements), while magnetic energy for nonlinear elements is represented by $\{F\}$. In statics,

$$\{R\} = \left[K^{lin}\right]\{u\} - \{P\} + \{F\} = 0 \qquad (1.8.7)$$

since dynamic forces are zero.

1.8.2   The Newton-Raphson Solution Method (Statics)

Because the matrix equations now contain nonlinear terms, they can no longer be solved using standard linear techniques. In statics a nonlinear matrix technique similar to Newton's method is used. Many enhancements are included to increase stability and efficiency. Assume that we have a guess for the solution, call it $\{u_o\}$, and that we wish to calculate the correction vector $\{\Delta u\}$ which reduces the residual force $\{R\}$ to zero. First, expand the i-th component of the residual force R_i in a matrix Taylor series around $\{u_o\}$

$$R(u_0 + \Delta u)_i \approx R(u_0)_i + T_{ij}\big|_{u_o} \Delta u_j = 0 \qquad (1.8.8)$$

(Note the use of summation notation.) The tangent matrix T_{ij} is given by

$$T_{ij} = \frac{\partial\{R\}_i}{\partial u_j} \qquad (1.8.9)$$

This equation is then solved for the correction vector $\{\Delta u\}$

$$\{\Delta u\} = -[T]^{-1}\{R(u_0)\} \qquad (1.8.10)$$

The correction vector is added to $\{u_o\}$ to obtain a new guess $\{u_1\}$; and the iteration process is repeated until a satisfactory solution is obtained.

This Newton-Raphson iterative method can be interpreted graphically as shown in Figure 1.8.3. This figure shows the ith component of the residual force R_i as a function of the j-th component of the DOF vector u_j. The i-j element of the tangent matrix represents the slope of this curve. As the iteration process continues, the series of approximate solutions, u_{j1}, u_{j2}..., converges to the actual solution. Note that in this example the slope is recalculated at each iteration step.
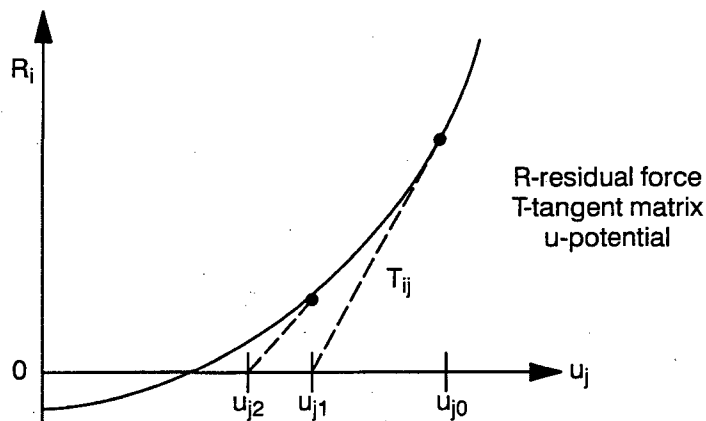
Figure 1.8.3: Newton-Raphson method.

1.8.3　Evaluation of the Tangent Matrix, T_{ij}

The tangent matrix T_{ij} is evaluated by direct differentiation of the residual force vector. By differentiating the i-th component of Eq. (1.8.7) with respect to u_j the following expression is obtained:

$$T_{ij}|_{u_o} = K_{ij}^{lin} + \frac{\partial F_i}{\partial u_j}\Big|_{u_o} \tag{1.8.11}$$

In the case of linear elements the tangent matrix is simply the constant linear reluctivity matrix. For nonlinear elements the tangent matrix is the derivative of the nonlinear load with respect to the various DOFs.

The derivatives of the nonlinear load are evaluated by differentiation of Eq. (1.8.5)

$$\frac{\partial F_i}{\partial u_j} = \int_{vol_e} dv\ [\nabla \times N]_{ki} \frac{\partial H_k}{\partial u_j} \tag{1.8.12}$$

The chain rule is then used to express the derivatives of $\vec{H}$

$$\frac{\partial H_k}{\partial u_j} = \frac{\partial H_k}{\partial B_l}\frac{\partial B_l}{\partial u_j} \tag{1.8.13}$$

Finally, the derivatives of $\vec{B}$ are evaluated using the definition, $\vec{B} = [\nabla \times N]^T\{u\}$

$$\frac{\partial B_l}{\partial u_j} = [\nabla \times N]_{lj} \tag{1.8.14}$$

By combining these results, the following final expression is obtained:

$$\frac{\partial F_i}{\partial u_j} = \int_{vol_e} dv\ [\nabla \times N]^T[v^{tan}][\nabla \times N] \tag{1.8.15}$$

Note that this final expression for the nonlinear tangent matrix is exactly the same at $[K^{lin}]$ except that the tangent reluctivity matrix (tensor rotation),

$$v_{kl}^{tan} = \frac{\partial H_k}{\partial B_l} \tag{1.8.16}$$

is used in place of the reluctivity matrix $[v]$.

In principle any complicated model of magnetic materials, including nonlinear reluctivity and hysteresis, could be implemented simply by calculating a new $[v^{tan}]$ matrix for each update of the tangent matrix. In practice there is no widely accepted general method for calculating $[v^{tan}]$. Until such methods are developed, the following assumption is made:

$$v_{kl}^{tan} = v(B_k)\delta_{kl} \tag{1.8.17}$$

That is, the tangent reluctivity is a nonlinear isotropic function of $B = |\vec{B}|$. The reluctivity may be different for each B-component, but they are all drawn from the same function $v(B)$. The scalar function $v(B)$ is calculated from B(H) data input by the user. More complicated material models can be incorporated as material modeling techniques are developed.

1.8.4   Nonlinear Transient Analysis

Nonlinear transient analysis is a simple extension of the static Newton-Raphson technique described above. The full expression for the nonlinear residual forces is used, Eq. (1.8.6), including dynamic forces. Finite difference expressions for the time derivatives are used along with the static force expressions to write the residual force in terms of DOFs at present and past time steps. The solution proceeds by minimizing {R} with respect to DOFs at the next time step.

1.9 THE ANALOGY BETWEEN ELECTROMAGNETICS AND STRUCTURAL MECHANICS

The reader familiar with the matrix equation for the finite element analysis of structures will notice that the equation for electromagnetics, Eq. (1.6.34), has exactly the same form. This equivalence establishes a complete and general analogy between these two dynamic systems. This analogy is summarized in Table 1.9.1. Such an analogy is useful for a variety of reasons. Many users have experience in modeling structures using the finite element method. By understanding the analogy, such users will be immediately familiar with the methods used in EMAS. The analogy can also be useful for those already familiar with E&M. The matrix equation presents a complete and general yet relatively simple approach to the solution of Maxwell's equations. Such a unified approach is lacking in most analytic work. Furthermore, the mathematical techniques used to solve this equation—static analysis, frequency response, eigenvalues, etc.—are familiar. Users will benefit from applying knowledge, experience, and intuition from structural mechanics to the solution of E&M problems.

To exploit this analogy, some terminology has been borrowed from structural analysis. In many cases, concepts with no accepted electromagnetic terminology have been introduced. In such cases, the terms from structural mechanics have been adopted. Thus, users will encounter terms such as: "loads," "constraints," "shear," etc.—borrowed from the structures field.

This analogy with structural mechanics is quite deliberate. The analogy was established to exploit MSC/NASTRAN, the world's largest and most widely used finite element structural analysis program, as a resource for the development of EMAS. The unconventional potential ψ was introduced in order to align time derivatives, and produce a final matrix equation with the desired form. As a result, the dynamic matrices are symmetric, sparse, and banded—features required for efficient numerical processing.

When viewed as a mechanical system, the $\vec{A}$ DOFs in $\{u\}$ are analogous to the three components of physical displacement commonly used in elasticity, called translations and denoted by T1, T2, and T3. The fourth DOF, ψ, should also be thought of as displacement, even though it occupies a position normally reserved for the first rotational DOF, denoted as R1. Fields are produced by rotation (curl) and velocity in the E&M structure.

Electric and magnetic fields are also analogous to structural quantities. In E&M, curl (rotation) produces $\vec{B}$, while in structures, spatial derivatives of displacement produce strain. ν (stiffness) times $\vec{B}$ (strain) produce $\vec{H}$, which is analogous to stress. $\vec{E}$ is computed from time derivatives of $\{u\}$, making it analogous to velocity. $[\epsilon]$ (mass) times $\vec{E}$ produces $\vec{D}$, which is analogous to momentum. $\vec{E}$ and $\vec{B}$ are analogous to "pure" geometric quantities (space and time derivatives of displacement), while the constituent fields, $\vec{D}$ and $\vec{H}$, are analogous to structural quantities that are also associated with materials.

Initial and boundary conditions are analogous to those used in structures. In structures, initial displacements and velocities must be defined in order to have a well-posed initial value problem with a unique solution. In E&M, displacements $\vec{A}$ are assigned to reflect the initial distribution of $\vec{B}$, while initial velocities $\vec{A}$ are associated with $\vec{E}$. Neumann boundary conditions simply represent pressure loads and tractions, possibly time dependent, applied at the surfaces.

The stiffness properties of the E&M structures are quite different from those of physical structures. In physical structures, stiffness is provided by the energy associated with volume expansion and shear. Thus the singular motions in structures are uniform rotation and translation. In E&M, stiffness is provided only by rotation (curl), i.e., the energy associated with magnetic fields. Volume expansion (divergence), translation, and shear are all singular motions, and must be constrained to obtain unique solutions. Further, the fourth displacement ψ **never** has stiffness. Because ψ and $\vec{A}$ do not actually represent physical deformation, there is never any distortion of the model geometry. Thus, unconstrained motion in ψ is acceptable.

Electromagnetics exhibits inertia and damping effects similar to those found in structures. The dielectric matrix, analogous to the mass matrix, represents kinetic energy, $\vec{E} \cdot \vec{D}$, proportional to velocity squared. Without inertia (e.g., in eddy current analysis), electromagnetic waves cannot propagate. Similarly, the conduction matrix is the sole source of loss in the system, much like damping in structures. One key difference, however, is that structural damping is never known accurately, while [B] explicitly represents the known conduction properties of E&M materials. Indeed, Ohm's law is analogous to viscous damping in structures.

The analogy between structural loads and E&M excitations is less direct. $\vec{J}_o$ is analogous to a force density, while $\vec{M}_o$ is analogous to a torque density. ρ_o can be thought of as an impulse density. Point loads due to current segments and point charges are directly analogous to mechanical forces and impulses applied at grid points. The surface loads due to $\vec{H}$, $\vec{J}$, or $\vec{D}$ boundary conditions are directly analogous to pressure loads, tractions, and impulse density. Loads intended to produce magnetic fields, such as currents and boundary $\vec{H}$ fields, are always automatically applied in such a way as to produce rotation of the E&M structure. These forces are resisted by rotation stiffness, resulting in a finite displacement. Loads intended to produce electric fields, such as charges and boundary $\vec{D}$ fields, through ψ produce velocity. Since ψ has to stiffness, velocity changes are resisted by inertia.

Like structures, constraints are used in E&M to enforce a particular displacement. Forces of constraint on $\vec{A}$ and ψ DOFs (displacement) are currents (forces), while constraint forces on $\dot{\psi}$ (velocity) are charges (initial impulse). Multipoint constraints have similar uses in E&M and structures.

Data recovery in E&M is somewhat different, mainly because the quantities of interest are different, and more numerous. The recovery of displacements, velocities, and accelerations is exactly the same as in structures. Stress and strain recovery produce $\vec{B}$ and $\vec{H}$, while velocity and momentum produce $\vec{E}$ and $\vec{D}$. Material quantities such as $\vec{P}$ and $\vec{M}$ are similar to supplemental momentum and stress derived from materials, but have no direct structural analogy. Electric field energy, $\vec{E} \cdot \vec{D}$, is exactly equivalent to kinetic energy (velocity times momentum), while magnetic energy, $\vec{B} \cdot \vec{H}$, is exactly analogous to elastic energy (stress times strain). Joule heating (energy per unit time), $\vec{J}_{cond} \cdot \vec{E}$, is analogous to mechanical heating through friction or damping (friction force $\times$ velocity).

TABLE 1.9.1
The Analogy Between Electromagnetics
and Structural Mechanics

Symbol	Electromagnetics	Structural Mechanics
$\{u\}$	Potential vector containing $\vec{A}$ and ψ DOFs	displacement vector containing translation and rotation DOFs
$\{su\}$	$\vec{B}$	strain
$[k]\{su\}$	$\vec{H}$	stress
$\{\dot{u}\}$	$\vec{E}$	velocity
$[m]\{\dot{u}\}$	$\vec{D}$	momentum
$[M]$	dielectric matrix	mass matrix
$[B]$	conduction matrix	damping matrix
$[K]$	permeability matrix	stiffness matrix
$\{P\}$	excitation vector due to: $\vec{J}$ $\vec{j}$ $\vec{M}_o$ $\vec{P}_o$ $\vec{q}$ boundary $\vec{H}$ boundary $\vec{J}$ boundary $\vec{D}$	load vector due to: force density force torque impulse density impulse tractions pressure surface impulse
$\{\dot{u}\}^T[M]\{\dot{u}\}$	electric energy $\vec{E} \cdot \vec{D}$	kinetic energy velocity x momentum
$\{su\}^T[K]\{su\}$	magnetic energy $\vec{B} \cdot \vec{H}$	strain energy stress x strain
$\{\dot{u}\}^T[B]\{\dot{u}\}$	joule heating $\vec{J}_{cond} \cdot \vec{E}$	frictional heating force x velocity

Where s represents the appropriate spatial operator.

BIBLIOGRAPHY

MATHEMATICS

1. G. Arfken, *Mathematical Methods for Physicists,* New York: Academic Press,1970 – Provides a good discussion of vector and variational calculus. There are a number of good texts in this area.

ELECTROMAGNETICS

2. D. Halliday, and R. Resnick, *Physics: Part II*, New York: John Wiley & Sons, Inc.,1962 – The classic basic E&M text.

3. J. D. Jackson, *Classical Electromagnetics*, New York: John Wiley & Sons, Inc.,1962 – A classic advanced text in CGS units.

4. D. K. Cheng, *Field and Wave Electromagnetics*, Reading CA: Addison-Wesley, 1983 – A good intermediate text.

MATERIALS

5. C. Kittel, *Introduction to Solid State Physics*, New York: John Wiley & Sons, 1971 – The basic text on physical properties of materials.

FINITE ELEMENTS

6. O. C. Zienkiewicz, *The Finite Element Method in Engineering Science*, London: McGraw-Hill, 1971 – The classic text on the finite element method.

7. *What Every Engineer Should Know About Finite Element Analysis*, ed. J. R. Brauer, 2nd Edition, New York: Marcel Dekker, Inc.,1993 – A broad, modern book on applications of finite element methods in engineering.

8. *Finite Elements in Electrical and Magnetic Fields Problems*, ed. M. V. K. Chari, and P. P. Silvester, New York: John Wiley & Sons, 1980 – A text devoted specifically to finite elements in electromagnetism.

9. *The EMAS Modeling Guide*, ed. B. E. MacNeal, Los Angeles: The MacNeal-Schwendler Corp., 1991 – An introduction to basic electromagnetic finite element concepts and modeling.

10. R. H. MacNeal, *Finite Elements: Their Design and Performance,* New York: Marcel Dekker, Inc., 1994 – An introduction to the design of finite elements.

11. Louis Komzsik, *Supercomputing in Engineering Analysis*, New York: Marcel Dekker, Inc., 1992 – Optimization of Finite Element Software Systems on Supercomputers.

ELASTICITY

12. A. E. H. Love, *A Treatise on the Mathematical Theory of Elasticity*, New York: Dover 1944, (originally 1927) – An advanced mathematical treatment of elasticity.

13. S. P. Timoshenko, and J. N. Goodier, *Theory of Elasticity*, New York: McGraw-Hill, 1970) – The basic modern text on elasticity.

MSC/NASTRAN

14. H. G. Schaeffer, *MSC/NASTRAN Primer: Static and Normal Modes Analysis*, Milford, NH: Schaeffer Analysis, Inc., 1984) — A textbook on the use of MSC/NASTRAN.

15. *The NASTRAN Theoretical Manual (Level 15.5)*, ed. R. H. MacNeal, Los Angeles: The MacNeal-Schwendler Corporation, 1972 — The theory of structural analysis used in MSC/NASTRAN.

EMAS

1. J. R. Brauer, "Simple Equations for the Magnetization and Reluctivity Curves of Steel," *IEEE Transactions on Magnetics*, January 1975.

2. J. R. Brauer, "Saturated Magnetic Energy Functional for Finite Element Analysis of Electrical Machines," IEEE Winter Power Engineering Society Meeting, January 1975.

3. J. R. Brauer, "Flux Patterns by the Finite Element Method," *Record of IEEE Applied Magnetics Workshop*, June 1975.

4. J. R. Brauer, "Finite Element Analysis of Electromagnetic Induction in Transformers," IEEE Winter Power Engineering Society Meeting, January 1977.

5. J. R. Brauer, "Improvements in Finite Element Analysis of Magnetic Devices," *Digest of IEEE INTERMAG Conference*, June 1977.

6. J. R. Brauer, "Finite Element Analysis of Solenoids, Transformers, Generators, and Motors," *Record of Cleveland Electronics Conference*, 1978.

7. J. R. Brauer, "Finite Element Analysis of Electric and Magnetic Fields," *Proceedings of Chautauqua Conference on Finite Element Modeling*, September 1980.

8. J. M. Dishman, D. R. Kressler, and R. Rodriguez, "Characterization, Modeling, and Design of Swinging Inductors for Power Conversation Applications," *Proceedings of the Powercon Conference*, April 1981.

9. R. Rodriguez and J. M. Dishman, "Proximity Effect Calculation for Rectangular Planar Conductors," *Digest of IEEE INTERMAG Conference*, May 1981.

10. J. R. Brauer, "Finite Element Analysis of Single—Phase and Poly—Phase Induction Motors," *Conference Record of IEEE Industry Application Society Annual Meeting*, October 1981.

11. J. R. Brauer, "Finite Element Calculations of Eddy Currents and Skin Effects," COMPUMAG Conference, Chicago IL, March 1982, *IEEE Transactions on Magnetics*, March 1982.

12. J. R. Brauer, "Finite Element Calculations of Synchronous, Universal, and Induction Motor Performance," *Motorcon Conference Proceedings*, March 1982.

13. J. R. Brauer, "Finite Element Analysis of DC Motors and Step Motors," *Proceedings of Incremental Motion Control Symposium*, May 1983.

14. J. R. Brauer, "Finite Element Calculation of Magnetic Fields," *Proceedings of Incremental Motion Control Symposium*, May 1983.

15. J. R. Brauer, "Finite Element Calculation of Saturable Magnetic Fields in Steel Laminations," Seminar of Properties and Applications of Electrical Steels, May 1982.

16. J. R. Brauer, "Electromagnetic Fields and Performance of Electrical Products Calculated Using Finite Elements," *Proceedings of Coil Winding and Electrical Manufacturing Expo*, October 1982.

17. J. R. Brauer, "Open Boundary Finite Elements for Axisymmetric Magnetic and Skin Effect Problems," *Journal of Applied Physics*, November 1982.

18. J. R. Brauer, L. A. Larkin, and V. D. Overbye, "Finite Element Modeling of Permanent Magnet Devices," Magnetism and Magnetic Materials Conference, November 1983, *Journal of Applied Physics*, March 1984.

19. J. R. Brauer, "Finite Element Analysis of Ferrite Magnets During and After Magnetization," *Proceedings of the 4th Annual International Conference on Ferrites*, October 1984.

20. J. R. Brauer, R. Y Bodine, and L. A. Larkin, "Nonlinear Anisotropic Three−Dimensional Magnetic Energy Functional," COMPUMAG Conference, June 1983.

21. John R. Brauer and Craig M. Perlov, "Finite Element Analysis of Magnetic Recording Heads and Media," EM−Comp Conference, December 1984.

22. J. R. Brauer, R. H. Erickson, S. B. Sliper, and F. I. Zeisler, "Automotive Electrical Components Analyzed by Magnetic Finite Elements," SAE International Congress and Exposition, February 1985.

23. J. R. Brauer, "Finite Element Software Aids Motor Design," Small Motors Manufacturers Association Annual Meeting, March 1985.

24. J. R. Brauer, J. K. Hastings, and M. A. Juds, "Accuracy and Economy of Finite Element Magnetic Analysis," *Proceedings of National Relay Conference*, April 1985.

25. F. L. Zeisler and J. R. Brauer, "Automotive Alternator Electromagnetic Calculation Using Three−Dimensional Finite Elements," COMPUMAG Conference, August 1985, *IEEE Trans on Magnetics*, September 1986.

26. N. J. Lambert, "Electromagnetic Field Analysis of Automotive Electrical Components," International Symposium on Automotive Technology & Automation Conference, September 1985.

27. J. R. Brauer, "EMC of Automotive Wiring Analyzed by Finite Elements," SAE Passenger Car Meeting, September 1985.

28. Edwin J. Fabiszak Jr., "The Application of Finite Element Computer Models to Predict EMC/EMI," SAE Passenger Car Meeting, September 1985.

29. James H. Coffell, "Analytical Prediction of EMC Properties of an Automotive Horn," SAE Passenger Car Meeting, September 1985.

30. J. R. Brauer and C. M. Perlov, "Computer−Aided Design of a Magnetron Sputtering Cathode," INTERMAG Conference, April 1986, *IEEE Trans on Magnetics*, September 1986.

31. J. R. Brauer, J. J. Ruehl, and Anthony B. Bruno, "Finite Element Analysis of Microwave Cavities," Applied Computational Electromagnetics Conference, March 1987.

32. J. R. Brauer, M. Jenich, and Ali Bazoun, "Finite Element Software for EMI Evaluation," SAE Future Transportation Technology Conference, August 1987.

33. J. R. Brauer, E. A. Aronson, K. G. McCaughey, and W. N. Sullivan, "Three–Dimensional Finite Element Calculation of Saturable Magnetic Fluxes and Torques of an Actuator," COMPUMAG Conference, August 1987, *IEEE Trans on Magnetics*, January 1988.

34. J. R. Brauer, G. A. Zimmerlee, T. A. Bush, R. J. Sandel, and R. D. Schultz, "3D Finite Element Analysis of Automotive Alternators Under Any Load," COMPUMAG Conference, August 1987, *IEEE Trans on Magnetics*, January 1988.

35. J. R. Brauer, Haig Kalfaian, and Harold Moreines, "Dynamic Electric Fields Computed by Finite Elements," IEEE Industry Applications Society Meeting, October 1987, *IEEE Trans on Industry Applications*, November 1989.

36. J. R. Brauer, R. H. Vander Heiden, and A. B. Bruno, "Finite Element Modeling of Electromagnetic Resonators and Absorbers," Magnetism and Magnetic Materials Conference, November 1987, *Journal of Applied Physics*, April 1988.

37. A. B. Bruno and J. R. Brauer, "Scattering from an Infinite, Finitely Conducting Cylinder by Finite Element Analysis," Magnetism and Magnetic Materials Conference, November 1987, *Journal of Applied Physics*, April 1988.

38. R. H. Vander Heiden, J. R. Brauer, J. J. Ruehl, and G. A. Zimmerlee, "Utilizing Permanent Magnets in NonLinear Three–Dimensional Finite Element Analysis," INTERMAG/Magnetism & Magnetic Materials Conference, July 1988, *IEEE Trans on Magnetics*, November 1988.

39. G. A. Zimmerlee, J. R. Brauer, and J. A. Dobogai, "Application of Ampere's Circuital Law to Two– and Three–Dimensional Finite Element Analysis," INTERMAG/Magnetism & Magnetic Materials Conference, July 1988, *IEEE Trans on Magnetics*, November 1988.

40. J. R. Brauer, G. A. Zimmerlee, and V. D. Overbye, "Calculation of Magnetic Forces and Resulting Displacements Using Finite Elements," ASME International Computers in Engineering Conference and Exposition, August 1988.

41. B. E. MacNeal, "The Vector Potential Formulation of Electrodynamics Used in MSC/MAGNUM," ASME Computer Applications Symposium, October 1988.

42. B. E. MacNeal, R. H. MacNeal, and R. N. Coppolino, "Spurious Modes of Electromagnetic Vector Potential Finite Elements," International Journal of Computer Applications in Technology, July 1989.

43. E. A. Aronson and J. R. Brauer, "Magnetic Torque or Force Calculation by Direct Differentiation of Finite Element Coenergy," INTERMAG Conference, March 1989, IEEE Trans on Magnetics, September 1989.

44. J. R. Brauer and E. J. Fabiszak Jr., "Three–Dimensional Electromagnetic Fields Computed by Vector Potential Finite Elements," International Journal of Computer Applications in Technology, July 1989.

45. B. E. MAcNeal, J. R. Brauer, and R. N. Coppolino, "A General Finite Element Formulation of Electrodynamics in the Form of Structural Mechanics," COMPUMAG Conference, September 1989.

46. A. G. Brooks and H. E. Hall Jr., "Calculation of MWD Electromagnetic Resistivity Tool Response by a Finite Element Method," 64th Annual Tech Conference SPE, October 1989.

47. B. E. MacNeal, J. R. Brauer, and L. A. Larkin, "Analysis of Electromagnetic Resonant Cavities and Waveguides Using EMAS," *Proceedings of Conference on Codes and the Linear Accelerator Community*, Los Alamos, NM, January 1990.

48. B. E. MacNeal, J. R. Brauer, and R. N. Coppolino, "A General Finite Element Vector Potential Formulation of Electromagnetics Using a Time-Integrated Electric Scalar Potential," INTERMAG Conference, Brighton, UK, April 1990, *IEEE Transactions on Magnetics*, September 1990.

49. B. E. MacNeal, J. R. Brauer, L. A. Larkin, and A. O. Cifuentes, "Elimination of Finite Element Spurious Modes Using a Modal Transformation Technique," INTERMAG Conference, Brighton, UK, April 1990, *IEEE Transactions on Magnetics*, September 1990.

50. J. R. Brauer, S. M. Schaefer, N. J. Lambert, and B. E. MacNeal, "Mixing 2-D with 3-D Finite Elements in Magnetic Models," INTERMAG Conference, Brighton, UK, April 1990, *IEEE Transactions on Magnetics*, September 1990.

51. J. R. Brauer, B. E. MacNeal, V. D. Overbye, and G. T. Hummert, "Inhomogeneous Neumann Boundary Excitations for Electromagnetic Finite Element Analysis," *Proceedings of ELECTROSOFT Conference*, Lowell, MA, August 1990, Boston: Computational Mechanics Publishing, Inc.

52. J. R. Brauer, B. E. MacNeal, L. A. Larkin, and V. D. Overbye, "New Method of Modeling Electronic Circuits Coupled with 3-D Electromagnetic Finite Element Models," Conference on Electromagnetic Field Computation, Toronto, Ontario, October 1990, *IEEE Transactions on Magnetics*, September 1991.

53. J. R. Brauer, L. A. Larkin, and B. E. MacNeal, "Higher Order 3-D Isoparametric Finite Elements for Improved Magnetic Field Calculation Accuracy," Conference on Electromagnetic Field Computation, Toronto, Ontario, October 1990, *IEEE Transactions on Magnetics*, September 1991.

54. B. E. MacNeal and R. H. MacNeal, "Minimum Constraints For Finite Element Vector Potential Problems With Neumann Boundary Conditions," IEEE Conference on Electromagnetic Field Computation, October 1990.

55. J. R. Brauer, L. A. Larkin, B. E. MacNeal, and J. J. Ruehl, "New Nonlinear Algorithms for Finite Element Analysis of 2-D and 3-D Magnetic Fields," Magnetism and Magnetic Materials Conference, San Diego, CA, October 1990, *Journal of Applied Physics*, April 15, 1991.

56. "A New Finite Element Approach for Microwave Component Modelization and for Parasitic Radiation of a Satellite Harness," Antenna Congress, France, November 1990.

57. Claude Lorenson, "The Why's and How's of Mathematical Modelling for Microwave Heating", *Microwave World*, Spring, 1990.

58. P. Bisognin, J. C. Pourtau, and P. Zemlianoy, "Modeling of Radiated Electromagnetic Compatibility Inside a Telecommunication Satellite Payload Using a Finite Element Software (EMAS)," Proceedings of the 17th MSC European Users' Conference, September, 1990.

59. B. E. MacNeal and J. R. Brauer, "Finite Elements Aid Analysis of Resonant Cavities," *Microwaves & RF*, December 1990.

60. Youbok Lee, John R. Brauer, and James E. Richie, "Analysis of Three−Dimensional Microstrip Lines Using EMAS," Proceedings of Electromagnetics Sessions of MSC World Users' Conference, March 1991.

61. Glenn H. Stalker and Mary Jo Johnson, "Coupled Thermal Analysis Using EMAS and MSC/NASTRAN," *Proceedings of Electromagnetics Sessions of MSC World Users' Conference,* March 1991.

62. James E. Richie, "Current Research in High Frequency Applications Using EMAS at Marquette University," *Proceedings of Electromagnetics Sessions of MSC World Users' Conference,* March 1991.

63. David W. Fugate, "Eddy Current Analysis of a Three-Dimensional IEE of Japan Verification Model," *Proceedings of Electromagnetics Sessions of MSC World Users' Conference,* March 1991.

64. Mark L. Markel, "Finite Element Analysis of a Radiated Susceptibility and Emissions Test Chamber," *Proceedings of Electromagnetics Sessions of MSC World Users' Conference,* March 1991.

65. Abd A. Arkadan and Roy H. Vander Heiden, "An Investigation into the Modeling of Switching Devices Using EMAS," *Proceedings of Electromagnetics Sessions of MSC World Users' Conference,* March 1991.

66. Jin-Fa Lee and Raj Mittra, "Mesh Truncation in the Finite Element Analysis for Static Electric and Magnetic Fields," *Proceedings of Electromagnetics Sessions of MSC World Users' Conference,* March 1991.

67. P. Bisognin, PH. Lepeltier, JC. Pourtau, and P. Zemlianoy, "A New Finite Element Approach to Modelize Microwave Components and the Electromagnetic Field Generated by Satellite Harness," *Proceedings of Electromagnetics Sessions of MSC World Users' Conference,* March 1991.

68. A. H. J. Fleming and M. Krivitsky, "Radio Frequency Fields Around a Spheroidal Biological Model," *Proceedings of Electromagnetics Sessions of MSC World Users' Conference,* March 1991.

69. John R. Brauer, Scott M. Schaefer, and Raj Mittra, "Simulation of Static Open Boundary Problems in EMAS," *Proceedings of Electromagnetics Sessions of MSC World Users' Conference,* March 1991.

70. J. R. Brauer, S. M. Schaefer, Jin-Fa Lee, and R. Mittra, "Asymptotic Boundary Condition for Three Dimensional Magnetostatic Finite Elements," INTERMAG-MMM Conference, 1991, *IEEE Transactions on Magnetics,* November 1991.

71. B. E. MacNeal, "Finite Element Analysis of Electromagnetic Fields in the Form of Structural Mechanics," *Finite Elements in Analysis and Design,* 1991.

72. John R. Brauer and Franz Hirtenfelder, "Anisotropic Materials in Electromagnetic Finite Element Analysis," International Conference on Computation in Electromagnetics, November 1991.

73. John R. Brauer and Franz Hirtenfelder, "Surface Integrals on 3-D and 2-D Finite Element Models for Skin Effect Excitations and Open Boundaries," COMPUMAG, Sorrento, Italy, July 1991, *IEEE Transactions on Magnetics,* March 1992.

74. J. R. Brauer, L. A. Larkin, B. E. MacNeal and J. J. Ruehl, "New Nonlinear Algorithms for Finite Element Analysis of 2D and 3D Magnetic Fields," Conference on Magnetism and Magnetic Materials, April 1991.

75. R. H. Vander Heiden, J. R. Brauer, and T. R. Schmitt, "Non-Destructive Evaluation of DC and Frequency Response Problems Using Electromagnetic Finite Elements," *Electrosoft,* June/September 1991.

76. R. H. Vander Heiden, A. A. Arkadan, J. R. Brauer, and G. T. Hummert, "Finite Element Modeling of a Transformer Feeding a Rectified Load: The Coupled Power Electronics and Magnetic Field Problem," INTERMAG-MMM Conference, 1991, *IEEE Transactions on Magnetics,* November 1991.

77. J. R. Brauer, R. Mittra, and J. F. Lee, "Absorbing Boundary Condition for Vector and Scalar Potentials Arising in Electromagnetic Finite Element Analyses in Frequency and Time Domains," *Proceedings of IEEE Antennas & Propagation Society Symposium,* 1991.

78. J. R. Brauer and E. Nakamoto, "Finite Element Analysis of Nonlinear Anisotropic B-H Curves," *International Journal of Applied Electromagnetics in Materials,* Volume 1, 1992

79. J. R. Brauer, J. F. Lee, and R. Mittra, "Absorbing Boundary Condition for Three Dimensional Finite Element Models With Magnetic Vector and Time-Integrated Scalar Potentials," IEEE Antenna & Propagation Society Symposium, July 1992.

80. J. R. Brauer, R. W. Nopper, and D. C. Gates, "Three-Dimensional Finite Element Analysis of Inductance and Capacitance Matrices," IEEE Meeting on Electrical Performance of Electronic Packaging, Tucson AZ, April 22–24, 1992.

81. Dean C. Rovang, "Pulsed Magnetic Field Coil Engineering at Sandia National Laboratories Using EMAS and MSC/NASTRAN," *Proceedings of the MSC World Users' Conference,* May 1992.

82. A. Di Sabatino, F. Muzi, and R. Paggi, "Comparisons Between Experimental Tests and Numerical Simulations of a Special Transformer Behavior," *Proceedings of the MSC World Users' Conference,* May 1992.

83. Douglass A. Hettrick, "A Two Dimensional Finite Element Model of the Impedance Catheter Technique for Ventricular Volume Measurement," *Proceedings of the MSC World Users' Conference,* May 1992.

84. David W. Fugate, Maria E. Skutch, Dennis Pavlik, and Raul R. Rico, "Electromagnetic and Thermal Analyses of a Small-scale Rotor Heating Experiment," *Proceedings of the MSC World Users' Conference,* May 1992.

85. Richard L. Copeland and Marcus B. Kopp, "Three-dimensional Nonlinear Analysis of Anisotropic Magnetic Steels Using EMAS," *Proceedings of the MSC World Users' Conference,* May 1992.

86. Richard L. Copeland and Marcus B. Kopp, "Modeling Non-Square Loop Shape Permanent Magnets Using EMAS," *Proceedings of the MSC World Users' Conference,* May 1992.

87. Mark L. Markel, "Vehicle Magnetic Field Distribution," *Proceedings of the MSC World Users' Conference,* May 1992.

88. Mark L. Markel, "High Frequency Susceptibility Analysis of an Electronic Control Module," *Proceedings of the MSC World Users' Conference,* May 1992.

89. Petra Poschmann, Louis Komzsik, and Pat Lamers, "The Iterative Solver In EMAS Version 2," *Proceedings of the MSC World Users' Conference,* May 1992.

90. John R. Brauer, "EMAS Open Boundary Elements Applied to High Frequency Analyses," *Proceedings of the MSC World Users' Conference*, May 1992.

91. Brian S. Brown, "EMI/EMC Analyses Using EMAS," *Proceedings of the MSC World Users' Conference*, May 1992.

92. C. P. Cho and B. K. Fussell, "Analysis of a Large Horsepower Disc Rotor Axial-Field Brushless PM Motor Using Finite Element and Lumped Parameter Circuit Analysis," *Proceedings of the MSC World Users' Conference*, May 1992.

93. J. R. Garcia, J. M. Burdio, A. Mediano, A. Martenez, A. Roy, and J. Navarro, "An EMAS Calculation Method for Magnetic Hysteretic Losses," *Proceedings of the MSC World Users' Conference*, May 1992.

94. John R. Brauer, Franz Hirtenfelder, and Sunday Rwakasenyi, "3-D Eddy Current Computations Using Magnetic Vector Potential and Time Integrated Electric Scalar Potential," IGTE Symposium, June 1992.

95. John R. Brauer, "Finite Element Analysis of Power Electronic Circuits Containing Nonlinear Magnetic Components," IEEE Applied Power Electronics Conference, March 1993.

96. John R. Brauer, Jin-Fa Lee, and Raj Mittra, "Quadrilateral Finite Elements for Open Boundaries of Three-Dimensional Magnetostatic Finite Element Models," IEEE Intermag Conference, April 1992.

97. John R. Brauer and Bruce E. MacNeal, "Finite Element Modeling of Multiturn Windings with Attached Electric Circuits," IEEE Conference on EM Field Computation, August 1992.

98. R. H. Vander Heiden, A. A. Arkadan, and J. R. Brauer, "Nonlinear Transient Finite Element Modeling of a Capacitor-Discharge Magnetizing Fixture," IEEE Conference on EM Field Computation, August 1992.

99. John R. Brauer and Bruce E. MacNeal, "Finite Element Software for Electrical and Electronics Industries," *International Journal of Computer Applications in Technology*, vol. 5, no. 2, February 1992.

100. John R. Brauer and Brian S. Brown, "Capacitance and Inductance Calculations of 3D Devices Using Mixed-Dimensional Finite Elements," *Proceedings of the MSC Japan Users' Conference*, November 1992.

101. John R. Brauer, Eiji Nakamoto, and Pierre Allaud, "Crosstalk Simulation Using 3D Electromagnetic Finite Elements and Spice," *International Journal of Applied Electromagnetics in Materials*, January 1993.

102. Philippe Kienner and Klaus Kitzinger, "ISL 500 kJ 15mm Railgun Numerical Simulation," *IEEE Transactions on Magnetics*, January 1993.

103. John R. Brauer, Brian S. Brown, and Mark M. Jenich, "ABC Finite Elements for Open Boundary Electromagnetic Problems of Frequencies from DC to GHZ," *Proceedings of the Applied Computational Electromagnetics Society Conference*, March 1993.

104. John R. Brauer, Jeffrey J. Ruehl, Bruce E. MacNeal, and Franz Hirtenfelder, "Finite Element Analysis of Hall Sensors," INTERMAG, April 1993.

105. John R. Brauer, Bruce E. MacNeal, and Franz Hirtenfelder, "New Constraint Techniques for 3D Finite Element Analysis of Multiturn Windings with Attached Circuits," INTERMAG, April 1993.

106. Mark L. Markel, John R. Brauer, and Brian S. Brown, "Using Finite Element Software to Predict Automotive EMC," EMC/ESD International, April 1993.

107. Marcus B. Kopp, Vichate Ungvichian, and Richard L. Copeland, "Using EMAS in Simulating a Parallel Microstrip Transmission Line," *Proceedings of the MSC World Users' Conference*, May 1993.

108. Yehuda Goren and Linda Wallen, "Eddy Current Simulations for the SSCL Low Energy Booster Cavity," *Proceedings of the MSC World Users' Conference*, May 1993.

109. Richard L. Copeland and Markus B. Kopp, "3D Nonlinear Magnetization Studies of Thin Amorphous Ribbons," *Proceedings of the MSC World Users' Conference*, May 1993.

110. John R. Brauer and Charles R. Figer Jr., "EMAS Nonlinear Transient Analysis of Multiturn Coils with Attached Circuits," *Proceedings of the MSC World Users' Conference*, May 1993.

111. T. J. Wagener, James R. Campbell Jr., and James E. Lenz, "Magnetic Sensor Development Using Finite Element Analysis," *Proceedings of the MSC World Users' Conference*, May 1993.

112. Vern D. Overbye, Glenn H. Stalker, Scott M. Schaefer, Roy H. Vander Heiden, and S. Rajendran, "Induction Furnaces: Integrated EMAS, MSC/XL, and MSC/NASTRAN Analysis," *Proceedings of the MSC World Users' Conference*, May 1993.

113. Mark L. Markel, "Using Finite Element Software to Predict EMC Performance from Electronically Small Sources," *Proceedings of the MSC World Users' Conference*, May 1993.

114. John R. Brauer and Brian S. Brown, "Mixed-Dimensional Finite Element Models of Electromagnetic Coupling and Shielding," *IEEE Transactions on Electromagnetic Compatibility*, May 1993.

115. David S. Dixon, Michael Obara, and Nicholas Schade, "Finite-Element Analysis (FEA) as an EMC Prediction Tool," *IEEE Transactions on Electromagnetic Compatibility*, May 1993.

116. Philippe Kienner, "Soft Coupling of a 3D Electromagnetic Code with a 3D Fast Transient Dynamics Code to Model Rail Guns," *Proceedings of the MSC European Users' Conference*, September 1993.

117. M. Gasparotto, F. Lucca, D. Lattanzi, M. Roccella, and A. Pizzuto, "Eddy Currents in the NET/ITER Tokamak Machine Using EMAS Code," *Proceedings of the MSC European Users' Conference*, September 1993.

118. P. Henninger, "Postprocessing of Vector Quantities, Lorentz Forces and Moments in AC Analysis for Electromagnetic Devices," *Proceedings of the MSC European Users' Conference*, September 1993.

119. A. M. Miri, A. O. Hauser, and S. Rwakasenyi, "3-D Calculation of Transient Potential Distribution in High-Voltage Transformer Windings," *Proceedings of the MSC European Users' Conference*, September 1993.

120. Franz Hirtenfelder and Mark Markel, "Predicting Vehicle EMC/EMI Performance with Finite Element Software," ISATA Conference on Mechatronics, September 1993.

121. John R. Brauer and Brian S. Brown, "Finite Element Analysis of a Magnetoresistive Head," *Proceedings of the MSC Japan Users' Conference*, November 1993.

122. J. R. Brauer, J. J. Ruehl, D. R. Dawson, and B. S. Brown, "EMAS Analysis of Coupled Motion Problems," *Proceedings of the MSC Japan Users' Conference,* November 1993.

123. Q. M. Chen, "3D Static Force Analysis of TEAM Problem #20 Using EMAS," MSC Japan Users' Conference, November 1993.

124. Brian S. Brown, "Simulating Short Duration Printed Circuit Board Transients Using the Finite Element Time Domain Technique," *Proceedings of the MSC Japan Users' Conference,* November 1993.

125. Brian S. Brown, "Use of EMAS in Major Electrical Engineering Applications," *Proceedings of the MSC Japan Users' Conference,* November 1993.

126. W. J. Hu, "EMI Shielding Effectiveness Analysis of Conductive Polymer Composite Using Finite Element Method," *Proceedings of the MSC Taiwan Users' Conference,* November 1993.

127. Avraham Frenkel, "Finite Element Time-Domain Analysis of a Wideband Horn Antenna," IEEE Antennas and Propagation Symposium, July 1993.

128. John R. Brauer and Avraham Frenkel, "Absorbing Boundary Conditions for Finite Element Modeling of Phased Array Antennas," IEEE Antennas and Propagation Symposium, June 1994.

129. John R. Brauer and Jeffrey J. Ruehl, "3D Coupled Electromagnetic and Structural Finite Element Analysis of Motional Eddy Current Problems," *IEEE Transactions on Magnetics,* September 1994.

130. J. Frenkel, J. R. Brauer, and M. A. Gockel, "Complex Periodic Boundary Conditions for AC Finite Element Models," Applied Computational Electromagnetics Society Conference, March 1994.

131. J. R. Brauer, "Antenna Analysis Using Finite Element CAE Software," *Applied Microwaves and Wireless,* Winter 1994.

132. F. Hirtenfelder and B. S. Brown, "Analysis of Pulse Propagation in a Multi–Layer Circuit Board Using the Finite Element Time Domain Technique," 4th International Symposium on Electromagnetic Compatibility, October 1994.

133. J. R. Brauer, J. J. Ruehl, and Eiji Nakamoto, "Electric Field Actuator Analysis Using Coupled Electromagnetic and Structural Finite Elements," Proceedings of the International Symposium on Advanced Computational Design Techniques in Applied Electromagnetic Systems (ISEM–Seoul '94), June 1994.

134. Eiji Nakamoto and B. S. Brown, "Computation of the External Q of Waveguide Load Cavity Using the Finite Element Time Domain Technique," Asian TEAM Workshop, June 1994.

135. John L. Butler, Mark B. Moffett, and Kenneth D. Rolt, "A Finite Element Method for Estimating the Effective Coupling Coefficient of Magnetostrictive Transducers," *Journal of the Acoustical Society of America,* May 1994.

136. Hamid Sadeghi and Dr. Earl F. Richards, "Three–Dimensional Nonlinear Transient Analysis of Space Harmonics in a Shaded Pole Motor," MSC Special Electromagnetic Products Users' Conference, September 1994.

137. Mary Jo Vander Heiden and Mark A. Juds, "Verification of a 3−D Electromagnetic Finite Element EMAS Model for a DC Actuator," MSC Special Electromagnetic Products Users' Conference, September 1994.

138. Dr. David M. Drury, "Modelling of a Microstrip Patch Antenna with EMAS," MSC Special Electromagnetic Products Users' Conference, September 1994.

139. Tim McGaffigan and Todd Eisenberg, "Finite Element Electromagnetic Analysis of an Eight Arm Spiral Antenna Using EMAS," MSC Special Electromagnetic Products Users' Conference, September 1994.

140. Richard L. Copeland and Markus B. Kopp, "Electromagnetic Fields for a Circular Loop Antenna using EMAS," MSC Special Electromagnetic Products Users' Conference, September 1994.

141. Benjamin Klein and John Booske, "The Use of EMAS for the Evaluation of the Spindle−Shaped Semiconductor Laser Device Geometry," MSC Special Electromagnetic Products Users' Conference, September 1994.

142. Mark L. Markel, "Predicting Cross−Talk for a Simple Harness," MSC Special Electromagnetic Products Users' Conference, September 1994.

143. John R. Brauer, "Coupled Electromagnetic and Structural Finite Element Analysis of Transducers with Time−Varying Reluctances, Permittances, And Conductances," 1994 IGTE Symposium on Numerical Field Computation in Electrical Engineering, September 1994.

144. John R. Brauer, Jeffery J. Ruehl and Franz Hirtenfelder, "Coupled Nonlinear Electromagnetic and Structural Finite Element Analysis of an Actuator Excited by an Electric Circuit," IEEE Transactions on Magnetics, May 1995.

145. W. J. Hu, "A Three Dimensional Finite Element Analysis of Cardiac Defibrilation Current Distributions," MSC Taiwan Users' Conference, November 1994.

146. Franz Hirtenfelder and Avraham Frenkel, "Phased Array Simulations Using Finite Element Technique," 1995 ICAP Antennas and Propagation Conference, April 1995.

147. J. Zhang, K. Kim, and T. L. King, "Acceleration of Solid Hydrogen Pellet Using Augmented Railgun for Magnetic Fusion Reactor Refueling," IEEE Transactions on Magnetics, January 1995.

148. John R. Brauer, Jeffery J. Reuhl, Bruce E. MacNeal, and Franz Hirtenfelder, "Finite Element Analysis of Hall Effect and Magnetoresistance," IEEE Transactions on Electronic Devices, February 1995.

149. Jin−Fa Lee, Gary Lizalek, and John Brauer, "Finite Element Analysis of Waveguides Using Edge−Based Magnetic Vector Potential and Nodal−Based Electric Scalar Potential," Applied Computational Electromagnetics Society Conference, March 1995.

150. Mark A. Juds and John Brauer, "AC Contactor Motion Computed with Coupled Electromagnetic and Structural Finite Elements," IEEE Transactions on Magnetics, September 1995.

151. J. F. DeFord and P. Saladin, "Analysis of Waveguide Components using H_0−Curl Hexahedral Edge Elements in EMAS," IEEE Microwave Theory & Techniques Symposium (MTT−S), May 1995.

152. M. Gasparotto, F. Lucca, G. Paotti, and M. Roccella, "Temperature Growth−up and Mechanical Loads on the ENEA Facility CICC Test," MSC Italian Users' Conference, September 1994.

153. A. Di Sabatino, M. Linari, F. Muzi, and R. Paggi, "Probabilistic Reliability Analysis of a Simulated Finite−Element Electromechanical System," MSC Italian Users' Conference, September 1994.